Theses and Dissertations

2014

Modeling of Chemical-Mechanical Couplings in Solid Oxide Cells and Reliability Analysis

Xinfang Jin
University of South Carolina - Columbia

Recommended Citation

Jin, X.(2014). *Modeling of Chemical-Mechanical Couplings in Solid Oxide Cells and Reliability Analysis.* (Master's thesis). Retrieved from http://scholarcommons.sc.edu/etd/2581

MODELING OF CHEMICAL-MECHANICAL COUPLINGS IN SOLID OXIDE CELLS
AND RELIABILITY ANALYSIS

by

Xinfang Jin

Bachelor of Mechanical Engineering
University of Science and Technology, Beijing, 2004

Master of Mechanical Engineering
University of Science and Technology, Beijing, 2007

_____

Submitted in Partial Fulfillment of the Requirements

For the Degree of Doctor of Philosophy in

Mechanical Engineering

College of Engineering and Computing

University of South Carolina

2014

Accepted by:

Xingjian Xue, Major Professor

Michael Sutton, Committee Member

Jamil Khan, Committee Member

Xiao-dong Zhou, Committee Member

Lacy Ford, Vice Provost and Dean of Graduate Studies

ii

ABSTRACT

Solid oxide fuel cell (SOFC) has been well demonstrated as a promising clean energy conversion technology. For practical applications, the SOFC systems should have both good electrochemical performance and high reliability. The SOFCs are usually operated under very aggressive conditions, e.g., high temperatures (600-1000°C) and extremely low oxygen partial pressures (anode electrode). These aggressive operating conditions could lead to a variety of material system degradations, imposing great challenges on meeting lifetime requirement of SOFC commercial applications. It is therefore essential to increase the understanding of fundamental SOFC degradation mechanisms.

The basic structure of SOFCs is a positive electrode-electrolyte-negative electrode (PEN) tri-layer assembly, in which the dense electrolyte is sandwiched by porous electrode on either side. Because the material is different from one layer to another in PEN structure, and different materials have different thermal expansion coefficients, thermal stress occurs in PEN structure at elevated temperatures. The thermal stress effects on SOFC structures have been investigated extensively, however, the chemical stress effects are rarely studied, particularly their effects on the delamination at the cathode/electrolyte interface. The study of such chemical stress is very difficult or even impossible for present experimental techniques, but could be potentially feasible for modeling techniques.

iv

The defect transport process in conducting ceramics and non-stoichiometric conditions are closely related to the multi-physicochemical processes in SOFC devices, so the multi-physicochemical model is developed in the second section in both SOFC and SOEC mode. The model is validated with experimental V-I curves and utilized to investigate the performance degradation resulted from oxygen electrode/electrolyte interface delamination in chapter 3. Results indicate that delaminations significantly influence local charge current density distributions since the charge transport path is cutoff. In both parallel flow and counter flow settings, electrolysis performance is more sensitive to the delamination occurred at the center of the cell than those occurred at the edges of the cell.

To better understand the mechanism governing the delamination phenomenon, the chemical stress generated due to the non-uniform oxygen vacancy distribution at the interface is analyzed at Micro scale. The micro model considers the complicated interactions between structural mechanics and ionic transport process through conductive defects. While both the chemical and thermal stresses are complicated at the interface, the chemical stresses show different distribution patterns from the thermal stresses. The results of combined thermal and chemical stresses show that these two kinds of stresses can be partially canceled out with each other, leading to the reduced overall stresses at the cathode/electrolyte interface. The distributions of oxygen partial pressure and thus the oxygen vacancy concentration on the cathode particle surface have significant effects on chemical stress distribution and consequently on the principal stresses at the cathode/electrolyte interface.

For practical SOFC, the defect transport process is closely related to the multi-physicochemical processes, to predict the chemical stress generated in the cell under operating condition, a mathematical model is developed to study oxygen ionic transport induced chemical stress in a cell level in chapter 5. Comprehensive simulations are performed to investigate chemical stress distribution in the PEN assembly under different operating conditions and design parameters as well as mechanical constraints. Principal stress analysis is employed to identify the weakest zones in the cell. The Weibull approach is utilized to analyze failure probability of each components and the elastic energy stored in the cathode layer is employed to evaluate potential delamination failure at cathode/electrolyte interface. For the first time we build a chemical-mechanical coupling model at a cell level and is an important module complementary to the state-of-the-art electrochemical-thermal-mechanical model of SOFCs.

Upon the preceding results, we can conclude that under operating conditions, SOFCs are subjected to hundreds of MPa internal stress, introduced by either thermal mismatch or chemically induced strain. Such high mechanical stress is the major degradation mechanism limiting the industrial development of SOFC. Meanwhile, it can also be a factor for the physical property variation of the conducting ceramics. In chapter 6, we built a continuum model including space charge layers to simulate the charge transportation and interface reaction processes in a polycrystalline mixed ionic and electronic conductor (MIEC). Then, the impedance spectra of a MIEC SDC plate subjected to tensile stress is interpreted by the mathematical model. It indicates that when the MIEC ceramic is suffering from tensile stress, the ionic conductivity of the material will be increased, and the space charge layer will be stretched. The overall resistance of

the ceramic maintains constant by the combined effects. The results give further evidence of ionic conductivity enhancement under tensile stress. In addition, as temperature increases, the width increment of the space charge layer is more significant; the ionic mobility growth becomes less apparent. In other words, to be benefited from the mechanical stress, it is better for the polycrystalline MIEC ceramic working under low temperatures.

TABLE OF CONTENTS

LIST OF TABLES

LIST OF FIGURES

LIST OF SYMBOLS

A_v / S_a	Volumetric reactive surface area, (m^{-1})
C_p	Specific heat capacity of gas mixture, $(J / (kg \cdot K))$
c_j	Concentration of species/defects j, (mol/m^3)
C_i	Interfacial capacitance, (F)
$\overline{c_{v,0}}$	Uniform oxygen vacancy concentration in electrolyte, (mol/m^3)
D	Grain Size, (m)
D_j	Diffusion coefficient of defects j, (m^2/s)
D_{ij}	ij component of the multicomponent Fick diffusivity (m^2/s)
$D_{Kn,i}$	Knudsen diffusion coefficient of species i, (m^2/s)
E	Young's Modulus, (GPa)
E_r	Reversible voltage, (V)
F	Faraday's constant, $96485, (C / mol)$
G	Gibbs free energy, (J/mol)
K	Bulk modulus of the material, (GPa)
K_i	Equilibrium constant, $atm^{0.5}$
k_j	Reaction rate constant for species j, (m/s)
J_j	Current density of species j, (A/m^2)
h_j	Molar enthalpy of the species, (J/mol)
I	Momentum (kg·m/s)
L	Length, (m)

m	A shape parameter in Weibull approach
M_i	Molar weight of species i, (kg/mol)
m_j	Mobility of speices j, $\left(m^2 \cdot mol/(J \cdot s)\right)$
N_j	Molar flux of species j, (mol/m^2)
i_{ct}	Local charge transfer current densities, (A/m^2)
i_0	Exchange current density, (A/m^2)
k	Thermal conductivity of gas mixture, $\left(W/(m \cdot K)\right)$
K	Equilibrium constant, $atm^{1/2}$
m_j	Mobility of species j, $\left(m^2 \cdot mol/(J \cdot s)\right)$
M_j	Molar mass of species j (kg/mol)
M_{ij}	Mean molecular mass, (kg/mol)
n_i	Number of electrons in the reaction
N_j	Flux of species j, $\left(mol/(m^2 \bullet s)\right)$
P	Pressure, (Pa)
P_S^j	Survival probability under j principal stress
Q	Mass source term, (kg/m^3)/Heat source term, (W/m^3)
r	Surface reaction rate, $\left(mol/(m^2 \cdot s)\right)$
R	Gas constant, $8.314, (J/(mol \bullet K))$
R_i	Reaction source term for species i (kg/m^3·s)
ΔS	Entropy change, $J/(K \cdot mol)$
T	Temperature, (K)
t	Time, (s)
u(Vector)	Displacement, (m)/Velocity, (m/s)

V_m	Molar volume of the material, (m^3/mol)
V_j	Volume of the cell layer, (m^3)
V_0	Reference volume of the cell layer, (m^3)
$V_{1/2}$	Volume fraction of each phase in the composite material
w_j	Mass fraction of species j
x	x coordinate, (m)
x_j	Molar fraction of species j
z_j	Effective charge of species j
Z_j^*	Impedance of species j, (Ω)
α	Charge transfer coefficient/Thermal expansion coefficient, $(\frac{\mu m}{m}\frac{1}{K})$
β	Chemical expansion coefficient, (m^3/mol)
θ	Site fraction of adsorbate
$\Delta\chi_s$	Difference between the electrostatic potential drop across the surface and its equilibrium value, (V)
ν	Poisson's ratio
ν_i	Stoichiometric coefficient
ε_{ij}	Strain tensor
ε_{kk}	$\varepsilon_{kk} = \varepsilon_1 + \varepsilon_2 + \varepsilon_3$
ε	Porosity of the medium
$\varepsilon_r,$	Dielectric constant or relative permittivity, 10 (SDC)
ε_0	Vacuum permittivity, $8:8542\times10^{-12}$, (F/m)
ξ	Volume fraction of electron conducting material in porous electrode
τ	Tortuosity of porous electrodes
κ	Permeability of the medium, (m^2)
κ_i	Ionic conductivity in electrolyte, $(S \cdot m^{-1})$

σ	Conductivity of electron or ion (S/m)
σ_{ij}	Stress tensor, $\left(N/m^2\right)$
σ_j	Principal stress, (MPa)
σ_{kk}	$\sigma_{kk} = \sigma_1 + \sigma_2 + \sigma_3$, $\left(N/m^2\right)$
σ_0	Characteristic strength, (MPa)
τ_j	Stress induced potential by species j, $\left(J/mol\right)$
τ	Tortuosity
ω_i	Mass fraction of species i
μ	Dynamic viscosity (Pa·s)
μ_j	Electrochemical potential of species j, $\left(J/mol\right)$
ϕ	Potential, (V)
$\Delta\phi_{eq}$	Equilibrium potential difference (V)
η	Overvoltage (V)
ρ	Density, $\left(kg/m^3\right)$
δ	Oxygen nonstoichiometry
λ_S	Arbitrary space charge layer width, (m)
ω	Frequency

Subscripts

a	Dopant/Anode
c	Cathode
ct	Charge transfer
D	Diffusive flux

dis	Displacement current
e	Electron
eq	Equilibrium
f	Fracture/Fluid
h	Hydrogen electrode/Electron hole
i	Ionic
j	Species j
o	Oxygen electrode
t/T	Total
s	Solid
v	Oxygen vacancy
eq	Equilibrium
ref	Reference
react	Reactant
react-chanl	Reactant at the channel-electrode interface
prod	Product
prod-chanl	Product at the channel-electrode interface
ohm	Ohmic heating effect
act	Activation overpotentials
ent	Entropy change
0	Stoichiometric condition/Exchange/Dense material
H_2	Hydrogen
H_2O	Water
O_2	Oxygen

Superscripts

me	Mechanical
T	Thermal
c	Chemical
0	Stoichiometric
eff	Effective
eq	Equilibrium

LIST OF ABBREVIATIONS

CFD...Computational Fluid Dynamics

ECM..Equivalent Circuit Model

EIS .... Electrochemical Impedance Spectroscopy

FEM .... Finite Element Method

GDC ....$Ce_{0.9}Gd_{0.1}O_{1.95-\delta}$

GNP...Glycine–Nitrate–Process

LSCF.. $La_{0.6}Sr_{0.4}Co_{0.2}Fe_{0.8}O_{3-\delta}$

LSM .... $La_{0.8}Sr_{0.2}MnO_3$

MIEC...Mixed Ionic Electronic conducting

NiO..Nickel Oxide

PEN... Positive Electrode-Electrolyte-Negative Electrode

SDC...Sm0.2Ce0.8O1.9-δ

SOFC...Solid Oxide Fuel Cell

SOEC .... Solid Oxide Electrolyzer Cell

TEC...Thermal Expansion Coefficients

TPB .... Three Phase Boundary

YSZ.. Yttria-Stabilized Zirconia

CHAPTER 1

INTRODUCTION

1.1 FUEL CELL AS WAY OUT FOR ENERGY CRISES

Because of the rapid growth of economy and population, more and more countries and societies are experiencing energy crisis due to the excessive consumption of fossil fuel, especially coal, oil and gas [1-3]. On the other hand, the carbon dioxide emissions from the utilization of fossil fuels contributes significantly to global climate change with potentially catastrophic consequences [4-6]. To address these challenges facing the world, there is an increasing interest to develop renewable and clean energy technologies, such as fuel cell technology.

Fuel cells can convert the chemical energy in fossil fuels into electrical power in an electrochemical manner directly [7, 8] and have attracted significant attentions from both the scientific research centers and the profitable industries for the last few decades. Depending on the materials and transport mechanisms, fuel cells can be classified into proton exchange membrane fuel cell (PEMFC) [9-11], solid oxide fuel cell (SOFC) [12-14], alkaline fuel cell (AFC) [15, 16], molten-carbonate fuel cell(MCFC) [17, 18], phosphoric-acid fuel cell (PAFC) [19, 20], and direct-methanol fuel cell (DMFC) [21, 22]. Among these fuel cells, SOFCs demonstrate very unique advantages such as fuel flexibility, high system efficiency, and high heat byproduct, which are suitable for both stationary and portable applications.

1.2 INTRODUCTION OF SOLID OXIDE FUEL CELLS

The basic structure of solid oxide fuel cells (SOFCs) is a positive electrode-electrolyte-negative electrode (PEN) tri-layer assembly, in which the dense electrolyte is sandwiched by porous electrodes on either side. It can work under either solid oxide fuel cell (SOFC) mode or solid oxide electrolysis cell (SOEC) mode.
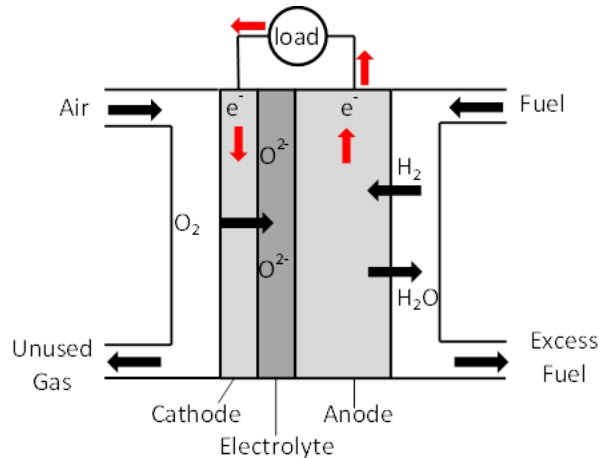
Figure 1.1 Illustration of SOFC

1.2.1 SOFC operating mode

SOFCs include very complicated transport processes and electrochemical reactions. As shown in Figure 1.1, taking an ionic conducting electrolyte based SOFC as an example, at the cathode side, the oxygen gas is fed into the cathode channel, and subsequently diffuses into porous cathode electrode, where the oxygen molecules combine with electrons from external circuit and form ions. The ions then transport through the dense electrolyte to the anode side. At the anode side, the fuel (e.g., hydrogen) flows into the anode channel and subsequently diffuses into the porous anode, where hydrogen molecules combine with oxygen ions and form water molecules and release electrons. The electrons then transport to the cathode side through external circuit,

providing useful electricity. The electrochemical reactions in the anode and cathode can be described respectively as follows,

$$H_2 + O^{2-} \rightarrow H_2O + 2e^-; \quad \frac{1}{2}O_2 + 2e^- \rightarrow O^{2-} \tag{1-1}$$

The overall reaction is then

$$H_2 + \frac{1}{2}O_2 \rightarrow H_2O \tag{1-2}$$
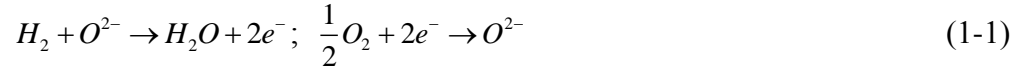
1.2.2 SOEC operating mode

The reverse operation of SOFC leads to SOEC mode. As shown in Figure 1.2, an electric potential sufficient for electrolysis is applied to the SOEC. Vapor/hydrogen gas mixture and air are supplied to the cathode and anode flow channels, respectively. At the cathode (hydrogen) side, vapor molecules transport through the porous cathode layer to the triple phase boundary (TPB) site, where the gas phase, electronic conducting material, and ionic conducting material meet together, and vapor is dissociated into hydrogen molecules and oxygen ions with a supply of electrons from external circuit. The hydrogen molecules then diffuse out of porous cathode electrode into the channel. The oxygen ions subsequently migrate to the anode (oxygen) side through the dense electrolyte. At TPB sites of the anode electrode, oxygen ions release electrons and form into oxygen molecules. The oxygen molecules then diffuse out of porous anode into the channel while the released electrons transport to the cathode side through external circuit. The electrochemical reactions at the cathode and anode can be described respectively as follows,

$$H_2O + 2e^- \rightarrow H_2 + O^{2-}; \quad O^{2-} \rightarrow \frac{1}{2}O_2 + 2e^- \tag{1-3}$$

The overall reaction is then

3

$$H_2O \rightarrow H_2 + \frac{1}{2}O_2 \qquad\qquad (1\text{-}4)$$
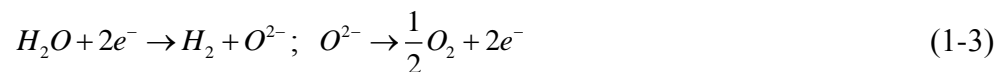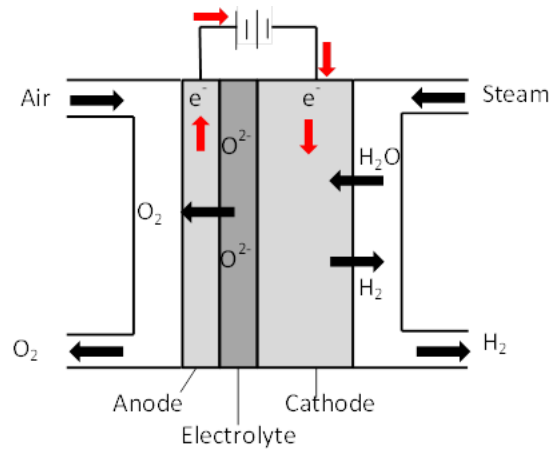
Figure 1.2 Illustration of SOEC

1.3 INVESTIGATION OF DEGRADATION IN SOFCS

The SOFC has been well demonstrated as a promising clean energy conversion technology. For practical applications, the SOFC systems should have both good electrochemical performance and high reliability. The SOFCs are usually operated under very aggressive conditions, e.g., high temperatures (600-1000°C) and extremely low oxygen partial pressures (anode electrode). These aggressive operating conditions could lead to a variety of material system degradations, imposing great challenges on meeting lifetime requirement of SOFC commercial applications.

As shown in Figure 1.3, the patterns of mechanical degradations can be classified into three types: vertical cracking in the cathode, vertical cracking in the electrolyte, and delamination near the cathode/electrolyte boundary. The performance degradations of SOFCs are frequently reported in open literature. However, the fundamental degradation mechanisms are not well understood. There have been various efforts toward the investigations of SOFC degradation mechanisms, such as material stability, redox

4

stability, coarsening of the microstructure due to sintering, thermal mismatch and chemically induced expansion.
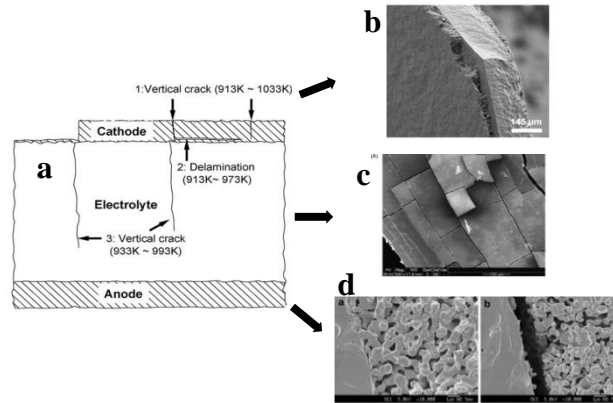
Figure 1.3 (a) Schematic representation of fracture pattern in SOFC button cell [23];(b) SEM image of a partially delaminated cathode layer on YSZ electrolyte [24];(c) SEM image of the cracks in the electrolyte [25];(d) SEM image of the cathode/electrolyte interface before and after experiment [26].

1.3.1 Material stability [27]

In addition to mechanical degradation, SOFCs also suffer from the issue of material stability. For example, phase separation take place in the electrolyte of 3-8.5 mol% Yttrium doped zirconia under operating conditions of the corresponding SOFC [28]. The tetragonal phase with 2.5-3 mol% Y_2O_3 content has lower conductivity by a factor of 3 than that with 8-8.5% Y_2O_3 [29]. Accordingly, the conductivity of the electrolyte is decreased and the fuel cell performance degrades.

SOFCs are fuel flexible, which can be operated on both hydrogen and hydrocarbon fuels. When hydrocarbon is used as the fuel, carbon deposition on the catalysis surface could take place. As a result, catalytic property of anode electrode would be deactivated [30, 31]. In addition, the hydrogen sulfide (H_2S) from hydrocarbon

fuel can also decrease the catalytic activity of anode due to the formation of Nickel sulfides [32, 33].

Under high temperature and multi-physics operating conditions, chemical reactions could take place between different materials in PEN assembly. Manganese-based perovskites with lanthanum and strontium on the A site (LSM) and yttria stabilized zirconia (YSZ) are widely used cathode and electrolyte materials respectively. The chemical reactions at LSM/YSZ interface generate the insulating phases of $SrZrO_3$ or $La2ZrO_7$ [34, 35]. The occurring of insulting phases would significantly deteriorate the conductivity of materials and PEN assembly [36, 37].

1.3.2 Redox stability

Nickel cermet is a state-of-the-art anode material. At elevated temperatures, the nickel oxide is reduced to nickel in reducing atmosphere (e.g., hydrogen). Once the fuel supply is stopped, the gas with oxygen flows into the anode electrode, the nickel will be oxidized to form nickel oxide [38]. The alternating reduction and oxidation of nickel cermet anode will lead to significant dimensional change of porous anode [39-45] and stress in SOFCs [38, 40, 42, 43, 46, 47].

1.3.3 Coarsening of the microstructure due to sintering[48]

The material with high curvatures tends to diffuse to the area with low curvature to lower the overall free energy of the system at elevated temperatures. For nickel cermet anode, nickel particles experience coarsening driven by the capillary process. The particle size will be enlarged, which is known as Ostwald ripening [49]. Furthermore, the three phase boundary sites will decrease, which will lead to the performance degradation.

1.3.4 Thermal Mismatch

Thermal stresses have been widely recognized as one of the main factors leading to the structural failure of SOFCs [50, 51]. Thermal stresses could be induced in the materials through several ways. During the cooling of the cell after being sintered at very high temperatures, stresses arise in the materials due to the mismatch in thermal expansion coefficients (TEC) between different layers of the cell [51]. Such stresses generated during cell fabrication processes are generally regarded as residual stresses. Residual stresses can also be expected if the cooling rates are not slow enough to sustain a quasi-steady heat transfer resulting in spatial temperature gradients [52]. The most widely investigated situations are thermal stresses induced by spatial temperature gradients during the fuel cell operations [50-54], particularly in transient operating conditions [55].

1.3.5 Chemical induced strain

The mechanical and electrical properties of oxide ion conductors depend on defect concentrations. Increasing oxygen vacancy concentration leads to higher oxygen ion conductivity and changes in oxygen vacancy concentration can lead to dimensional changes in the bulk material [56, 57].

1.3.5.1 Gadolinium doped ceria

For example, the Gadolinium doped ceria has a CaF_2 (Cubic) crystal structure, and the lattice constant is 5.423 , Figure 1.4. Each unit cell contains four cations (Ce^{4+} or Gd^{3+} in GDC) that form a face-centered cubic (fcc) cation sublattice. The eight tetrahedral interstitial sites of each fcc unit cell are occupied by oxygen ions or vacancies, which form a simple cubic (SC) anion sublattice.
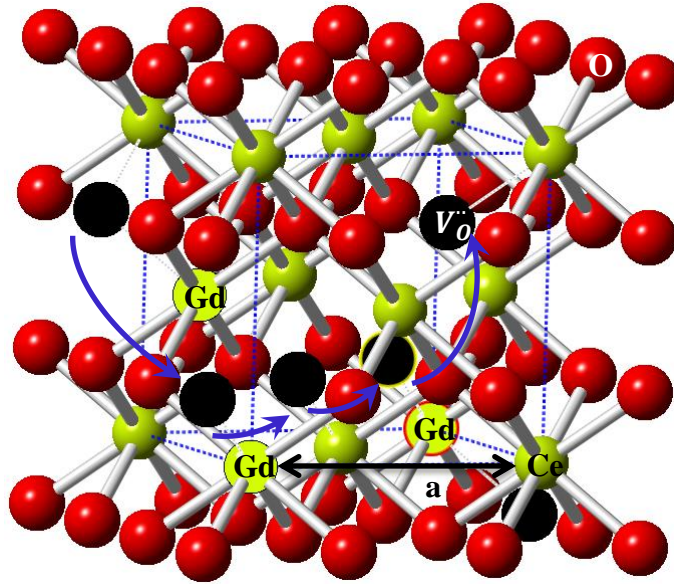
Figure 1.4 The crystal structure of GDC electrolyte

The oxides become oxygen deficient through oxygen vacancy formation at high temperatures in low PO_2 while maintaining the fluorite structure [57-61]. The oxygen deficiency readily occurs because Ce^{4+} cations are easily reduced to Ce^{3+} cations. Then, oxygen vacancies are generated to compensate the extra charge. The defect formation results in a chemical expansion because of electrostatic repulsion between defects and their surrounding atoms as well as the larger crystal radius of reduced cerium (Ce^{3+}) compared to the unreduced cerium (Ce^{4+}).

1.3.5.2 LSCF

LSCF is an ABO_3 type of the perovskite, the crystal structure of LSCF is shown in Figure 1.5. The lattice constant of LSCF is 3.925 . La/Sr occupies the A site, which is much larger than Co/Fe atom in B site. The ideal cubic-symmetry structure has the B cation in 6-fold coordination, surrounded by an octahedron of anions, and the A cation in 12-fold cuboctahedral coordination. Another example of ABO_3 type of the perovskite is $La_{1-x}Sr_xCoO_{3-\delta}$ as investigated by Adler and Atkinson [62, 63]. The mixed electronic ionic

8

conducting oxide contains transition metal cation to provide high electronic conductivity and is likely to become oxygen deficient under reducing conditions. The extra vacancy will lead to an increase in the lattice parameter of the oxide crystal.
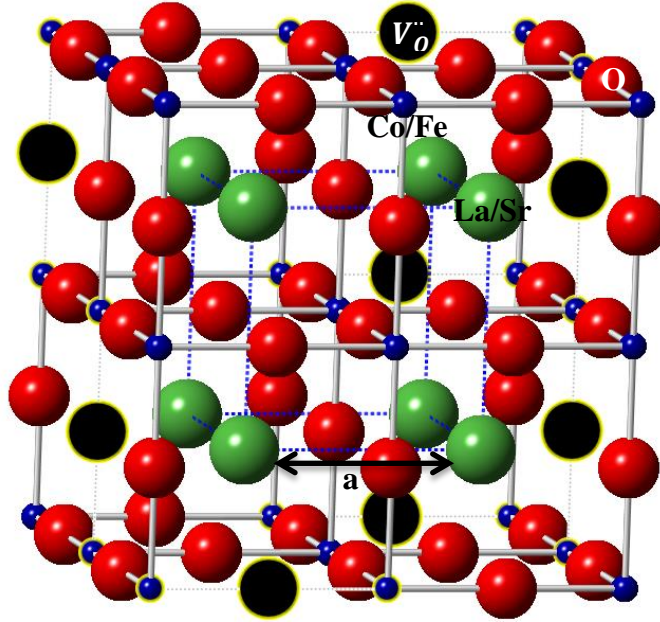
Figure 1.5 The crystal structure of LSCF cathode

1.4 STUDY OF THERMAL STRESS

The basic structure of SOFCs is the positive-electrode/electrolyte/negative-electrode (PEN) tri-layer assembly. Because the materials are different from one layer to another, the thermal stress occurs at elevated temperatures due to thermal expansion mismatch. In open literature, the thermal stress issues in SOFCs have been studied extensively using modeling approach. Kim et al. studied thermal stress of functionally graded SOFCs with assumed temperature distributions [64]. Liu et al. investigated the thermal stress at electrode/electrolyte interface, upon which lifetime of SOFCs was predicted under assumed thermal cycling conditions [54]. Since the thermal stress is dependent on the temperature distribution across SOFC structure, the multi-physics electrochemical model is usually needed to determine the temperature distribution, upon

which thermal stress is calculated. Clague et al. analyzed thermal stress of anode-supported SOFC under duty cycles using the temperature distribution predicted by computational fluid dynamics model [65]. Peksen et al. performed the transient thermal-mechanical analysis for an SOFC short stack using the similar approach [66]. Khaleel et al. carried out stack thermal stress analysis using the temperature profile calculated from the coupled electrochemistry, thermal and flow analysis [67]. All of these represent significant progress toward thermal stress analysis of SOFC structures.

1.5 STUDY OF CHEMICAL INDUCED STRAIN

SOFCs require materials with the ability to release or store oxygen in addition to a high concentration of oxygen vacancies for high oxygen ionic conductivity [68]. The transport of oxygen ion through oxygen vacancies may lead to the effect that the distribution of oxygen vacancy concentration is not uniform within the bulk materials, which would cause different volumetric expansions within the materials. As a result, chemical stress occurs in oxygen ionic conducting materials. In open literature, the thermal stress effects on SOFC structures have been investigated extensively, however, the chemical stress effects are rarely studied, particularly their effects on the delamination at the cathode/electrolyte interface.

Early studies try to understand and build the correlations between (oxygen vacancy) defect equilibrium and chemical expansion through bulk Gadolinium doped ceria (GDC) material characterizations, Wachsman[69-71] Wang[59, 72] and Adler [62]. Later on, there are several literatures to study the chemical stress in the GDC electrolyte only through 1-D modeling, Yakabe et al.[73], Atkinson[63, 74], Krishnamurohy et al.[75], Swaminathan et al.[76-78] , Terada et al. [79]., representing a significant progress towards the understanding

of chemical-mechanical coupling in a component of SOFCs at continuum scale. However, practical SOFCs involve very complicated physicochemical process particularly in porous electrodes. These processes and operating conditions could generate complicated chemical stresses in SOFC structure. For example, hydrogen (pure or derived from hydrocarbon) is used as the fuel to the GDC/Ni composite anode. Accordingly the anode porous structure is exposed to the hydrogen with low oxygen partial pressure. At elevated temperatures, the GDC material releases or stores oxygen in order to maintain the oxygen equilibrium. As a result, oxygen vacancies vary in the solid, generating chemical stresses in the SOFC structure. Depending on the specific designs of SOFCs and operating conditions, the chemical stresses could be further complicated.

1.6 OBJECTIVES OF THIS DISSERTATION

The study of such chemical stress is very difficult or even impossible for present experimental techniques, but could be potentially feasible for modeling techniques. Nevertheless, modeling of processes described above needs mechanical-chemical couplings under comprehensive multi-physicochemical processes enabling SOFC operations. The objective of this research is to develop an innovative model of SOFCs to study the chemical-mechanical coupling phenomena subjected to the effects of complicated multi-physicochemical processes. Based upon the model development, the structural reliability due to chemical stress will be evaluated and correlated to different operating conditions of SOFCs. The model will link the multi-transport processes and electrochemical reactions to the solid mechanics of functional materials. In addition, the effect of mechanical stress on electrical properties of MIEC will be investigated by impedance spectra.

1.7 DISSERTATION ORGANIZATION

The study of this dissertation is divided into seven chapters. In chapter 2, a 2D CFD model is built to simulate the multi-physics processes in the planar solid oxide fuel cell. The model is employed to investigate complicated responses of the cell during the transient process of mode switching. Then, the model is modified and applied in SOEC mode for delamination study in chapter 3. To better understand the mechanical failure of delamination at cathode/electrolyte interface, a micro model is developed to study the cathode/electrolyte interfacial stresses in chapter 4. In chapter 5, an innovative model at a cell level is developed to study chemical-mechanical coupling phenomenon. The model considers the chemical stress in PEN structure induced by complicated multi-physicochemical processes. In chapter 6, a continuum model is developed, linking the charge transport processes in a polycrystalline mixed ionic and electronic conductor (MIEC) to the electrochemical impedance spectroscopy response. The model is employed to interpret the experimental data of an MIEC SDC slab subjected to tensile stress. In the last chapter, the contributions of this dissertation are summarized and future work is provided.

CHAPTER 2

MATHEMATICAL MODELING ANALYSIS OF REGENERATIVE SOLID OXIDE FUEL CELLS IN SWITCHING MODE CONDITIONS

2.1 INTRODUCTION

Solid oxide fuel cell (SOFC) is one of promising clean energy technologies that convert the chemical energy of hydrogen into electronic energy directly [80]. Mathematical modeling technique has been proved a cost effective method in fundamental mechanism understanding and optimization designs of SOFCs at different levels. In this respect, steady state models have been developed extensively to study various internal parameter distributions including heat transfer, mass transport, charge migration, and electrochemical reactions and their links to SOFC performances [81-85]. Transient models have also been utilized to investigate SOFC dynamic behaviors [86-93].

The SOFC can also be operated in electrolysis mode, e.g., solid oxide electrolyzer cell (SOEC), where hydrogen/oxygen is generated with the consumption of electricity. In this respect, SOEC models have been developed in literature, most of which are steady state [94-100]; few models can be found for transient performance investigations.

When a solid oxide cell/stack is operated in SOFC mode and SOEC mode alternatively, energy sustainability could be implemented. In this regenerative operating mode, SOFC/SOEC system is able to better utilize and support electricity grid. When grid electricity demand increases, SOFC mode turns on to generate electricity for the

grid; when grid electricity demand decreases, SOEC may utilize grid electricity to produce hydrogen. During the switching process between SOFC mode and SOEC mode, there will be very complicated transient interactions between electrochemical reactions and transport processes. The fundamental mechanism understanding under the switching mode will play a significant role for SOFC/SOEC system design and operations. However, no research can be found in open literatures for this purpose.

This research aims at investigating transient behaviors of SOFC/SOEC in switching mode conditions using mathematical modeling approach. The research considers a general 2-D model that includes flow channels and positive electrode-electrolyte-negative electrode (PEN) assembly. The research goal is to elucidate the complicated interactions among transport and electrochemical processes when the cell is switched from one operating mode to another.

2.2 MATHEMATICAL MODEL
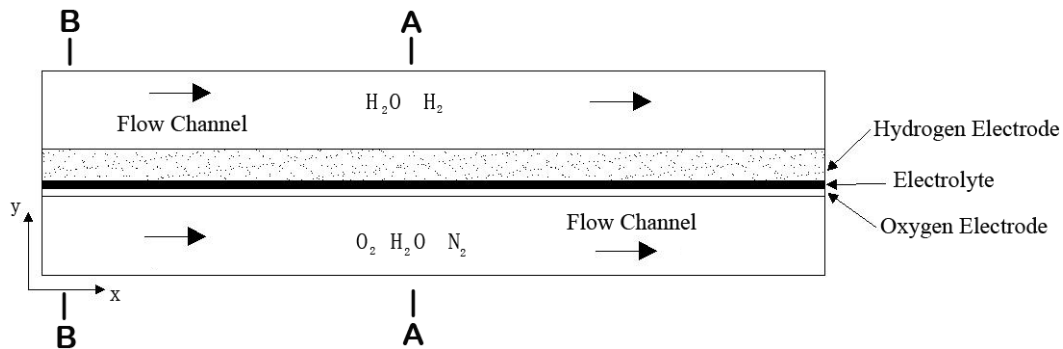
Figure 2.1 Schematic of a 2D planar SOFC

The geometry of a planar 2-D hydrogen electrode supported solid oxide cell is illustrated in Figure 2.1, including flow channels and PEN assembly. Since the cell could be operated in either fuel cell mode or electrolysis mode, steam (H_2O) is assumed in both hydrogen channel and oxygen channel. As a result, gases in hydrogen electrode side are

the mixture of H_2 and H_2O while those in oxygen electrode side are the mixture of H_2O, O_2 and N_2. In the model, we assume isothermal conditions; the reactant gas mixtures are approximated as ideal gases; composite electrodes are assumed so that electrochemical reaction sites are uniformly distributed in hydrogen and oxygen electrodes.

For SOFC mode, oxygen flows into oxygen channel and diffuses into porous oxygen electrode, where oxygen molecules combine with electrons coming from external circuit, and forms into oxygen ions. The oxygen ions migrate through the dense electrolyte to the hydrogen electrode. At the hydrogen side, steam and hydrogen flow into the hydrogen channel. The hydrogen then diffuses into porous hydrogen electrode, where hydrogen molecules combine with oxygen ions coming from the oxygen electrode, and form into steam and release electrons. The electrons then transport through external circuit from hydrogen electrode to oxygen electrode. As a result, electricity is generated. When an external voltage, greater than the open circuit potential of a SOFC, is applied to the cell, the SOFC mode of the cell is switched to SOEC mode. In this scenario, the internal transport and electrochemical reactions will reverse. Specifically, steam at the porous hydrogen electrode is split into hydrogen molecules and oxygen ions with a supply of electrons from external circuit. The oxygen ions then migrate via the dense electrolyte to the oxygen electrode, where oxygen ions then form into oxygen molecules and release electrons. The electrons then transport from oxygen electrode to hydrogen electrode through external circuit. During the process, hydrogen and oxygen are produced and electricity is consumed. The corresponding mathematical model, describing the transport and electrochemical processes within a solid oxide cell operated in both SOFC mode and SOEC mode, is detailed as follows.

2.2.1 Charge Balance

Both electronic and ionic transports are allowed in composite electrodes, while electrolyte only allows ions to migrate through. According to the generalized Ohm's law, the governing equations for charge balance can be described as,

$$\nabla(-\sigma_e \nabla \phi_e) = \pm S_a i_{ict} \tag{2-1}$$

$$\nabla(-\sigma_i \nabla \phi_i) = \pm S_a i_{ict} \tag{2-2}$$

Where σ_e and σ_i are electronic and ionic conductivities, ϕ_e and ϕ_i are electronic and ionic potentials respectively. S_a the effective triple phase boundary (TPB) length. The signs in the right side of Equations (2-1) and (2-2) is dependent on the cell mode. In SOFC mode, oxygen electrode serves as ion sources and electron sinks, while hydrogen electrode serves as ion sinks and electron sources. In SOEC mode, the sources and sinks will be reversed.

i_{ict} in Equations (2-1) and (2-2) is the current density and is represented using Bulter-Volmer equation. For SOFC mode,

$$i_{h,ct} = i_{0,h}[x_{h_2} \frac{c_t}{c_{h_2,ref}} \exp(\frac{0.5F}{RT}\eta_h) - x_{h_2o} \frac{c_t}{c_{h_2o,ref}} \exp(\frac{-0.5F}{RT}\eta_h)] \tag{2-3}$$

$$i_{o,ct} = i_{0,o}[x_{o_2} \frac{c_t}{c_{o_2,ref}} \exp(\frac{0.5F}{RT}\eta_o) - \exp(\frac{-0.5F}{RT}\eta_o)] \tag{2-4}$$

For SOEC Mode,

$$i_{h,ct} = i_{0,h}[x_{h_2o} \frac{c_t}{c_{h_2o,ref}} \exp(\frac{0.5F}{RT}\eta_h) - x_{h_2} \frac{c_t}{c_{h_2,ref}} \exp(\frac{-0.5F}{RT}\eta_h)] \tag{2-5}$$

$$i_{o,ct} = i_{0,o}[\exp(\frac{0.5F}{RT}\eta_o) - x_{o_2} \frac{c_t}{c_{o_2,ref}} \exp(\frac{-0.5F}{RT}\eta_o)] \tag{2-6}$$

16

Here η_h and η_o are overpotentials in H_2 electrode and O_2 electrode respectively, and are defined in Table 2.1 for SOFC mode and SOEC mode.

Table 2.1 The signs of the equations for SOFC and SOEC modes

Mode	SOFC mode		SOEC mode	
Electrode	Hydrogen Electrode	Oxygen Electrode	Hydrogen Electrode	Oxygen Electrode
$\nabla(-\sigma_1 \nabla \phi_{electronic}) = \pm S_a i_{ict}$	-	+	+	-
$\nabla(-\sigma_2 \nabla \phi_{ionic}) = \pm S_a i_{ict}$	+	-	-	+
$\eta = \pm(\phi_{electronic} - \phi_{ionic} - \Delta\phi_{eq})$	+	-	-	+
Source term for O_2	N/A	-	N/A	+
Source term for H_2O	+	0	-	0
Source term for N_2	0	0	0	0
Source term for H_2	-	N/A	+	N/A

N/A: not applicable.

2.2.2 Multicomponent Transport

The gas transport is described by the Maxwell-Stefan's diffusion and convection equations,

$$\rho \frac{\partial \omega_i}{\partial t} + \nabla \cdot (\omega_i \rho u - \rho \omega_i \sum_{j=1}^{k} D_{ij}(\frac{M}{M_j}(\nabla \omega_j + \omega_j \frac{\nabla M}{M}) + (x_j - \omega_j)\frac{\nabla p}{p})) = R_i \quad (2\text{-}10)$$

Where ω_i is the weight fraction of species i. The source term R_i is determined by the electrochemical reactions according to the Faraday's law [81].

$$R_i = \nu_i \frac{i_{ct,i} M_i}{n_i F} \quad (2\text{-}11)$$

2.2.3 Gas-Flow Equations

The weakly compressible Navier-Stokes equations govern the flows in the open channels,

$$\rho \frac{\partial u}{\partial t} + \rho(u \cdot \nabla)u = \nabla \cdot [-pI + \mu((\nabla u + (\nabla u)^T) - \frac{2}{3}(\nabla \cdot u)I)] \quad (2\text{-}12)$$

$$\frac{\partial \rho}{\partial t} + \nabla \cdot (\rho u) = Q \tag{2-13}$$

where μ is the dynamic viscosity, I the momentum.

In porous electrodes, the Brinkman equation is used to describe the flow,

$$\rho \frac{\partial u}{\partial t} + (\frac{\mu}{\kappa} + Q)u = \nabla \cdot [-pI + \frac{\mu}{\varepsilon}(\nabla u + (\nabla u)^T - \frac{2}{3}(\nabla \cdot u)I)] \tag{2-14}$$

$$\frac{\partial \rho}{\partial t} + \nabla \cdot (\rho u) = Q \tag{2-15}$$

where ε and κ denote, respectively, the porosity and permeability of the electrodes, *Q,* the mass source term, is related to the charge transfer current density,

$$Q = \sum_i S_a \frac{i_{ct,i} M_i}{n_i F} \tag{2-16}$$

2.3 EXPERIMENTAL AND MODEL VALIDATION

The V-I curves are first obtained using an in-house prepared cell. In the experimental, the powder mixture of NiO-YSZ and organic additives were dry-pressed into a pellet as hydrogen electrode substrate. A layer of YSZ powder was put on the surface of the substrate, co-pressed to form bilayer structure consisting of hydrogen electrode and electrolyte. The bilayer structure was then sintered at $1450^0 C$ in air for 5h. The $La_{0.8}Sr_{0.2}MnO_3$ (LSM) powders synthesized by a glycine–nitrate–process (GNP) were intimately mixed and ground with fine YSZ powders and organic additives to form an ink, with which the YSZ electrolyte surface of the YSZ/NiO–YSZ bilayer was painted and fired at 1250 ^{o}C for 2 h to form oxygen electrode. The obtained button cell has a diameter of 12 mm, oxygen electrode area of 0.35 cm^2, hydrogen electrode thickness of 400 μm, electrolyte thickness of 30 μm and oxygen electrode thickness of 50 μm, respectively. The cell was then tested in both SOFC mode and SOEC mode. In SOFC

mode, the mixture of 70% vol H_2 and 30% H_2O was used as a fuel, the ambient air as the oxidant. After sweeping a V-I curve in SOFC mode, the applied voltage increased so that SOFC mode was switched to SOEC mode. The corresponding V-I curves were recorded in different temperature conditions as shown in Figure 2.2.
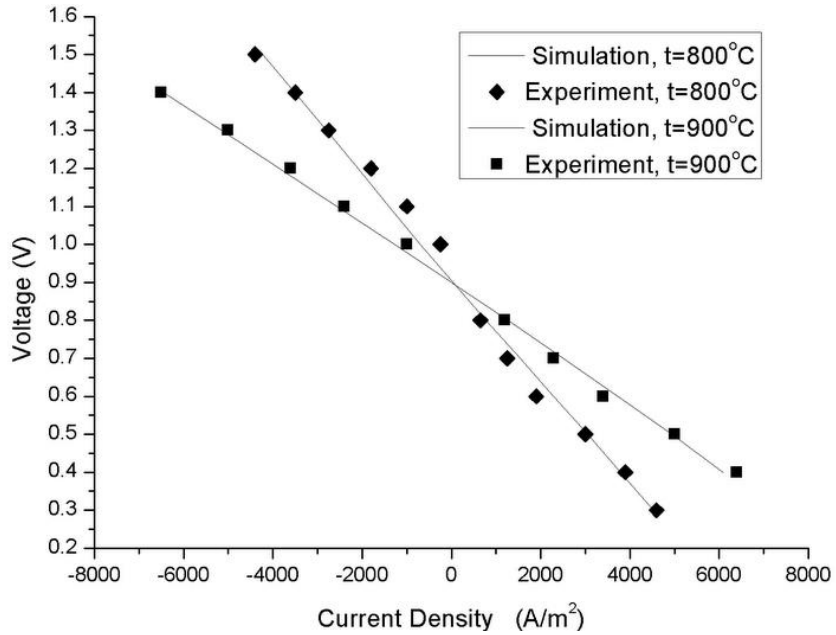
Figure 2.2 Comparisons of model predictions with experimental results

The mathematical model is solved using COMSOL Multiphysics 3.5. The physical parameters used in the model are summarized in Table 2.2. The parameters denoted by "**" are difficult to determine in the experiment and are used as adjustable parameters to fit the model predictions with experimental results. As shown in Figure 2.2, the simulation results agree very well with experimental results. The overall consistency between the experimental data and the simulated results indicates that the present model is reasonable. While the model may need further validation for general planar solid oxide cells, the physical parameters obtained here will be employed for numerical analysis in different cell geometry dimensions.

Table 2.2 Physical parameters used in the model

Parameters	Values	Explanation
d_h *	6.0×10^{-4} [m]	Thickness of hydrogen electrode
d_o *	1.0×10^{-4} [m]	Thickness of oxygen electrode
$d_{electrolyte}$ *	1.0×10^{-4} [m]	Thickness of electrolyte
L_{cell} *	0.019 [m]	Length of the cell
ξ	0.3	Volumetric fraction of ion conductor
ε	0.4	Porosity
σ_i	$33400 \times \exp(-10300/T) \times \xi$ [S/m]	Ionic conductivity
$\sigma_{e,h}$	$2 \times 10^6 \times (1 - \varepsilon - \xi)$ [S/m]	Electronic conductivity in H_2 electrode
$\sigma_{e,o}$	$\dfrac{4.2 \times 10^6}{T} \exp(\dfrac{-11500}{T}) \times (1 - \varepsilon - \xi)$ [S/m]	Electronic conductivity in O_2 electrode
$\sigma_{i,electrolyte}$	$33400 \times \exp(-10300/T) \times \xi$ [S/m]	Electrolyte conductivity
$i_{0,o}$ **	$1[A/m^2]$	Exchange current density in H_2 electrode
$i_{0,h}$ **	$0.1[A/m^2]$	Exchange current density in O_2 electrode
S_a **	$10^9[1/m]$	Specific surface area

* 2D planar SOFC geometry dimensions for simulations in switching mode conditions
** The parameters are adjustable.

2.4 RESULTS AND DISCUSSIONS
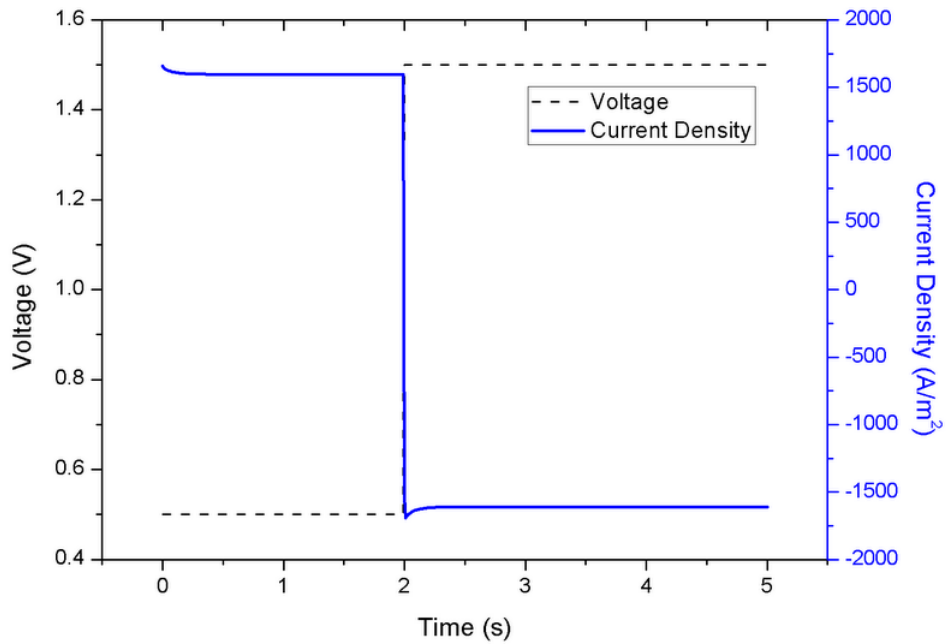
Figure 2.3 Transient responses of voltage and current density in switching mode

In general, it is very difficult for experimental method to measure internal transport and reaction processes within solid oxide cells, especially during the transient process of operating mode switching. The mathematical model developed above will be employed to investigate these performances. In the simulation, the cell is first operated under SOFC mode with the cell voltage setting at 0.5V. At the time of 2 second, the cell voltage is subject to a sudden step change from 0.5V to 1.5V, as a result, the cell SOFC mode is changed to SOEC mode. Correspondingly, the cell current density decreases from 1700A/m^2 at SOFC mode to -1600A/m^2 at SOEC mode as shown in Figure 2.3.
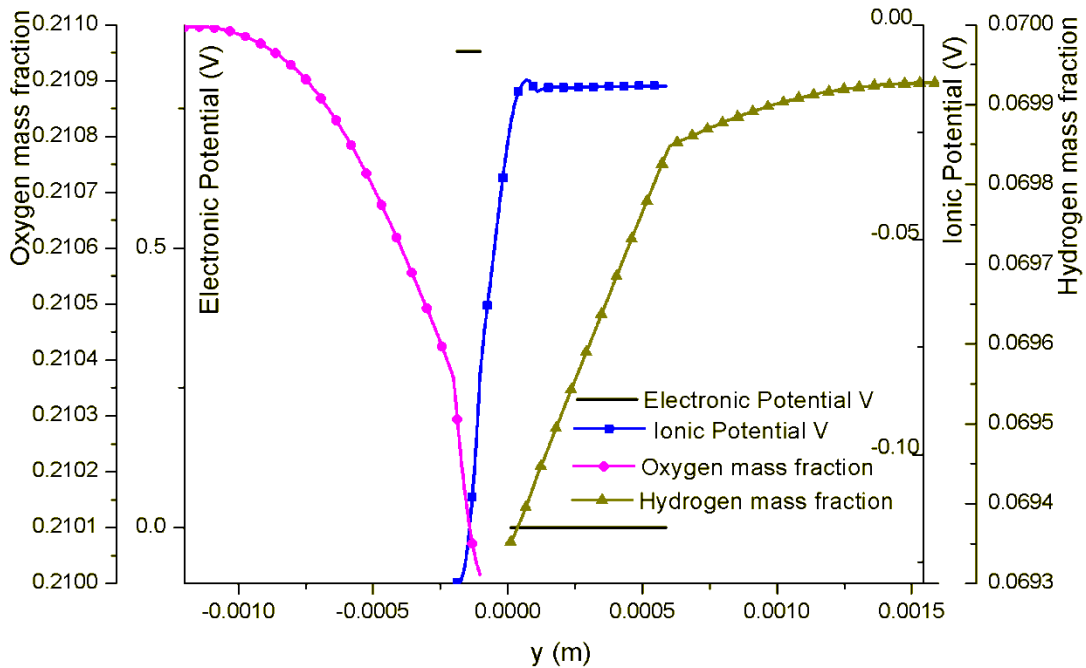
Figure 2.4 Parameter distributions along A-A at 2nd second

In order to examine the internal transport process changes induced by the sudden step increasing of cell voltage, the internal parameter distributions are obtained along a line parallel to y-axis at x = 0.009m (line A-A as shown in Figure 2.1). At the time of 2 second, the cell is in SOFC mode, the corresponding parameter distributions are shown in

Figure 2.4. Due to the hydrogen and oxygen consumptions by electrochemical reactions, hydrogen and oxygen mass fractions decrease from respective channels towards electrode/electrolyte interfaces. At the oxygen electrode, ionic potential increases from channel/electrode interface towards the electrode/electrolyte interface. Within the electrolyte, ionic potential keeps increasing from oxygen electrode side towards hydrogen electrode side. At hydrogen electrode, ionic potential is around -0.0125V with a slight variation. The electronic potential keeps at 0V level at H_2 electrode while reaching 0.87V at O_2 electrode in SOFC mode.
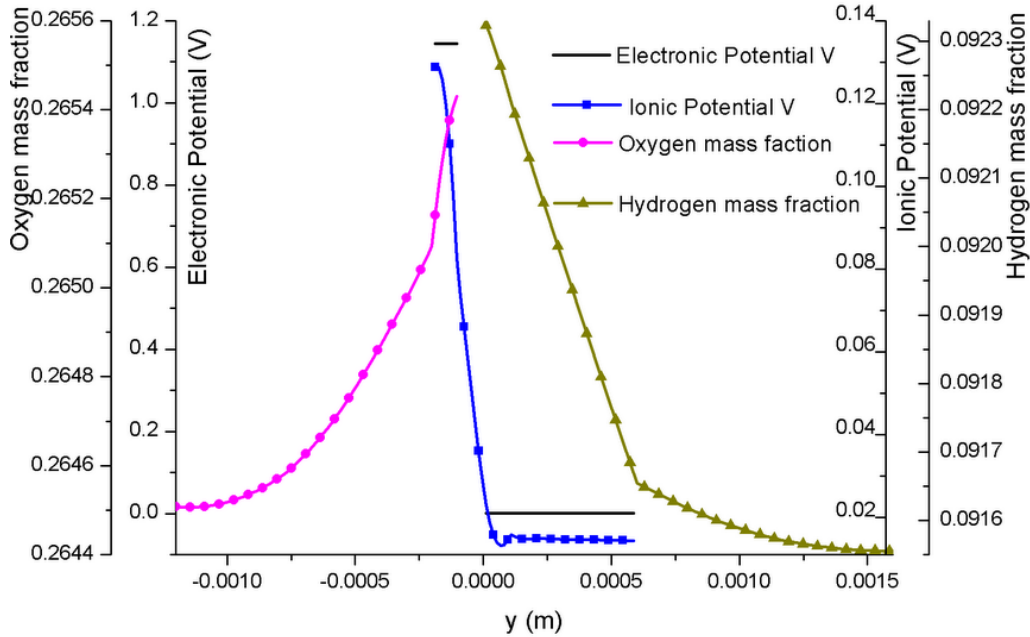
Figure 2.5 Parameter distributions along A-A at 5th second

Once the cell voltage is increased to 1.5V, the SOFC mode is switched to SOEC mode. The corresponding parameter distributions are shown in Figure 2.5. Since H_2 and O_2 are generated in SOEC mode, the trend of corresponding mass fractions flips when compared to those in Figure 2.4, which increase from channels towards electrode/electrolyte interface along the A-A. The ionic potential distribution also shows an opposite trend to that in Figure 2.4. The electronic potential is 0V at H_2 electrode, but

22

reaches about 1.15V at O_2 electrode. Obviously, except for electronic potential, the rest of parameter distributions show opposite trend to those in Figure 2.4.

Figure 2.6 shows the evolution history of O_2 mass fraction distribution along the line parallel to y-axis at x = 0.002m (line B-B in Figure 2.1) during the transient process of cell mode switching. At 1.99[th] second, the cell is in SOFC mode, O_2 mass fraction decreases from the channel towards the electrode/electrolyte interface. At 2.01[st], the overall O_2 mass fraction increases meanwhile the trend of the distribution flips, which increases from the channel towards the electrode/electrolyte interface due to the fact that the cell starts to generate oxygen. At 2.1[st], the cell is still in transient process and the O_2 mass fraction further increases. At 5th second, the cell reaches the steady-state SOEC mode with maximum O_2 mass fraction distribution.
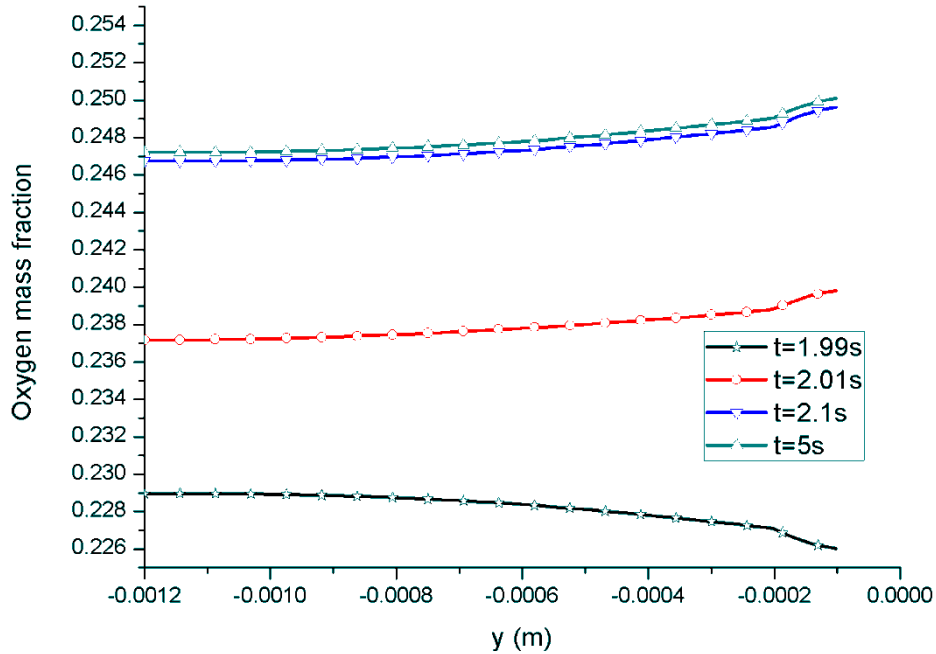
Figure 2.6 Evolution history of oxygen mass fraction distribution along B-B

Figure 2.7 shows the corresponding evolution histories of H_2 mass fraction distributions, which have the similar trends to those of O_2 mass fraction distributions in

Figure 2.6. At the 1.99th second, the cell is in SOFC mode, H_2 mass fraction shows the decreasing trend from the channel towards the electrode/electrolyte interface along B-B due to H_2 consumptions by electrochemical reactions. During the switching process from SOFC mode to SOEC mode, H_2 mass fraction distribution reverses and shows an increasing trend from the channel towards electrode/electrolyte interface at 2.01st second. The overall H_2 mass fraction distribution increases and reaches a steady-state at 5th second.
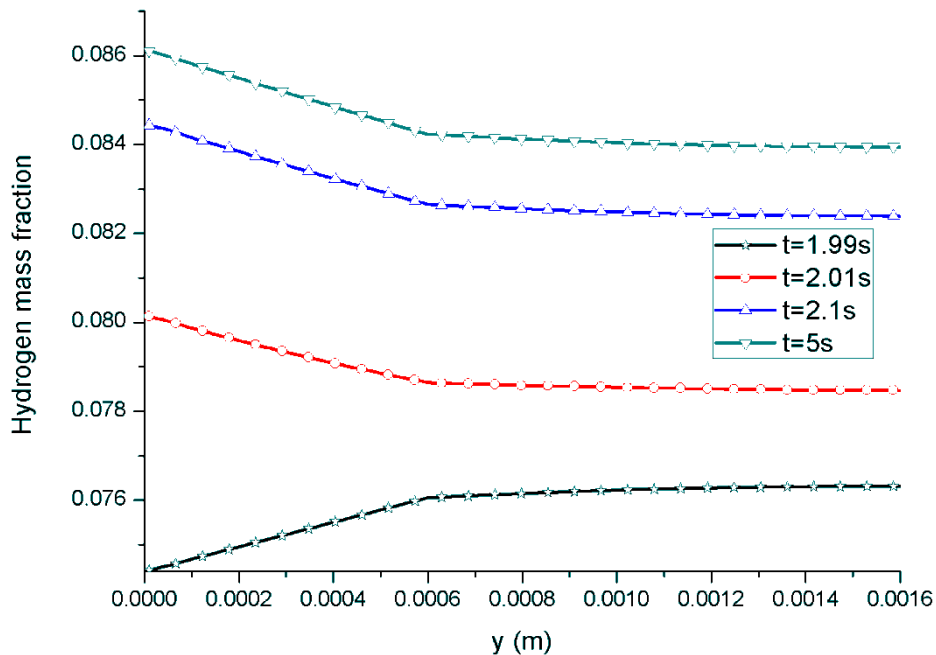
Figure 2.7 Evolution history of hydrogen mass fraction distribution along B-B

The mass fraction distribution of water vapor in hydrogen side is shown in Figure 2.8. In SOFC mode at 1.99th second, the distribution has an increasing trend from the channel towards the electrode/electrolyte interface because water vapor is generated at this electrode. Once the cell is switched to SOEC mode, water vapor is consumed by electrochemical reactions. Consequently its distribution decreases from the channel towards the electrode/electrolyte interface. Water vapor distribution keeps decreasing

from 2.01st second to 2.1st second, and then increases and reaches a steady state at 5th second. Obviously the evolution of water vapor experiences an overshoot around the 2.1st second. In comparison, H_2 mass fraction distribution in Figure 2.7 doesn't experience such an overshoot. The reason is that H_2O is heavier than H_2, the big inertia of H_2O leads to such an overshoot phenomenon.
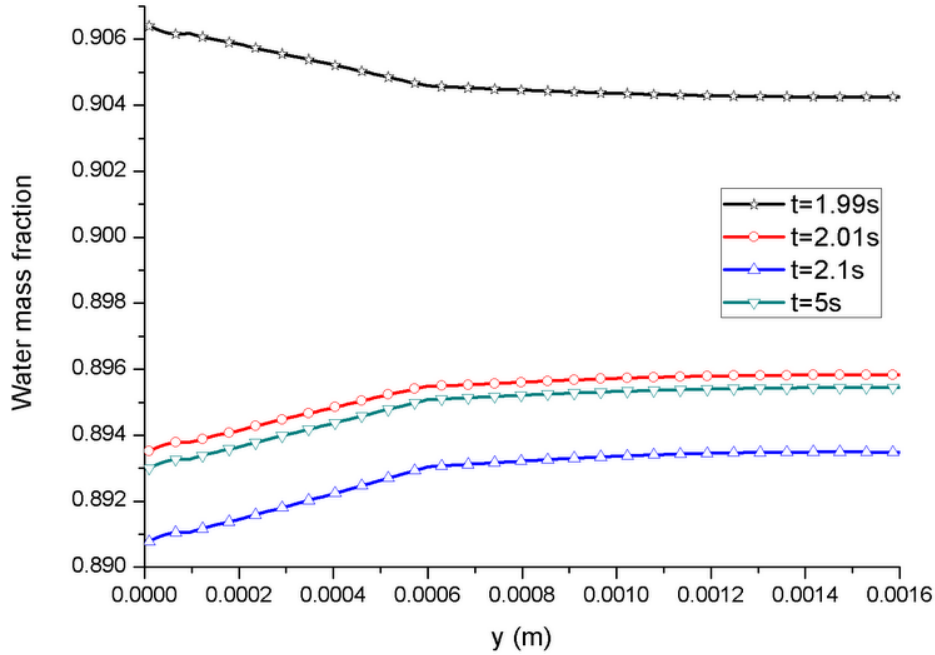
Figure 2.8 Evolution history of water vapor mass fraction distribution along B-B

Figure 2.9 shows the evolution history of electronic potentials along B-B. Essentially, the electronic potential at H_2 electrode keeps at 0V, while those at O_2 electrode changes. During the transient process of the mode switching, electronic potential increases from 0.62V at SOFC mode to 1.36V at SOEC mode and reaches maximum value at 5th second.
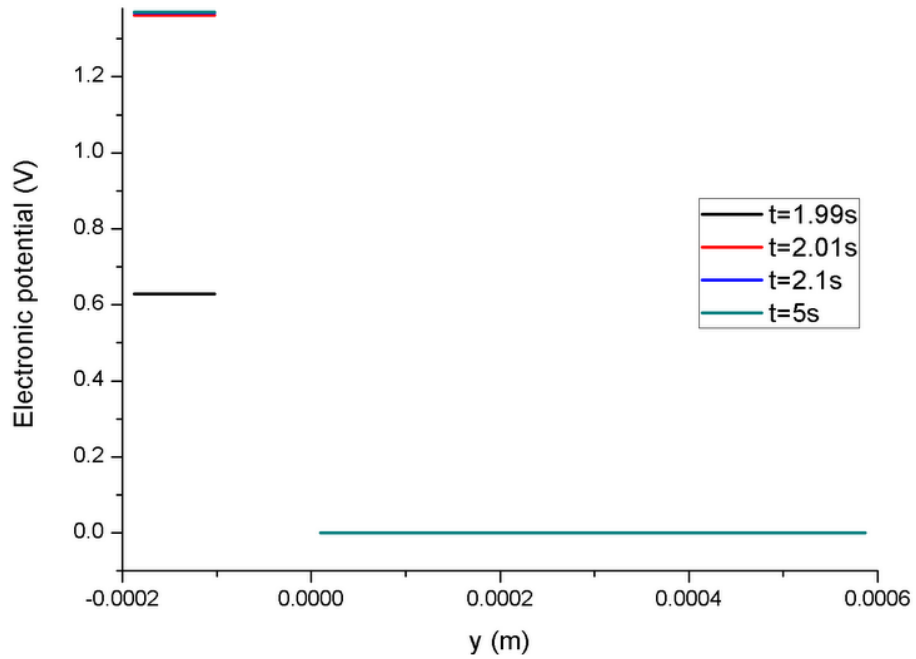
Figure 2.9 Evolution history of electronic potential distribution along B-B
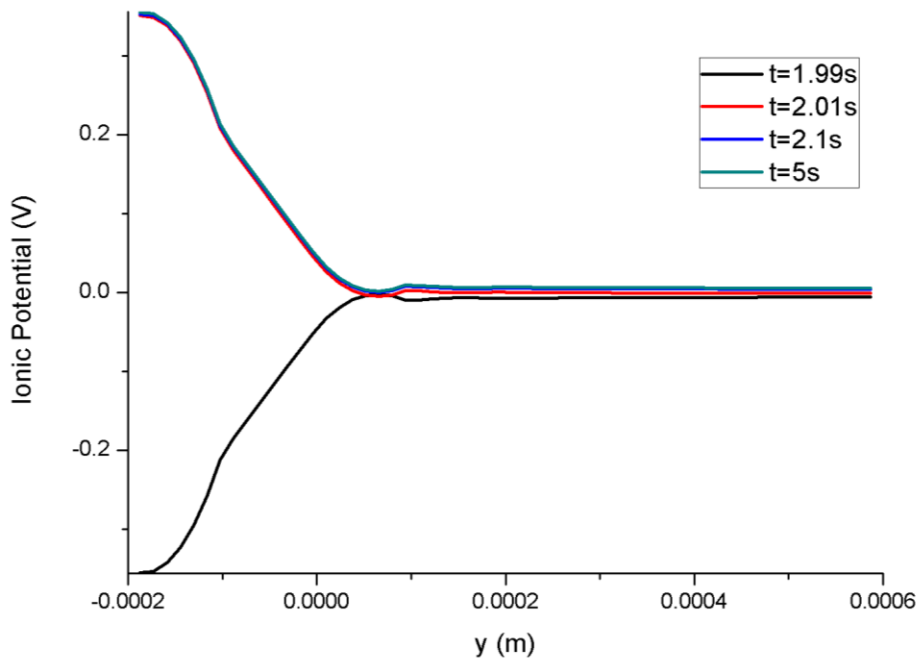
Figure 2.10 Evolution history of ionic potential distribution along B-B

Figure 2.10 shows the evolutions of corresponding ionic potential distributions along B-B. At SOFC mode (1.99[th] second), the ionic potential at channel/O_2 electrode interface is about -0.36V. It increases towards H_2 electrode. Beyond H_2

26

electrode/electrolyte interface, ionic potential keeps increasing, followed by a little bit of variations, it then reaches around 0V. Once the operating mode starts to switch from SOFC mode at 1.99^{th} second to SOEC mode at 2.01^{st} second, ionic potential immediately flips around 0V to positive values. During the following transient process of mode switching, ionic potentials almost keep unchanged.

2.5 CONCLUSION

In this research, an isothermal 2D transient mathematical model is developed for solid oxide cells, which are operated in both SOFC mode and SOEC mode. The model is validated using experimental results of in-house prepared NiO-YSZ/YSZ/LSM cell under different operating temperatures. The model is employed to investigate complicated multi-physics processes during the transient process of mode switching. Simulation results indicate that the trends of internal parameter distributions, including $H_2/O_2/H_2O$ and ionic potentials, flip when the operating cell is switched from SOFC mode to SOEC mode. However, the electronic potential shows different behaviors. At H_2 electrode, electronic potential keeps at zero voltage level, while at O_2 electrode, electronic potential increases from a relatively low level in SOFC mode to a relatively high level in SOEC mode. Transient results also show that an overshoot occurs for mass fraction distribution of water vapor at H_2 side when the operating cell switches from SOFC mode to SOEC mode. The mass fractions of O_2 and H_2 as well as charge potentials (electronic and ionic) may quickly follow the operating mode changes. The simulation results presented in this research facilitate the internal mechanism understanding for regenerative SOFCs.

CHAPTER 3

COMPUTATIONAL FLUID DYNAMICS ANALYSIS OF SOLID OXIDE

ELECTROLYSIS CELLS WITH DELAMINATIONS

3.1 INTRODUCTION

The hydrogen has been identified as an important energy carrier, and could play a significant role in future clean energy technology such as fuel cells [101]. Hydrogen can be produced through several methods, e.g., thermal reforming, photoelectrochemical water splitting, etc., among which direct water electrolysis through the reverse process of fuel cells is widely recognized as a clean and sustainable method. PEM electrolysis cell and solid oxide electrolysis cell (SOEC) are two popular methods in this respect. Since SOEC is ceramic cell, it can sustain high operating temperatures and consequently may provide more advantages than low temperature electrolysis cells, such as high reaction rate, high kinetic energy, and high conversion efficiency, etc. In particular, there is an increasing interest in using nuclear energy for hydrogen generation in an efficient and environmentally friendly way, where the high temperature steam generated from nuclear plant can be directly utilized by SOECs for hydrogen generation [102-106].

Hydrogen production through SOECs has been investigated using both experimental method and numerical modeling method. Since very complex transport and electrochemical reaction processes take place simultaneously within SOECs, modeling method, as an important complementary to experimental method, plays an increasing role

in de-convoluting the coupled multi-physics processes and understanding the working mechanisms. In this respect, mathematical models at different levels were developed to investigate SOEC steady state performance [98, 99, 107, 108] and dynamic performance [94, 96]. In order to better understand multi-physics processes, detailed parameter distributions, and their effects on SOEC performance, computational fluid dynamics (CFD) models were employed. Hawkes et al. [109] employed CFD modeling method to study the operating voltage effects on the distributions of gas compositions, current density, and temperature of SOEC stack. Ni [100] developed a 2D CFD model and studied the effects of gas velocity and electrode microstructure on SOEC performance. All of these studies represent significant progresses on SOEC modeling and numerical analysis.

The basic structure of SOECs is a tri-layer positive electrode-electrolyte-negative electrode (PEN) assembly, in which the dense electrolyte is sandwiched by porous electrodes on either side. In order to perform water electrolysis, the functional material is different from one layer to another. Since different material has different thermal expansion coefficient (TEC), the thermal stresses generated at electrode/electrolyte interface might cause the detachment of adjacent layers when SOECs experience long-term elevated temperature conditions or dynamic thermal cycling conditions, leading to delamination phenomenon. Experimental observations show that delamination occurs at oxygen electrode/electrolyte interface in durability tests [110]. Upon the occurrence of delamination, the cell performance deteriorates because the interface open gap, perpendicular to the main current path, consists of an insulating barrier to charge conduction, and destroys electrochemical reaction sites. While significant progresses have been made toward mechanism understanding of SOECs as mentioned above,

including experiment and mathematical modeling, few studies can be found in open literatures on how to quantitatively interpret delamination effects on SOEC performance.

In this study, a comprehensive 2-D CFD model is developed and is employed for performance simulation of SOECs. The size and location of delamination effects on local parameter distributions as well as SOEC polarization performance are studied systematically. This research is significant for quantitative understanding of delamination phenomenon and SOEC performance tolerance on delamination failure.

3.2 MATHEMATICAL MODEL DEVELOPMENT
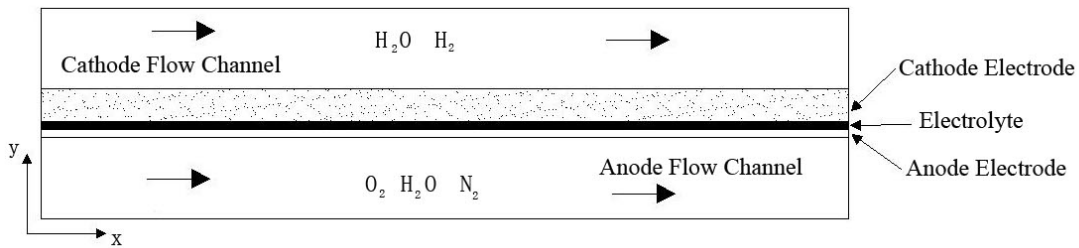
Figure 3.1 Schematic of a 2D planar SOEC

Figure 3.1 shows a 2-D planar SOEC composed of PEN assembly and two flow channels (cathode and anode). During operations, an electric potential sufficient for electrolysis is applied to the SOEC. Vapor/hydrogen gas mixture and air are supplied to the cathode and anode flow channels, respectively. At the cathode (hydrogen) side, vapor molecules transport through the porous cathode layer to the triple phase boundary (TPB) site, where the gas phase, electronic conducting material, and ionic conducting material meet together, and vapor is dissociated into hydrogen molecules and oxygen ions with a supply of electrons from external circuit. The hydrogen molecules then diffuse out of porous cathode electrode into the channel. The oxygen ions subsequently migrate to the anode (oxygen) side through the dense electrolyte. At TPB sites of the anode electrode, oxygen ions release electrons and form into oxygen molecules. The oxygen molecules

30

then diffuse out of porous anode into the channel while the released electrons transport to the cathode side through external circuit.

In mathematical model development, we make the following assumptions: operating conditions are steady state; the reactant gas mixtures are approximated as ideal gases; active reaction sites (TPB sites) are uniformly distributed through porous electrodes. Based on these assumptions and 2D SOEC geometric settings shown in Figure 3.1, the model, detailed as follows, includes the coupled processes of charge (ion/electron) balance, electrochemical reaction kinetics, mass balance, and momentum and energy balances.

3.2.1 Charge Balance

Charge transport includes ionic and electronic transports. Since composite electrodes are assumed, both electronic and ionic transports are allowed in anode and cathode electrodes, while electrolyte only allows ions to migrate through. According to the Ohm's law, the governing equations for charge balance can be described as:

$$\text{Electronic charge:} \begin{cases} \text{Anode electrode layer}: \nabla \cdot \left(\sigma_a^{eff} \nabla \phi_e \right) = i_{a,ct} A_V \\ \text{Cathode electrode layer}: \nabla \cdot \left(\sigma_c^{eff} \nabla \phi_e \right) = -i_{c,ct} A_V \end{cases} \quad (3\text{-}1)$$

$$\text{Ionic charge:} \begin{cases} \text{Electrolyte layer}: \nabla \cdot \left(\kappa_i \nabla \phi_i \right) = 0 \\ \text{Anode electrode layer}: \nabla \cdot \left(\kappa_a^{eff} \nabla \phi_i \right) = -i_{a,ct} A_V \\ \text{Cathode electrode layer}: \nabla \cdot \left(\kappa_c^{eff} \nabla \phi_i \right) = i_{c,ct} A_V \end{cases} \quad (3\text{-}2)$$

Where ϕ_e and ϕ_i are electronic and ionic potentials respectively; σ^{eff} and κ^{eff} are effective electronic and ionic conductivities in cathode and anode regime self-explained with subscripts a (anode) and c (cathode) respectively; A_V the volumetric reactive surface

area; the effective ionic and electronic conductivities in the electrode layers are defined as [84]:

$$\sigma^{\text{eff}} = \xi(\frac{1-\varepsilon}{\tau})\sigma_{\text{e}} \tag{3-3}$$

$$k^{\text{eff}} = (1-\xi)(\frac{1-\varepsilon}{\tau})k_{\text{i}} \tag{3-4}$$

Here, ξ is the volume fraction of electron conducting material in porous electrode; ε and τ are porosity and tortuosity of porous electrodes respectively; σ_{e} and k_{i} are intrinsic conductivities of electron conducting material and ion conducting material.

The $i_{c,ct}$ and $i_{a,ct}$ in equations (3-1) and (3-2) are local charge transfer current densities in cathode and anode electrodes respectively, and can be calculated using generalized Butler-Volmer equation.

$$i_{ct} = i_0 \left(\frac{c_{react}}{c_{react-chanl}} \exp\left(\frac{\alpha n_e F \eta_{ao}}{RT} \right) - \frac{c_{prod}}{c_{prod-chanl}} \left(-\frac{(1-\alpha)n_e F \eta_{ao}}{RT} \right) \right) \tag{3-5}$$

$$\eta_{\text{ao}} = \phi_{\text{e}} - \phi_{\text{i}} - \Delta\phi_{\text{eq}} \tag{3-6}$$

Where c_{react}, c_{prod}, $c_{\text{react-chanl}}$ and $c_{\text{prod-chanl}}$ are the reactant concentration and product concentration, self-explained with subscript, at the reaction sites and the channel-electrode interface respectively. At cathode side, the reactant and product are vapor and hydrogen, while at anode side, the product is oxygen. α is the charge transfer coefficient $(0 < \alpha < 1)$. n_{e} is the moles of electrons transferred per mole reactant. F is the Faraday's constant. η_{ao} is the activation overpotential representing electrode kinetics at the reaction site; ϕ_{ref} is the relative potential difference between the electronic and ionic conductors from the reference state. R the gas constant; T the operating temperature; i_0, the exchange

current density, is defined as the current density of the charge-transfer reaction at the dynamic equilibrium potential; $\Delta\phi_{eq}$ is the equilibrium potential difference. At cathode-channel/electrode interface, the potential is fixed at a reference potential of zero, while at anode-channel/electrode interface, a voltage V_{cell}, sufficient for electrolysis, is applied.

3.2.2 Mass/species conservation

Since multi-species are involved in anode and cathode channels and electrodes, multi-species Maxwell-Stefan's equation is employed to describe the corresponding transport phenomena.

$$\nabla(\omega_i\rho u - \rho\omega_i\sum_{j=1}^{k}D_{ij}(\frac{M}{M_j}(\nabla\omega_j + \omega_j\frac{\nabla M}{M}) + (x_j - \omega_j)\frac{\nabla p}{p})) = R_i \qquad (3\text{-}7)$$

Where R_i is the reaction source term for species i, ω_i the weight fraction of species i, x_j the molar fraction of species j. D_{ij} represents the binary diffusion coefficient for a pair of species i and j, and is used to characterize species diffusion, and can be described as,

$$D_{ij} = \frac{1.43e^{-8}T^{1.75}}{pM_{ij}^{\frac{1}{2}}(V_i^{\frac{1}{3}} + V_j^{\frac{1}{3}})} \qquad (3\text{-}8)$$

Here M_{ij} is the mean molecular mass,

$$M_{ij} = \frac{2}{\frac{1}{M_i} + \frac{1}{M_j}} \qquad (3\text{-}9)$$

The effective diffusion coefficient is employed to characterize multi-species transport in porous electrodes, in which the Knudsen diffusion [111] and the binary diffusion are combined together as,

$$D_{ij}^{eff} = \frac{\varepsilon}{\tau}(\frac{D_{ij}D_{Kn,i}}{D_{ij} + D_{Kn,i}}) \tag{3-10}$$

Here D_{Kn} is the Knudsen diffusion coefficient of species i,

$$D_{Kn,i} = \frac{97}{2}d_{pore}\sqrt{\frac{T}{M_i}} \tag{3-11}$$

The average molecular weight is calculated as:

$$M = \sum_{j=1}^{n}x_jM_j \tag{3-12}$$

When ideal gas is considered, the density can be written as:

$$\rho = \frac{pM}{RT} \tag{3-13}$$

3.2.3 Momentum Conservation

Due to high temperature operating conditions, and normal pressure environment ($p_{out} = 1atm$), the weakly compressible Navier-Stokes equations are assumed to govern fluid flow in channels.

$$\rho(u \cdot \nabla)u = \nabla \cdot [-pI + \mu((\nabla u + (\nabla u)^T) - \frac{2}{3}(\nabla \cdot u)I)] \tag{3-14}$$

$$\nabla \cdot (\rho u) = 0 \tag{3-15}$$

where μ is the dynamic viscosity, I the momentum.

The Brinkman equation is used to describe momentum conservation in porous electrode,

$$(\frac{\mu}{\kappa} + Q)u = \nabla \cdot [-pI + \frac{\mu}{\varepsilon}(\nabla u + (\nabla u)^T - \frac{2}{3}(\nabla \cdot u)I)] \tag{3-16}$$

$$\nabla \cdot (\rho u) = Q \tag{3-17}$$

where κ denotes the permeability of porous electrode; Q is the mass source term induced by electrochemical reactions, which is related to the charge transfer current density according to

$$Q = \sum_i \frac{i_{ct}M_i}{n_i F} \tag{3-18}$$

3.2.4 Energy Conservation

The energy equation, accounting for conduction, convection, and diffusion effect, can be written as,

$$\nabla \cdot (-k\nabla T + \rho C_p Tu + \sum_j h_j N_{D,j}) = Q \tag{3-19}$$

Where k is the thermal conductivity of gas mixture; ρ the density of gas mixture; C_p the specific heat capacity of gas mixture; h_j is the molar enthalpy of the species, and $N_{D,j}$ is the diffusive flux of species *j*, calculated from the species balance equation.

For flows in porous electrode, thermal equilibrium condition is assumed, where the temperature of fluid is the same as that of porous solid in the volumetric average sense. Correspondingly, the thermal conductivities of flow phase and solid phase are combined together to form an effective thermal conductivity,

$$k_{eff} = \varepsilon k_f + (1-\varepsilon)k_s \tag{3-20}$$

Q is the heat source term induced by ohmic heating effect (Q_{ohm}), activation and concentration overpotentials under a non-equilibrium condition ($Q_{act+con}$), as well as entropy change through electrochemical reactions (Q_{ent}) [86].

$$Q = Q_{ohm} + Q_{act+con} + Q_{ent} \tag{3-21}$$

$$Q_{ohm} = \frac{J^2 \cdot A_V}{\sigma} \;;\; Q_{act} = J\eta_{act+con}A_V \;;\; Q_{ent} = JA_V(-\frac{T\Delta S}{2F}) \tag{3-22}$$

where J is the current density, A_v the volumetric reactive surface area (m^{-1}), ΔS the entropy change.

3.3 NUMERICAL SOLUTION AND MODEL VALIDATION
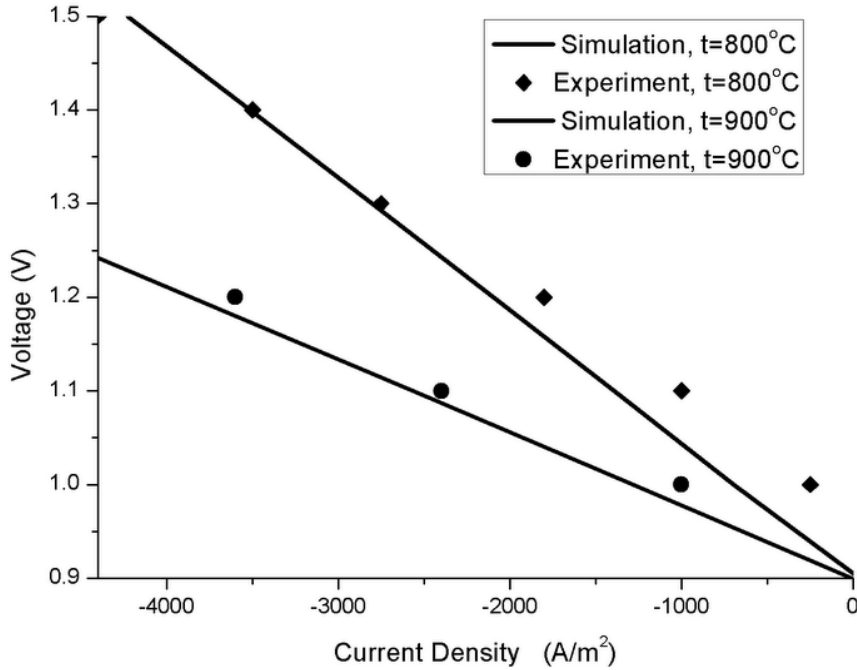
Figure 3.2 Comparisons between experimental results and model simulations

The mathematical model presented in this research is solved using finite element package COMSOL MULTIPHYSICS version 3.5a. For a specified cell voltage at anode electrode boundary, the corresponding cell average current density is calculated. The cell polarization curve is then obtained by specifying a series of cell voltages and calculating the corresponding average current densities.

Model validation with experimental results is very useful to test model behavior upon variation of physical parameters, such as electrode/electrolyte interface delamination failure. For this purpose, we measured polarization performance of an in-house made button cell consisted of a ~500 μm thick Ni-YSZ cermet, ~15μm thick YSZ electrolyte membrane, and 30 μm LSM electrode layer. Hydrogen was used as inlet

carrier gas, which is used to vary the partial pressures of the vapor and as reducing gas to prevent the oxidation of H_2 electrode material (Ni). Hydrogen flow rate was 40 cubic centimeter per minute (cm^3/min) with 50% humidity, controlled by a precision mass flow controller (APEX). The oxygen electrode was exposed to ambient atmosphere. The polarization curve was recorded by Versa-STAT3 system at 800^0C. The experimental result is shown in Figure 3.2. The physical parameters used in the model validation are shown in Table 3.1. The parameters with "**" are difficult to determine in the experiment and are used as adjustable parameters to fit the model predictions with experimental results. The comparison results are shown in Figure 3.2. It can be seen that the numerical results agree very well with experimental results.

Table 3.1 The physical parameters used in the model validation

Parameters	Values	Explanation
d_h*	6.0×10^{-4} [m]	Thickness of Cathode
d_o*	1.0×10^{-4} [m]	Thickness of Anode
$d_{electrolyte}$*	1.0×10^{-4} [m]	Thickness of Electrolyte
L_{cell}*	0.019 [m]	Length of the cell
ξ	0.3	Volumetric Fraction of Ion Conductor
ε	0.4	Porosity
$\sigma_{i,c}$	$33400\times\exp(-10300/T)\times\xi$ [S/m]	Ionic conductivity, Cathode
$\sigma_{e,c}$	$2\times10^6\times(1-\varepsilon-\xi)$ [S/m]	Electronic conductivity, Cathode
$\sigma_{i,a}$	$33400\times\exp(-10300/T)\times\xi$ [S/m]	Ionic conductivity, Anode
$\sigma_{e,a}$	$\dfrac{4.2\times10^6}{T}\exp(\dfrac{-11500}{T})\times(1-\varepsilon-\xi)$ [S/m]	Electronic conductivity, Anode
$\sigma_{i,electrolyte}$	$33400\times\exp(-10300/T)\times\xi$ [S/m]	Electrolyte conductivity
$i_{0,a}$**	1[A/m^2]	Exchange current, Cathode
$i_{0,c}$**	0.1[A/m^2]	Exchange current, Anode
S_a**	10^9[1/m]	Specific surface area

    * 2D planar SOEC geometry dimensions for simulations.
    ** The parameters are adjustable.

3.4 RESULTS AND DISCUSSION

The mathematical SOEC model is then employed to investigate the cell performance. In particular, the study will determine how the size and location of delaminations at electrode/electrolyte interface affect SOEC performance. A delamination failure occurring at oxygen electrode/electrolyte interface is a gas filled gap, in a plane which is perpendicular to the main ionic/electronic current direction. Because of solid material discontinuity induced by delamination, the ionic/electronic conducting path is cutoff locally, the possible TPB sites are also ruined out. Obviously, delamination will influence local mass/charge transport and electrochemical reactions, and consequently affect SOEC performance. It is assumed that charges are not able to jump over the delamination site, as a result, the boundary conditions (BCs) for charge transport are treated as insulated BCs at this site.

3.4.1 Delamination effects with parallel flows
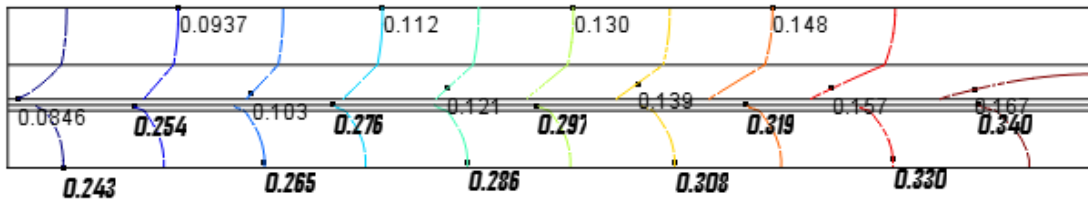
Figure 3.3 Mass Fraction Distributions of Base case with parallel flow

In this case study, the flows in anode and cathode channels are set as parallel flows. Hydrogen mixed with vapor is used as inlet carrier gas and reactant in cathode channel respectively while air is employed as carrier gas in anode channel. The simulation results are shown in Figure 3.3. Due to the electrolysis effect, hydrogen and oxygen are generated in cathode and anode electrodes respectively, as a result, the mass

fraction of hydrogen increases from 0.0846 to 0.167 along the cathode channel while that of oxygen increases from 0.243 to 0.34 along the anode channel.
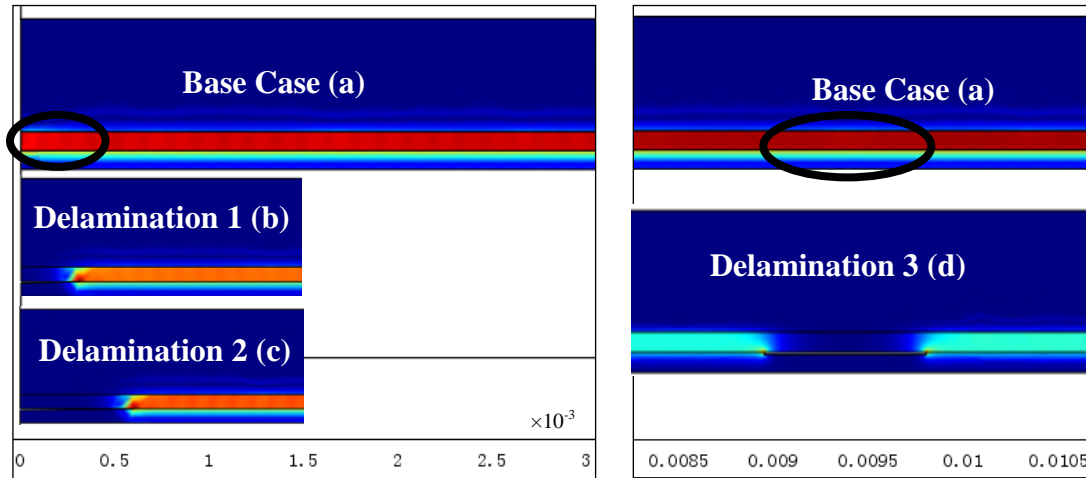
Figure 3.4 Ionic current density distributions: (a) Base case without delamination, (b) With delamination 1, (c) With delamination 2, (d) With delamination 3
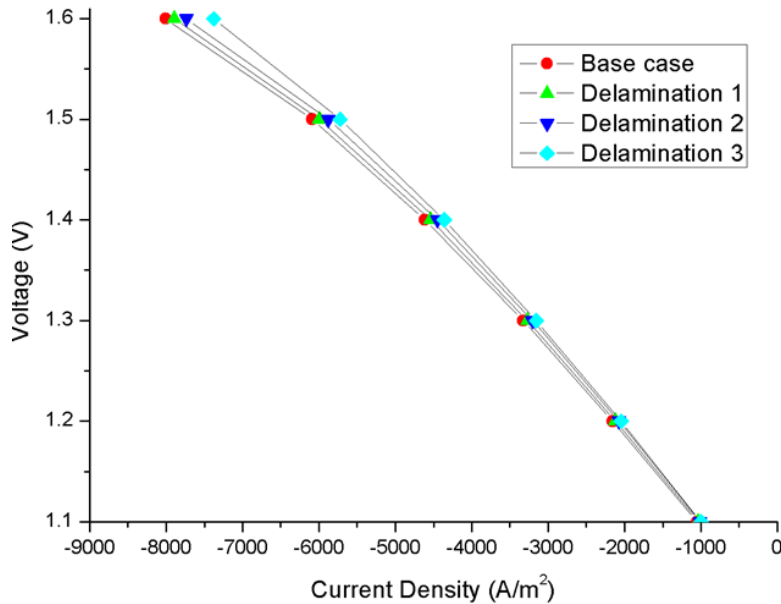
Figure 3.5 SOEC performance sensitivity to delaminations in parallel flow

The corresponding ionic current density distribution is shown in the base case of Figure 3.4. We then introduce delaminations at oxygen electrode/electrolyte interface. The delamination 1 is set at left side near the inlet as shown Figure 3.4(b). The

delamination 2 is set at the same site of delamination 1 but the delamination size is doubled as shown in Figure 3.4(c). The size of delamination 3 is the same as that of delamination 2, however, the location of delamination 3 is set at the center of the cell along the flow direction as shown in Figure 3.4(d). These three delaminations are individually introduced. Comparing ionic current density distribution in base cases and delamination cases, one can see that delaminations cut off the charge transport path and significantly influence local current density distributions. The effect of delaminations on cell polarization performance is shown in Figure 3.5. Both the delamination location and size affect the cell performance. For the parallel flow considered in this case, the cell performance is more sensitive to the delamination at the center of the cell (delamination 3) than that at the inlet of the cell (delamination 1 and 2). For the same delamination location, increasing the delamiantion size (delamiantion 1 to delamination 2) will make the cell performance a little bit worse.

3.4.2 Delamination effects with counter flows
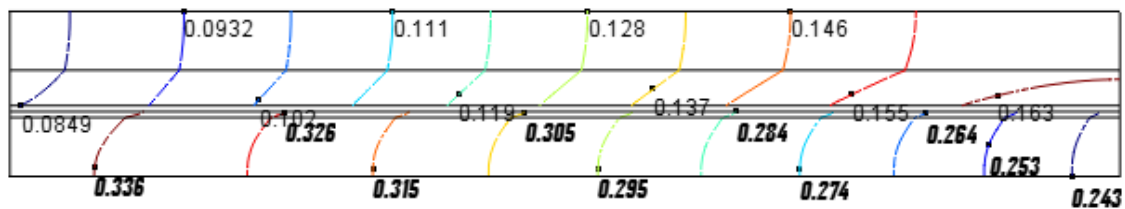
Figure 3.6 Mass fraction distributions of base case with counter flow

As a comparison, counter flow is utilized in this case study, where the mixture of hydrogen and vapor flows through the hydrogen channel from the left side to the right side while air flows through the oxygen channel from the right side to the left side. Without any delaminations, the mass fraction distributions are shown in Figure 3.6. Basically the hydrogen mass fraction increases from 0.0849 to 0.163 along the flow

direction while the oxygen mass fraction increases from 0.243 to 0.336 along the air flow direction.
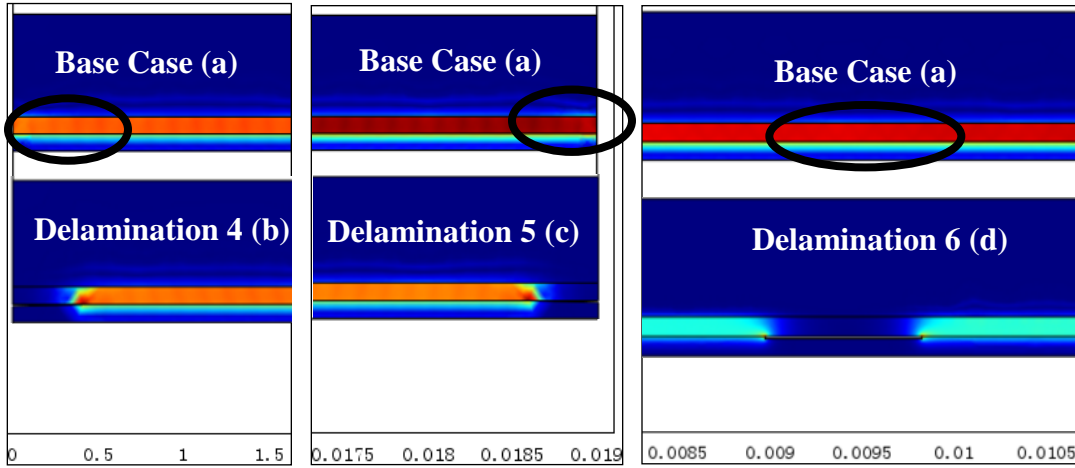
Figure 3.7 Ionic current density distribution: (a) base case, (b) with delamination 4, (c) with delamination 5, (d) with delamination 6

The corresponding ionic current density distributions are shown in Figure 3.7. We then individually introduce three delaminations. Delamination 4 with size 4.0e-4m is set at the oxygen electrode/electrolyte interface at the left end of the cell, delamination 5 with the same size (4.0e-4m) is introduced at the oxygen electrode/electrolyte interface but at the right end of the cell. Finally delamination 6 with size 8.0e-4m is set at the center of the cell along the oxygen electrode/electrolyte interface. The corresponding ionic current density distributions are shown in Figure 3.7(b)(c)(d), respectively. Comparing the base case in Figure 3.7(b)(c)(d), one can see that the local ionic current density distributions are significantly influenced since the charge transport path is cutoff at the delamination site. To highlight the sensitivity of cell performance to the delaminations, the cell V-I curve is obtained under different delamination settings as shown in Figure 3.8. It is clear to see that without delamination, the cell obtains the best performance. Once delamination is introduced, the cell performance gets worse, among

which the cell with delamination 4 obtains similar performance to that with delamination 5 and the cell shows a slight high sensitivity to delamination 5 at relatively high current density conditions. When the delamination 6 is introduced, the cell obtains the worst performance.
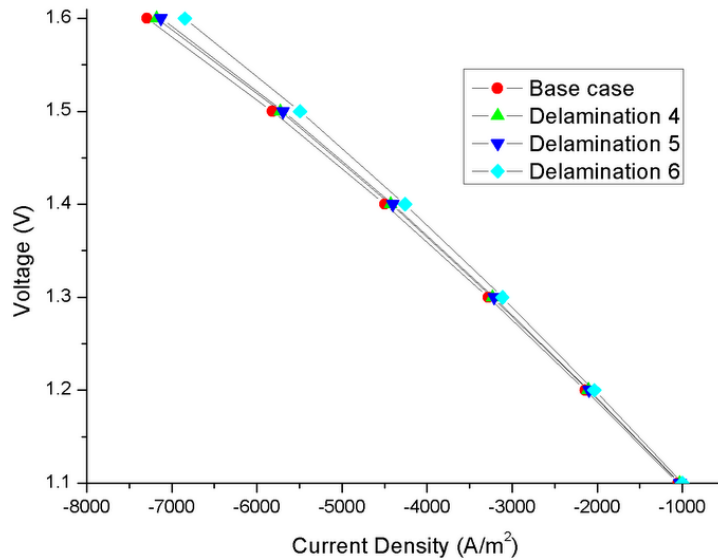
Figure 3.8 SOEC performance sensitivity to delaminations with counter flow

3.5 CONCLUSION

In this research, a 2-D CFD model is developed for a planar SOEC. The model is validated using experimental data of a button cell under different temperatures. The model is utilized to investigate the sensitivity of electrolysis performance to deliminations occurred at oxygen electrode/electrolyte interface. Results indicate that delaminations significantly influence local charge current density distributions since the charge transport path is cutoff. In both parallel flow and counter flow settings, electrolysis performance is more sensitive to the delamination occurred at the center of the cell than those occurred at the edges of the cell.

CHAPTER 4

MICRO MODELING STUDY OF CATHODE/ELECTROLYTE INTERFACIAL STRESSES FOR SOLID OXIDE FUEL CELLS

4.1 INTRODUCTION

The basic structure of solid oxide fuel cells (SOFCs) is a positive electrode-electrolyte-negative electrode (PEN) tri-layer assembly, in which the dense electrolyte is sandwiched by porous electrodes on either side. Long-term stability is an important requirement for commercial applications of SOFC technology. However, very aggressive operating temperatures (600-1000°C) generally lead to a variety of SOFC degradations representing significant challenges in meeting lifetime requirements[112]. It is therefore essential to increase the understanding of the degradation mechanisms.

One of the important degradation phenomena in SOFCs is the occurrence of delamination at the oxygen electrode/electrolyte interface. Experimental observations have shown that such delamination failures occur in both fuel cell mode [113] and electrolysis mode [114]. Upon the occurrence of delamination, the cell performance degradation is accelerated because the interfacial open-gap, perpendicular to the main current path, consists of an insulating barrier to charge conduction, and destroys electrochemical reaction sites [115]. Such a mechanical degradation has been identified as a major limitation to the industrial developments of SOFCs [116].

Thermal stresses have been widely recognized as one of the main factors leading to the structural failure of SOFCs [50, 51]. Thermal stresses could be induced in the materials through several ways. During the cooling of the cell after being sintered at very high temperatures, stresses arise in the materials due to the mismatch in thermal expansion coefficients (TEC) between different layers of the cell [51]. Such stresses generated during cell fabrication processes are generally regarded as residual stresses. Residual stresses can also be expected if the cooling rates are not slow enough to sustain a quasi-steady heat transfer resulting in spatial temperature gradients [52]. The most widely investigated situations are thermal stresses induced by spatial temperature gradients during the fuel cell operations [50-54], particularly in transient operating conditions [55]. If the fuel supply is accidentally stopped, the nickel cermet re-oxidation may occur. This re-oxidation step generates an anodic bulk expansion which can also lead to a high level of stresses in the cell layers [117].

The mechanism governing the delamination at the oxygen electrode/electrolyte interface remains an active subject of debate. It is generally recognized that, for the stationary applications, the chemical instability at the interfaces is one of the key issues, whereas the thermo-mechanical instability is important in the transportation applications because of frequent thermal cycles [54, 68]. Other understanding envisioned that the high pressure of oxygen generated at the interface could cause the delamination as well [23].

SOFCs require materials with the ability to release or store oxygen in addition to a high concentration of oxygen vacancies for high oxygen ionic conductivity [68]. The transport of oxygen ion through oxygen vacancies may lead to the effect that the distribution of oxygen vacancy concentration is not uniform within the bulk materials,

which would cause different volumetric expansions within the materials. As a result, chemical stress occurs in oxygen ionic conducting materials. In open literature, the thermal stress effects on SOFC structures have been investigated extensively, however, the chemical stress effects are rarely studied, particularly their effects on the delamination at the cathode/electrolyte interface. When the thermal stress is coupled with the chemical stress, the structural reliability issue of SOFCs will become even more complicated. The objective of this research is to develop a micro model to study the complicated stress states at the cathode/electrolyte interface in SOFCs, including thermal stress and chemical stress. The results could be used to study the different roles of thermal stress and chemical stress at the cathode/electrolyte interface in SOFCs.

4.2 MODELING OF TRANSPORT PROCESS IN COMBINATION WITH STRUCTURAL MECHANICS

4.2.1 Solid mechanics

The total strain is the summation of the mechanical strain and two types of eigenstrains,

$$\varepsilon_{ij} = \varepsilon_{ij}^{me} + \varepsilon_{ij}^{T} + \varepsilon_{ij}^{c} \tag{4-1}$$

Here ε is the strain, the superscripts *me*, *T*, and *c* represent mechanical, thermal, and chemical respectively.

For an isotropic material, the constitutive relationship for the strain ε_{ij}^{me} and the corresponding mechanical stress is given as:

$$\varepsilon_{ij}^{me} = \frac{1}{E}\left[(1+\nu)\sigma_{ij} - \nu\sigma_{kk}\delta_{ij}\right] \tag{4-2}$$

Where σ_{ij} represents the stress components with i and j indicating the axis of the Cartesian coordinate system, E is Young's Modulus, ν is Poisson's ratio of the material, and $\delta_{ij} = \begin{cases} 1, & i = j \\ 0, & i \neq j \end{cases}$, $\sigma_{kk} = \sigma_1 + \sigma_2 + \sigma_3$. In this research, E and ν are treated as constants. The variations of the elastic constants with temperature and oxygen vacancy concentration are neglected [118].

The eigenstrain ε_{ij}^T induced by temperature variations in an isotropic material is given by:

$$\varepsilon_{ij}^T = \alpha \Delta T \delta_{ij} \tag{4-3}$$

Where ΔT is the temperature variation, and α is the thermal expansion coefficient. It is worth noting that dopants may change the formation energy of defects in materials, which in turn can affect the dependence of defect concentration on temperatures and hence the practical thermal expansion coefficient. For simplicity, the true thermal expansion coefficient is employed in this study, which is defined under the constant defect concentration of materials [62].

The chemical expansion stress induced by oxygen vacancy variations is calculated by analogy to the thermal stress. It is assumed that the volume of ionic conducting bulk materials changes linearly with volumetric oxygen ion insertion and extraction. The eigenstrain ε_{ij}^c induced by chemical expansion effect is written as [76]:

$$\varepsilon_{ij}^c = \beta \Delta c \delta_{ij} \tag{4-4}$$

Where Δc is the variation of oxygen vacancy concentration, β is the chemical expansion coefficient.

Substitution of equations (4-2)-(4-4) into equation (4-1) leads to:

$$\varepsilon_{ij} = \frac{1}{E}\left[(1+v)\sigma_{ij} - v\sigma_{kk}\delta_{ij}\right] + \alpha\Delta T\delta_{ij} + \beta\Delta c\delta_{ij} \tag{4-5}$$

The expression for stress components can be written as,

$$\sigma_{ij} = 2\mu^*\varepsilon_{ij} + (\lambda\varepsilon_{kk} - \alpha'\Delta T - \beta'\Delta c)\delta_{ij} \tag{4-6}$$

Where $\mu^* = E/2(1+v)$, $\lambda = 2v\mu^*/(1-2v)$, $\alpha' = \alpha(3\lambda + 2\mu^*)$, $\beta' = \beta(3\lambda + 2\mu^*)$,and

$\varepsilon_{kk} = \varepsilon_1 + \varepsilon_2 + \varepsilon_3$.

In elasticity, the strain tensor is related to the displacement **u** by [119]:

$$\varepsilon_{ij} = \frac{1}{2}\left(\frac{\partial u_i}{\partial x_j} + \frac{\partial u_j}{\partial x_i}\right) \tag{4-7}$$

By neglecting the body forces, the equilibrium equation is represented as,

$$\sigma_{ij,i} = 0 \ (i, j = 1, 2, 3) \tag{4-8}$$

Substituting equations (4-6), (4-7) into equation (4-8), the displacement equation can be expressed as [120],

$$\mu^*\nabla^2 u_i + (\lambda + \mu^*)u_{k,ki} - \alpha'\Delta T - \beta'\Delta c = 0, (i, k = 1, 2, 3) \tag{4-9}$$

4.2.2 Transport process in ionic conducting ceramic materials

The electrochemical potential in an ideal solid solution can be expressed as [76-78],

$$\mu_j = \mu_{0,j} + RT\ln x_j + z_j F\phi + \tau_j \tag{4-10}$$

Where μ_j is the electrochemical potential of species j; R the gas constant; T the temperature; x_j the molar fraction of species j; z_j the effective charge of species j; F the Faraday's constant; ϕ the potential; and τ_j is the stress-dependent part of the electrochemical potential. For isotropic elastic solids, the τ_j is given by[76],

$$\tau_j = -\beta_j(\sigma_{kk} + \frac{3v}{2E}(\sigma_{kk})^2 - \frac{3(1+v)}{2E}\sigma_{ij}\sigma_{ij}) \tag{4-11}$$

Where β_j is the chemical expansion coefficient of species j; σ_{ij} is the stress tensor; $\sigma_{ij}\sigma_{ij} = \sum_{i=1}^{3}\sum_{j=1}^{3}\sigma_{ij}\sigma_{ij}$.

The chemical expansion coefficient of species j is defined as,

$$\beta_j = \frac{1}{3}\frac{\partial V_m}{V_m^0 \partial c_j} \tag{4-12}$$

Where V_m is the molar volume of species j in the stress-free solid with concentration of c_j; V_m^0 is the molar volume of species j in the stress-free solid with stoichiometric defect concentration of c_j^0.

The defects are considered as species that simply diffuse through a solid with a solid framework that does not change. According to non-equilibrium thermodynamics, the molar flux of the diffusing mobile defect species j is given by,

$$N_j = -\frac{c_j D_j}{RT}\nabla\mu_j \tag{4-13}$$

Where $D_j = RTm_j$ is the diffusion coefficient of the species j; m_j is the mobility of the species j ; c_j is the concentration of diffusion component, e.g., oxygen vacancy, electron or hole.

The current density of a charged species can be represented as,

$$J_j = -\frac{z_j F c_j D_j}{RT}\nabla\mu_j \tag{4-14}$$

Substituting equation (4-10) into (4-14) gives,

$$J_j = -(z_j F D_j)\nabla c_j - \frac{c_j(z_j F D_j)}{RT}\nabla\tau_j - \frac{z_j F c_j(z_j F D_j)}{RT}\nabla\phi \tag{4-15}$$

Obviously, the current density consists of three contributors including charged species concentration gradient, stress gradient, and potential gradient.

To simplify the problem into a manageable form, we consider the case where the majority of mobile defects are vacancies and electronic species only. Because the size of electron is much smaller than that of oxygen vacancy, it is assumed that the compositional expansion is mainly caused by oxygen vacancy distribution. As a result, the effect of stress gradient on electronic current density is neglected. Also the material $Ce_{0.9}Gd_{0.1}O_{1.95-\delta}$ (GDC) is treated as a perfect electrolyte material in which the oxygen vacancy concentration is determined by the doping level only and is uniformly distributed through the entire electrolyte domain. Accordingly it is assumed that the oxygen vacancy transportation in the electrolyte is driven only by the electric field, the effects of both oxygen vacancy concentration gradient and stress gradient are neglected.

Under steady state conditions, $\nabla \cdot J_v = \nabla \cdot J_e = 0$, substituting equation (4-15), we have for the electrolyte and the cathode respectively,

$$\text{Electrolyte: } \nabla \cdot \left(-\frac{z_v F \overline{c_{v,0}} (z_v F D_v)}{RT} \nabla \phi \right) = 0 \tag{4-16}$$

Here, $\overline{c_{v,0}}$ represents the uniform oxygen vacancy concentration in the electrolyte.

$$\text{Cathode: } \begin{cases} \nabla \cdot \left(-(z_v F D_v) \nabla c_v - \frac{c_v (z_v F D_v)}{RT} \nabla \tau_v - \frac{z_v F c_v (z_v F D_v)}{RT} \nabla \phi \right) = 0 \\ \nabla \cdot \left(-(z_e F D_e) \nabla c_e - \frac{z_e F c_e (z_e F D_e)}{RT} \nabla \phi \right) = 0 \\ \sum_j z_j c_j = 0, \ (j = v, \ e, \ a) \end{cases} \tag{4-17}$$

Where v, e, and a represent vacancy, electron, and acceptor dopant respectively. The third equation in (4-17) characterizes the electroneutrality, requiring that the sum of

all the charges in a material be equal to zero at macroscopic scale. The assumption of an electroneutrality does not necessarily preclude the existence of a nonlinear potential distribution as indicated by Newman [121].

4.3 MODEL SETUP AND BOUNDARY CONDITIONS

Figure 4.1(a) shows the computational domain of the model, where a cathode particle is attached to a bulk electrolyte due to the sintering effect. It is assumed that the cathode particle is a mixed ionic and electronic conducting material, e.g., $La_{0.6}Sr_{0.4}Co_{0.2}Fe_{0.8}O_{3-\delta}$ (LSCF), while the electrolyte is an ionic conducting material, e.g., $Ce_{0.9}Gd_{0.1}O_{1.95-\delta}$ (GDC). Since the considered computational domain is relatively small, the isothermal condition is assumed. Essentially equations (4-9), (4-16) and (4-17) need to be solved to obtain the unknowns of defect concentration c_j, potential ϕ, and solid displacements $\mathbf{u}$ as well as their derivatives. Accordingly the boundary conditions are specified including defect concentration, potential and displacement, which are detailed as follows.
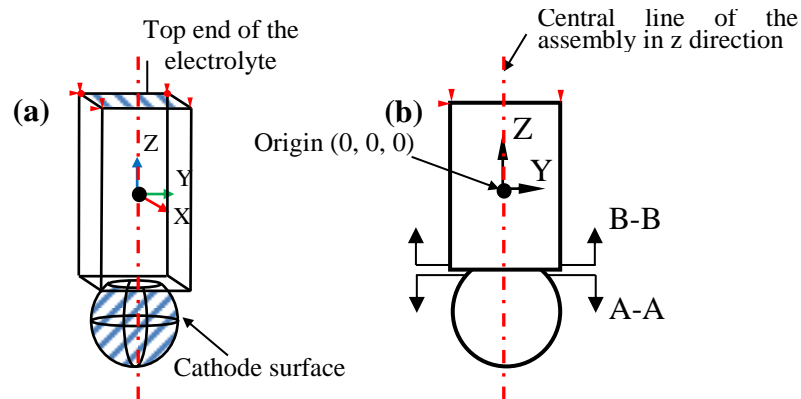
Figure 4.1 (a) Cathode/electrolyte assembly (the origin of XYZ coordinate system is located at the central point of the electrolyte domain); (b) schematic illustration of cross-section locations (The A-A and B-B cross sections are parallel to the cathode/electrolyte interface and have the distance of 0.5μm from the cathode/electrolyte interface)

50

4.3.1 Concentration boundary conditions

The defect concentration of conducting materials is dependent on the doping level. The defect concentration also depends on the oxygen partial pressures, particularly those of bulk material surface exposed to the surrounding atmosphere, such as the cathode material $La_{0.6}Sr_{0.4}Co_{0.2}Fe_{0.8}O_{3-\delta}$ (LSCF). For perovskite-type oxides in a low oxygen partial pressure P_{O_2} and small temperature ranges, the oxygen nonstoichiometry δ shows linear dependence on log P_{O_2} [122, 123],

$$\delta = A + B\log_{10} P_{O_2} \tag{4-18}$$

Where A and B are constants, depending on specific type of perovskite oxides. For $La_{0.6}Sr_{0.4}Co_{0.2}Fe_{0.8}O_{3-\delta}$ (LSCF) cathode material, A and B are obtained by fitting the experimental data [124],

$$\delta = -0.02 - 0.03\log_{10}(P_{O_2} / bar) \tag{4-19}$$

Equation (4-19) is valid for oxygen partial pressures from 10^{-2} bar to 10^{-8} bar and temperature at 973.15K. It should be pointed out that for a working cathode the gas phase and the surface of the cathode particle are generally not in equilibrium [125, 126]. For simplicity of the model, the gas phase and the surface of the cathode particle are assumed to be in equilibrium and the equation (4-19) is applicable.

4.3.2 Other boundary conditions

The potential difference between the top end of the electrolyte (Figure 4.1(a)) and the cathode particle surface is determined by using the multi-physics modeling approach, which is approximately greater than or equal to -0.4V as predicted by the SOFC model [115]. The electrolyte/cathode assembly is point-constrained at the top end of the electrolyte as shown in Figure 4.1(a) while traction-free conditions are applied on the rest

of surfaces. This prevents rigid-body movements but does not affect the stress distribution. The boundary conditions are summarized in Table 4.1.

Table 4.1 Boundary conditions

Boundary	Oxygen vacancy concentration	Potential	Mechanics
Anode/electrolyte interface	--	0V	Point constrained
Cathode/electrolyte interface	Specified by the doping level in electrolyte	--	Continuum
Cathode particle surface	Specified by oxygen partial pressure	ϕ_c	Free
Other surfaces	Symmetry/Insulation, $\nabla \cdot J_v = 0$	Symmetry/Insulation $\nabla \cdot J_e = 0$	Free

4.4 SIMULATIONS AND MODEL PARAMETERS

The mathematical model is solved using finite element package, COMSOL Multiphysics V4.0. The model parameters are listed in Table 4.2.

Since the related experimental data are very limited, the parameters noted with * are estimated based on the data from open literatures. In particular, the oxygen vacancy concentrations (c_v) induced by the dopant in the electrolyte and cathode materials are estimated according to their chemical formula. As mentioned above, the $Ce_{0.9}Gd_{0.1}O_{1.95-\delta}$ (GDC) electrolyte is treated as a perfect electrolyte, in which the oxygen vacancy concentration is uniformly distributed and determined by the dopant only. For stoichiometric defect reactions, we have $\delta = 0$. Using the molar volume of GDC bulk electrolyte in Table 2, we can obtain $\overline{c_{v,0}} = 0.05/V_{m,GDC} = 2083$ (mol/m^3). This value is used as the concentration boundary condition of the cathode/electrolyte interface. For the $La_{0.6}Sr_{0.4}Co_{0.2}Fe_{0.8}O_{3-\delta}$(LSCF) cathode particle, if choosing $\delta = 0.06$, we can obtain $c_{v,LSCF} = 0.06/V_{m,LSCF} = 1818$ (mol/m^3). For the calculation of chemical expansion

52

coefficient, the ratio of strain vs. oxygen nonstoichiometry is obtained from open literatures for GDC[74] and LSCF[63] respectively. The chemical expansion coefficient is then obtained by using the equation $\beta=\varepsilon/(\delta/V_m)$.

Table 4.2 Parameters used in the model

Item Name	Cathode (LSCF)	Electrolyte (GDC)	Reference
Dimensions of computational domain (m)	Particle radius: 5×10^{-6}	$Width\times Height\times Length$ $10^{-5}\times10^{-5}\times(2\times10^{-5})$	
E (GPa)	161	255.9	[51]
ν	0.32	0.334	[51]
Uniaxial tensile strength, σ_f, (MPa)	180	250	[50, 127-129]
ρ (kg/m^3)	6820	7150	[51]
T (K)	973.15	973.15	
V_m (m^3/mol)	33×10^{-6}	24×10^{-6}	[63, 74]
Reference oxygen vacancy concentration, (m^3/mol)	1818	--	∗
Mobility $(mol\cdot m^2 / J\cdot s)$	m_v: 2.0×10^{-14} m_e: 7.26×10^{-13}	m_v: 3.4×10^{-14}	[130]∗
β (m^3/mol)	4.95×10^{-6}	--	[63]∗
$\alpha\,(\dfrac{\mu m}{m}\dfrac{1}{K})$	15	11	[51]

4.5 RESULTS AND DISCUSSION

The thermal and chemical stresses are coupled together in a complicated way in practical SOFCs. It is difficult for experimental methods to identify their individual contributions. In this aspect, modeling technique has the flexibility to study the individual roles. In the following sections, the chemical stress and thermal stress are individually studied, followed by the combinational investigations.

4.5.1 Chemical stress
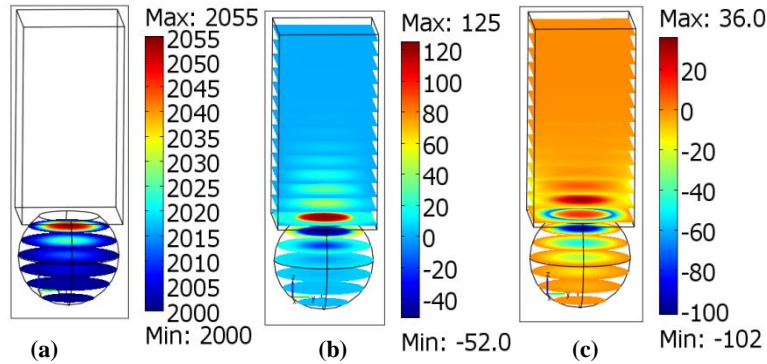
Figure 4.2 Oxygen vacancy concentration distribution (mol/m^3) (a); first principal stress distribution (MPa) (b); third principal stress distribution (MPa) (c).

Figure 4.2(a) shows the oxygen vacancy concentration distribution within the considered electrolyte/cathode assembly. The oxygen vacancy concentration reaches the maximum value of 2055 mol/m^3 near the cathode/electrolyte interface and decreases toward the cathode particle surface. Within the electrolyte, the oxygen vacancy concentration is uniform because the perfect electrolyte is assumed and oxygen ion transport is driven only by the electrical potential. Even though oxygen ions are generated on the cathode particle surface while being consumed at the top end of electrolyte surface in the model, the distribution of the oxygen ion concentration shows certain gradients, particularly near the cathode/electrolyte interface. This leads to the chemical stress in the cathode/electrolyte assembly.

The corresponding first principal stress and third principal stress profiles are shown in Figure 4.2(b) and Figure 4.2(c) respectively. Obviously the maximum first principal stress of 125MPa occurs in the electrolyte near the cathode/electrolyte interface (Figure 4.2(b)). The maximum third principal stress of -102MPa is in the cathode adjacent to the cathode/electrolyte interface (Figure 4.2(c)). Since the oxygen vacancy

concentration in the cathode particle is greater than that in the cathode particle with stress-free condition ($1818mol/m^3$), the cathode particle tends to expand while the electrolyte is reluctant to expand. As a result, the cathode particle is in compressive state near the cathode/electrolyte interface while the electrolyte is in tensile state. The complicated stress distribution is resulted from the combinational effects of oxygen vacancy concentration distributions and the structural configuration of the cathode/electrolyte assembly.

To examine the complicated chemical stress state across the cathode/electrolyte interface, the details of stress distributions in A-A and B-B cross sections (A-A and B-B are defined in Figure 4.1(b)) are obtained as shown in Figure 4.3. Figures 4.3(a)-(c) and 4.3(c') show the stress distributions in cross-section B-B while Figures 4.3(d)-(f) and 4.3(f') show those in cross-section A-A. As can be seen from Figure 4.3(a), the shear stress distribution shows four small "islands" with relatively high stress magnitude. The positive shear stress and negative shear stress occur alternatively along the neck of the interface. According to the coordinate system defined in Figure 4.1(a), the shear stress directions are represented with arrows in Figure 4.3(a) and 4.3(d). The normal stress in B-B cross section shows the ring-shaped distribution (Figure 4.3(b)). Obviously the normal stress shows tensile state within a small internal circle followed by a ring band area with stress magnitude close to zero. Beyond this area, another ring band area with maximum compressive stress can be clearly seen. The normal stress then ripples off to zero towards the circumference. This phenomenon can be attributed to the non-uniform distribution of oxygen vacancy concentration in the cathode particle, where the vacancy concentration decreases from the center towards the circumference of the particle (as

shown in Figure 4.2(a)). The volumetric expansions in different locations of the cathode particle will be different due to non-uniform vacancy concentrations in the cathode particle. Meanwhile the volumetric expansion of cathode particle is confined by the electrolyte at the cathode/electrolyte interface. Therefore the stress is generated as shown in Figure 4.3(a) and 4.3(b).

The first and third principal stresses in the B-B cross-section in the electrolyte are shown in Figures 4.3(c) and 4.3(c') respectively. The first principal stress in Figure 4.3(c) shows the maximum value of 118MPa in the central circle area and ripples to zero towards the circumference. Obviously the maximum first principal stress of 118MPa is less than the uniaxial tensile strength 250MPa of the GDC electrolyte (Table 4.2). The third principal stress in Figure 4.3(c') shows tensile state within the central circle area followed by the maximum compressive stress of -67MPa in a ring band. The third principal stress then decreases to a relative low compressive stress state towards the circumference. For ceramic materials, the compressive strength is usually greater than the tensile strength. Due to the lack of experimental data, here we assume that the compressive strength is equal to the tensile strength for the GDC electrolyte. Accordingly the maximum third principal stress of -67MPa is less than the compressive strength of -250MPa. Combining the first and third principal stresses in B-B cross-section with the GDC electrolyte strength, one can see that the chemical stress will not lead to the fracture of the electrolyte.

Figure 4.3 Chemical stress distribution (MPa). Stress at B-B cross section: (a) shear stress, (b) normal stress, (c) first principal stress, (c') third principal stress; stress at A-A cross section: (d) shear stress, (e) normal stress, (f) first principal stress; (f') third principal stress.

The various stress distributions in A-A cross section in the cathode particle are shown in Figure 4.3(d)-(f) and 4.3(f'), which display opposite distribution patterns to those in B-B cross section. These results can be attributed to the balance requirement of stresses in the cathode/electrolyte assembly. The maximum first principal stress takes place in the shell area of the cathode particle and reaches 115MPa as shown in Figure 4.3(f). The maximum third principal stress occurs in the central circle area and reaches -154MPa as shown in Figure 4.3(f'). Obviously it is in compressive stress state. Here we

assume that the compressive strength of LSCF material is the same as its tensile strength (180MPa) due to the lack of experimental data. One can see that neither the first principal stress nor the third principal stress can lead to the fracture of the cathode particle.

4.5.2 Thermal stress

Since the computational domain is relatively small, the temperature distribution is assumed to be uniform within the domain. Accordingly the thermal stress is calculated by varying the temperature from one state to another. Because the LSCF cathode is generally sintered at 900-1000°C[131], the stress-free temperature is assumed at 1000°C. The thermal stress is then calculated when the cathode/electrolyte assembly is operated at 700 °C. Figures 4.4(a) and 4.4(b) show the corresponding first and third principal stress distributions respectively. Clearly the maximum stress occurs at the cathode/electrolyte interface with significant non-uniformity. Since the assumed operating temperature (700°C) is different from the thermal stress-free temperature (1000°C), and thermal expansion coefficient of GDC electrolyte is different from that of LSCF cathode, the expansion of the GDC electrolyte should be different from that of the LSCF cathode. However, without delamination, the expansion of both electrolyte and cathode should be identical at the cathode/electrolyte interface. This confliction of structural deformation leads to the thermal stress as shown in Figure 4.4.
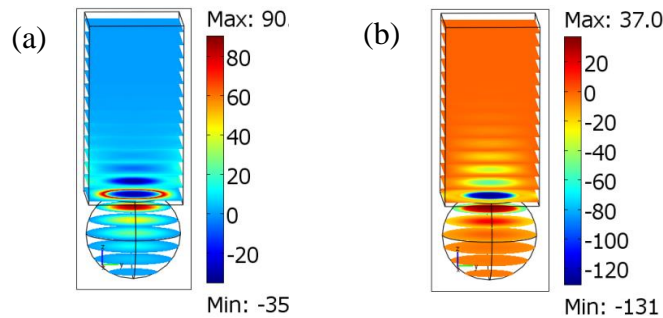
Figure 4.4 Distribution of principal stresses (MPa):
(a) first principal stress; (b) third principal stress.
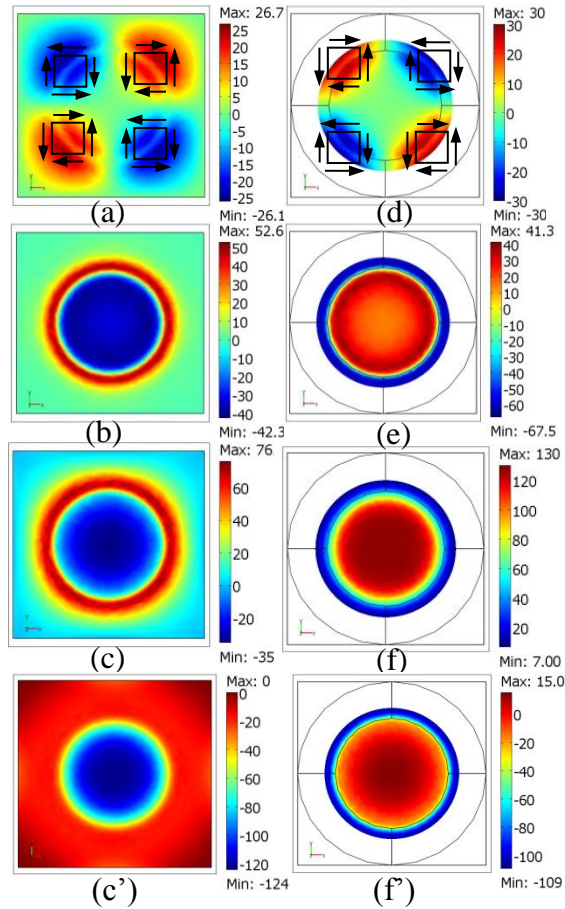
Figure 4.5 Thermal stress distribution (MPa). Stress at B-B cross section: (a) shear stress, (b) normal stress, (c) first principal stress, (c') third principal stress; stress at A-A cross section: (d) shear stress, (e) normal stress, (f) first principal stress; (f') third principal stress.

To examine the details of thermal stress near the cathode/electrolyte interface and identify the difference from their chemical stress counterparts, the distribution of stress components is individually obtained at the cross sections A-A and B-B respectively. The shear stress distribution in B-B cross section shows four small "islands" (Figure 4.5(a)), where the positive and negative shear stress "islands" appear alternatively. Comparing the chemical stress distribution in the same cross section B-B (Figure 4.3(a)), one can see that the pattern of thermal stress distribution in Figure 4.5(a) is opposite to that of chemical stress distribution. The difference of stress distribution is due to the different

natures of chemical expansion and thermal expansion, where the chemical expansion is the tendency of materials to change in volume due to the variations of oxygen vacancy concentration; whereas the thermal expansion is the tendency of materials to change their volumes in response to the change in temperatures. The normal stress in B-B cross section shows a ring-band distribution (Figure 4.5(b)). Within a central circle, the normal stress is compressive. Beyond this central circle area, a ring band with normal stress amplitude close to zero can be observed, followed by another ring-band like area, in which the normal stress is tensile. The stress then decays to zero towards the circumference.

The first and third principal stress distribution in B-B cross section is shown in Figure 4.5(c) and 4.5(c') respectively. The first principal stress in Figure 4.5(c) is in compressive state in the central circle area. Beyond this circle area, a ring-band area appears with the maximum tensile stress of 76MPa. The first principal stress then decays to 0 MPa towards the circumference. The third principal stress in Figure 4.5(c') shows the maximum compressive stress of -124MPa within the central circle area. Beyond this circle, the third principal stress decays to 0 MPa. Since both the maximum first principal stress and the maximum third principal stress are less than the strength of the GDC electrolyte, the thermal stress cannot cause the failure of the GDC electrolyte.

The various thermal stress distributions in A-A cross section in the cathode particle are shown in Figure 4.5(d)-(f) and 4.5(f'), which display opposite distribution patterns to those in B-B cross section. These results may be attributed to the balance requirement of stresses in the cathode/electrolyte assembly due to the mismatch of thermal expansion coefficients between the electrolyte and the cathode. The maximum

60

first principal stress takes place within the central circle area and reaches 130MPa as shown in Figure 4.5(f). The maximum third principal stress occurs in the shell area of the cathode particle circumference and reaches -109MPa as shown in Figure 4.5(f'). Obviously it is in compressive stress state. Since the tensile/compressive strength of the LSCF cathode is 180MPa (Table 4.2), we can see that neither the first principal stress nor the third principal stress can lead to the fracture of the cathode particle.

4.5.3 Combined chemical and thermal stresses at the cathode/electrolyte interface

In practical solid oxide fuel cells, the chemical stress and thermal stress occur simultaneously. In this section, the cathode/electrolyte interfacial stresses induced by the combined chemical and thermal effects are studied. The operating conditions are the combination of those in section 4.5.1 and 4.5.2. Comparing every single chemical stress distribution in Figure 4.3 with the corresponding thermal stress distribution in Figure 4.5, one may find that the patterns of chemical stress distribution are opposite to those of thermal stress distribution. Therefore the chemical stress will be partially canceled out by the thermal stress, or vise verse, when combined together. This understanding can be seen from Figure 4.6, where the magnitude of every single combinational stress is less than that of chemical stress (Figure 4.3) and thermal stress (Figure 4.5). So the combination of chemical and thermal stress facilitates to mitigate the overall stress occurred at the cathode/electrolyte interface. In B-B cross section, the maximum first principal stress is the tensile stress of 20MPa (Figure 4.6(c)) and the maximum third principal stress is the compressive stress of -20MPa (Figure 4.6(c')), both of which are less than the strength of the GDC electrolyte (Table 4.2). Therefore no fracture occurs in the electrolyte in this case. Similarly, in A-A cross section, the maximum first principal stress is the tensile

stress of 31MPa (Figure 4.6(f)) and the maximum third principal stress is the compressive stress of -19MPa (Figure 4.6(f')), both of which are less than the strength of the LSCF cathode (Table 4.2). Therefore no fracture occurs in the cathode particle either.
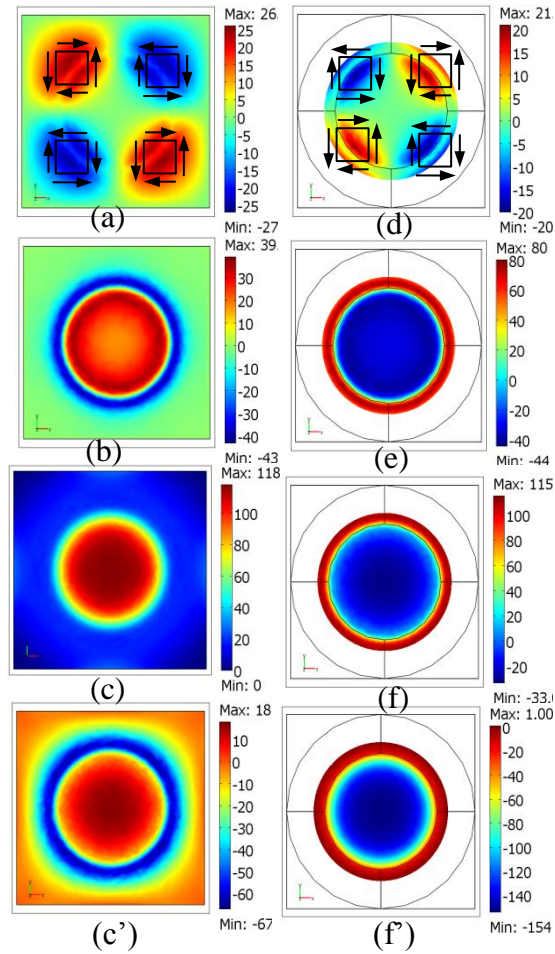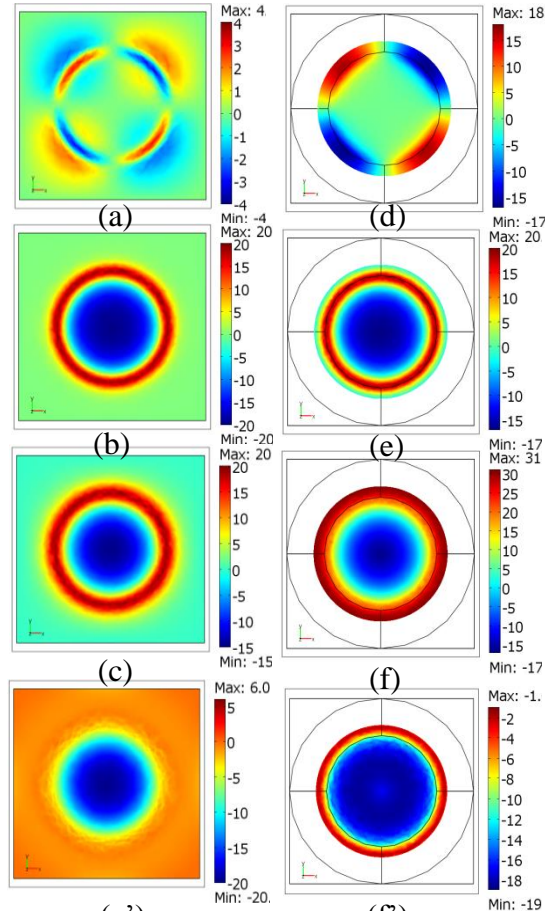

Figure 4.6 Combined thermal and chemical stress (MPa). In B-B cross section: (a) shear stress, (b) normal stress, (c) first principal stress, (c') third principal stress; In A-A cross section: (d) shear stress, (e) normal stress, (f) first principal stress; (f') third principal stress.

4.5.4 Effects of non-uniform oxygen partial pressure

Oxygen partial pressure may significantly affect the surface oxygen vacancy concentration of cathode material and oxygen reduction reaction process. At the cathode side of SOFCs, the oxygen diffuses from the channel to the surface of cathode material through porous electrode. As a result, non-uniform oxygen partial pressure distribution

may exist within porous cathode. It is anticipated that the non-uniform distribution of oxygen partial pressure could cause complicated chemical stress and ceramic particle distortions. To study such effects, we assume that different portion of cathode particle surface (shown in Figure 4.7) is subjected to different oxygen partial pressures. Specifically, the oxygen partial pressure of 0.002 bar is applied to the right half surface of the cathode particle, while that of 0.00112 bar is applied to the left half surface of the cathode particle (Figure 4.7). The rest of the operating conditions are the same as those in section 4.5.1. Because of non-uniform oxygen partial pressure on the cathode particle, the corresponding distribution of oxygen vacancy concentration within the A-A cross section is also non-uniform (Figure 4.7). Specifically, the right half surface of the cathode particle is exposed to the environment with high oxygen partial pressure; consequently the concentration of oxygen vacancy is low. This can be seen from the shell area of the right half surface of the cathode particle in Figure 4.7. By contrast, the left half surface of the cathode particle is exposed to the low oxygen partial pressure; as a result, the corresponding concentration of oxygen vacancy is high, because the gas phase and the surface of the cathode particle are in equilibrium. One may also see from Figure 4.7 that the oxygen vacancy concentration within the central circle area is high, which is significantly affected by low oxygen partial pressure instead of high oxygen partial pressure.

The higher oxygen vacancy concentration leads to larger expansions in volume, therefore, the non-uniform distribution of oxygen vacancy concentration is expected to cause the complicated chemical stress distribution. Figure 4.8(a) shows the first principal stress in A-A cross section, which shows significant variations along the circumferential

63

shell area of the cathode particle. The first principal stress in Figure 4.8(a) varies from -48MPa to 207MPa, which exceeds the fracture strength of the LSCF cathode material 180MPa. As a result, cracks within the cathode particle might initiate in this case. It is worth noting that the assumption of abrupt changes of oxygen partial pressure on the cathode particle surface might be an extreme scenario, however, the results clearly demonstrate the significant effects of oxygen partial pressure on chemical stress generation. The third principal stress in Figure 4.8(c) is dominated by the compressive stress within the central area of A-A cross section.
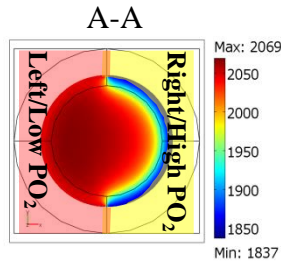
Figure 4.7 Oxygen vacancy concentration distribution at A-A cross section
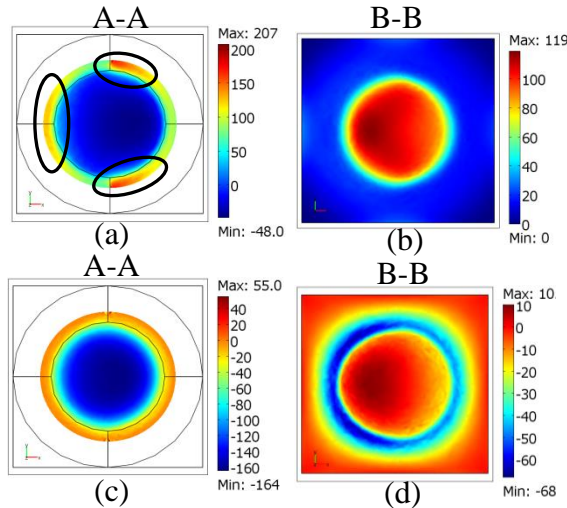
Figure 4.8 principal stress distributions (MPa) under non-uniform oxygen partial pressure. (a) first principal stress at A-A cross section, (b) first principal stress at B-B cross section; (c) third principal stress at A-A cross section, (d) third principal stress at B-B cross section.

As shown in Figure 4.7, the distribution of the oxygen vacancy concentration is significantly non-uniform. It has been realized that different vacancy concentrations lead to different volumetric expansions in the material. On the other hands, such volumetric expansions are also confined by the structure configuration of the cathode/electrolyte assembly. Therefore complicated stress takes place. The first and third principal stresses in B-B cross section are shown in Figure 4.8(b) and 4.8(d) respectively. The maximum tensile stress is 119MPa while the maximum compressive stress is -68MPa. None of these stresses can lead to the cracks within the GDC electrolyte (strength 250MPa). Comparing to Figures 4.3(c), 4.3(c'), 4.3(f) and 4.3(f'), one can see that the stress distributions in Figure 4.8(a-d) show different degree of distortion because of non-uniform oxygen partial pressure distribution on the cathode particle surface.

4.5.5 Effects of oxygen vacancy concentration at the cathode particle surface

For practical solid oxide fuel cells, the cathode is exposed to the environment containing oxygen gas. The oxygen gas in turn affects the surface oxygen vacancy concentration of the cathode particle, which will further influence the oxygen vacancy concentration distribution in the cathode/electrolyte assembly. Figure 4.9(a) shows the distribution of oxygen vacancy concentration. The horizontal axis in Figure 4.9 is defined from the cathode surface towards the cathode/electrolyte interface along the central line of the cathode/electrolyte assembly in z-direction (the z-direction is defined in Figure 4.1(a)). The dimension from $-19\mu m$ to $-10\mu m$ on the horizontal axis is the cathode domain while that from $-10\mu m$ to $10\mu m$ is the electrolyte domain. As shown in Figure 4.9(a), the oxygen vacancy concentration increases from the cathode particle surface to the cathode/electrolyte interface. The gradient of the oxygen vacancy concentration is

relatively large near the cathode/electrolyte interface. When the oxygen vacancy concentration increases from 1800mol/m^3 to 2000mol/m^3 at the cathode surface, the overall distribution of oxygen vacancy concentration also increases.
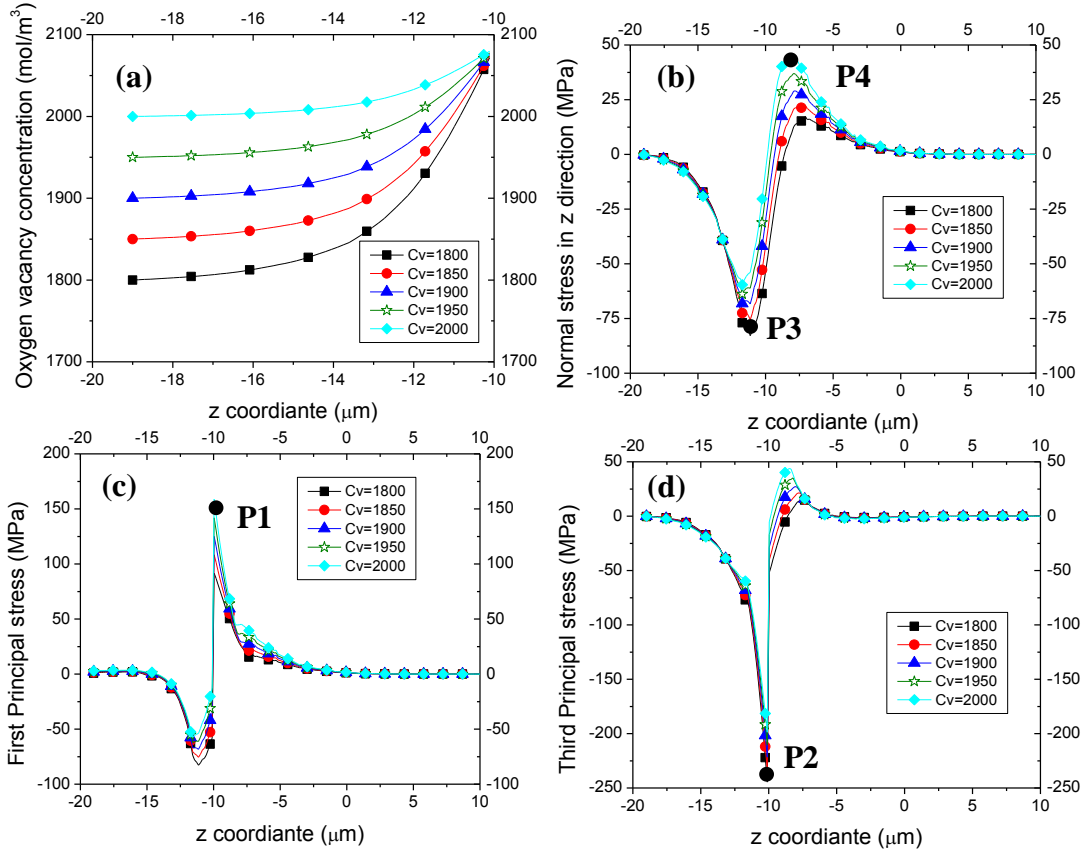
Figure 4.9 Parameter distribution along the central line of the cathode/electrolyte assembly in z-direction under different oxygen partial pressure: (a) oxygen vacancy concentration, (mol/m^3); (b) normal stress in z direction, (MPa); (c) first principal stress, (MPa). (d) third principal stress, (MPa).

The corresponding distributions of the normal stress, the first principal stress, and the third principal stress are shown in Figure 4.9(b), 4.9(c), and 4.9(d) respectively. Obviously the maximum stress and the maximum stress gradient take place near the cathode/electrolyte interface, where the compressive stress occurs at the cathode side while the tensile stress happens at the electrolyte side. Since the oxygen vacancy concentration reaches the maximum value at the cathode/electrolyte interface and

decreases towards the cathode particle surface (as shown in Figure 4.9(a)), the volumetric expansion of cathode near the cathode/electrolyte interface is larger than that of the rest part in the cathode. Considering that the cathode expansion near the cathode/electrolyte interface is confined by the electrolyte, this is the reason that the compressive stress occurs at the cathode side while the tensile stress takes place at the electrolyte side.
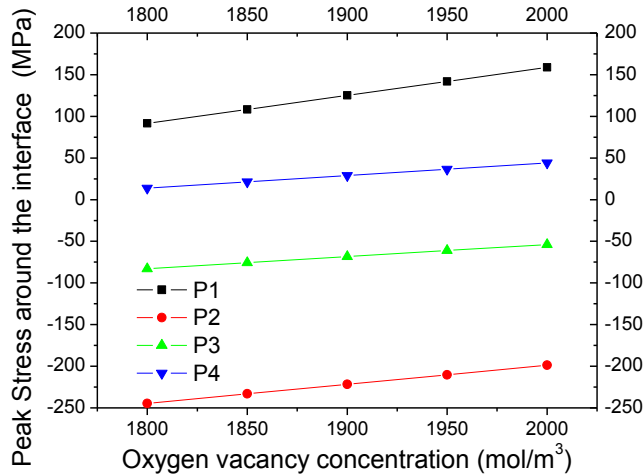
Figure 4.10 Peak stress at the specified locations in Figure 4.9, (MPa).

To correlate the boundary conditions on the cathode surface with the maximum stresses occurred at the cathode/electrolyte interface, four peak stresses marked as P1, P2, P3, and P4 in Figure 4.9(c), 4.9(d), and 4.9(b) respectively are selected. Figure 4.10 shows the correlations between P1, P2, P3, P4 and the oxygen vacancy concentrations on the cathode particle surface. P1 and P4 are in tensile state while P2 and P3 are in compressive state. Clearly, increasing the oxygen vacancy concentration on the cathode particle surface will increase the tensile stresses of P1 and P4 but decrease the compressive stresses of P2 and P3. Conversely, decreasing the oxygen vacancy concentration on the cathode particle surface is beneficial to reduce the tensile stresses of P1 and P4 but increase the compressive stresses of P2 and P3. Therefore, suitable oxygen vacancy concentration on the cathode particle surface needs to be considered so that the

first and third principal stresses can be confined below the strength of the concerned materials if appropriate.

4.6 CONCLUSION

A micro model is developed to study the cathode/electrolyte interfacial stresses. The model considers the complicated interactions between structural mechanics and ionic transport process through conductive defects. While both the chemical and thermal stresses are complicated at the interface, the chemical stresses show different distribution patterns from the thermal stresses. The results of combined thermal and chemical stresses show that these two kinds of stresses can be partially canceled out with each other, leading to the reduced overall stresses at the cathode/electrolyte interface. The distributions of oxygen partial pressure and thus the oxygen vacancy concentration on the cathode particle surface have significant effects on chemical stress distribution and consequently on the principal stresses at the cathode/electrolyte interface.

CHAPTER 5

MODELING OF CHEMICAL-MECHANICAL COUPLINGS IN ANODE-SUPPORTED

SOLID OXIDE FUEL CELLS AND RELIABILITY ANALYSIS

5.1 INTRODUCTION

Solid oxide fuel cell (SOFC) has been well demonstrated as a promising clean energy conversion technology that converts the chemical energy of fuels into electricity directly[132]. To commercially utilize this technology, the SOFC material system should have not only very good electrochemical performance for high energy conversion efficiency but also long term stability. It is well known that the SOFCs are operated under very aggressive conditions, e.g., high temperatures (600-800°C) and extremely low oxygen partial pressures (anode electrode). These operating conditions could lead to a variety of degradations, which impose great challenges on meeting the lifetime requirement of SOFCs. There have been significant efforts toward the investigations of SOFC degradation mechanisms, including interface stability [27], redox stability [39, 40, 43], material phase stability under different temperatures and gas environment [133, 134], microstructure/micro-morphology stability [48, 49], and mechanical stability [53-55, 135, 136]. Among these degradation mechanisms, the mechanical instability is a major degradation mechanism limiting the industrial development of SOFCs [137, 138].

The basic structure of SOFCs is the positive-electrode/electrolyte/negative-electrode (PEN) tri-layer assembly. Because the materials are different from one layer to

another, the thermal stress occurs at elevated temperatures due to thermal expansion mismatch. In open literature, the thermal stress issues in SOFCs have been studied extensively using modeling approach. Kim et al. studied thermal stress of functionally graded SOFCs with assumed temperature distributions [64]. Liu et al. investigated the thermal stress at electrode/electrolyte interface, upon which lifetime of SOFCs was predicted under assumed thermal cycling conditions [54]. Since the thermal stress is dependent on the temperature distribution across SOFC structure, the multi-physics electrochemical model is usually needed to determine the temperature distribution, upon which thermal stress is calculated. Clague et al. analyzed thermal stress of anode-supported SOFC under duty cycles using the temperature distribution predicted by computational fluid dynamics model [65]. Peksen et al. performed the transient thermal-mechanical analysis for an SOFC short stack using the similar approach [66]. Khaleel et al. carried out stack thermal stress analysis using the temperature profile calculated from the coupled electrochemistry, thermal and flow analysis [67]. All of these represent significant progress toward thermal stress analysis of SOFC structures.

The materials of SOFCs have the capability to take and/or release oxygen depending on the equilibrium state between the bulk ceramics and the surrounding atmosphere, which in turn leads to the volumetric change of bulk ceramics, termed chemical expansion. In this respect, extensive experiments have been carried out to elucidate the relations between oxygen deficit in ceramics and surrounding oxygen partial pressure and temperature as well as chemical expansion, such as Adler et al. [62] and Wachsman group [118, 139]. These studies only considered chemical expansion of bulk ceramics under non-stoichiometric conditions. The materials of SOFCs also have the

ability to transport oxygen ions through vacancy defects. The complicated multi-physicochemical processes in SOFCs could lead to the fact that the distribution of oxygen vacancy concentration is not uniform within the bulk materials of electrolyte and electrodes. The non-uniform oxygen vacancy concentration distribution would cause different volumetric expansions in different locations within bulk materials, resulting in a complicated chemical-mechanical coupling phenomenon and chemical stress. Compared to the study of thermal stress in SOFCs, the chemical stress study is still at very early stages. Atkinson studied the chemically-induced stresses in gadolinium doped ceria (GDC) electrolyte through measuring the deformation of electrolyte [74]. Krishnamurohy and Sheldon developed a model to study the chemical stress occurred in the 1-D electrolyte of GDC subjected to oxygen potential gradient [75]. Swaminathan at al. developed a model framework to study the chemical stress of a GDC planar electrolyte with different oxygen partial pressures on both sides [77, 78]. Yakabe et al. modeled the chemical stress in a plate of doped lanthanum chromite with either surface of the plate exposed to the fuel and air respectively [73]. Terada et al. developed a 1-D model to study electro-chemical-mechanical coupling behavior of PEN structure without considering complicated multi-physics transport processes in SOFCs [79].We recently developed a micro-model to study the chemical and thermal stresses at cathode/electrolyte interface [140]. These results represent significant progresses toward the understanding of chemical-mechanical coupling phenomenon in a component of SOFCs. However, practical SOFCs involve very complicated multi-physicochemical processes particularly in porous electrodes. This could generate complicated oxygen potential gradients and electrical field. In addition, the individual component is mechanically constrained by PEN structure

71

assembly in SOFCs. Accordingly the chemical stress in an SOFC setting would be very complicated and the corresponding chemical-mechanical coupling is not well understood.

The objective of this research is to develop an innovative model to study chemical-mechanical coupling phenomenon in an SOFC. The model considers the chemical stress in PEN structure of a button cell induced by complicated multi-physicochemical processes. Based upon chemical stress calculation, the reliability of PEN structure is evaluated and correlated to different operating conditions and design parameters as well as mechanical constraints. To our best knowledge, this is the first model of chemical-mechanical coupling under multi-physicochemical processes at a cell level and is an important module complementary to the state-of-the-art electrochemical-thermal-mechanical modeling for SOFCs.

5.2 DESCRIPTION OF MATHEMATICAL MODEL

SOFCs involve very complicated multi-physicochemical processes, such as reactant/product gas diffusion in porous electrodes, electrical oxidation of fuel in the anode, oxygen reduction reaction in the cathode, oxygen exchange at electrode surface, and ion transport through oxygen vacancies in solid matrix of PEN structure, as well as ionic transport induced chemical expansion of PEN structure. In the following sections, the corresponding mathematical equations will be described in details.

5.2.1 Charge transport process in conducting ceramic solid phases

The driving force for charge transport in a solid solution is the gradient of electrochemical potential. The electrochemical potential of a defect species in an ideal solid solution is represented by [76-78],

$$\mu_j = \mu_{0,j} + RT ln x_j + z_j F \phi + \tau_j \tag{5-1}$$

where μ_j is the electronic potential of species j; R the gas constant; T the temperature; x_j the molar fraction of species j; z_j the effective charge of species j; F the Faraday's constant; ϕ the electrical field due to externally applied potential and/or non-uniform distribution of charged species; and τ_j is the stress-dependent part of the electrochemical potential. For isotropic elastic solids, the τ_j is given by [76],

$$\tau_j = -\beta_j \left(\sigma_{kk} + \frac{3v}{2E} (\sigma_{kk})^2 - \frac{3(1+v)}{2E} \sigma_{ij} \sigma_{ij} \right) \tag{5-2}$$

where β_j is the chemical expansion coefficient due to species j; σ_{ij} is the stress tensor; $\sigma_{ij}\sigma_{ij} = \sum_{i=1}^{3}\sum_{j=1}^{3} \sigma_{ij}\sigma_{ij}$.

The chemical expansion coefficient due to species j is defined as [118],

$$\beta_j = \frac{1}{3} \frac{1}{V_m^0} \frac{\partial V_m}{\partial c_j} \tag{5-3}$$

where V_m is the molar volume of species j in the stress-free solid with concentration of c_j; V_m^0 is the molar volume of species j in the stress-free solid with stoichiometric defect concentration of c_j^0.

According to non-equilibrium thermodynamics, the current density of a charged species in a solid solution driven by an electrochemical potential can be expressed as [77],

$$J_j = -\frac{z_j F c_j D_j}{RT} \nabla \mu_j \tag{5-4}$$

where $D_j = RT m_j$ is the diffusion coefficient of species j; m_j is the mobility of species j; c_j is the concentration of diffusion component, e.g., oxygen vacancy, electron, or hole.

Substitution of equation (5-1) into (5-4) gives,

$$J_j = -\left(z_j F D_j \right) \nabla c_j - \frac{c_j (z_j F D_j)}{RT} \nabla \tau_j - \frac{z_j F c_j (z_j F D_j)}{RT} \nabla \phi \tag{5-5}$$

Clearly, the diffusion of mobile defects in a solid solution is driven by the gradients of mobile species concentration and stress as well as electrical field.

Under steady state conditions, $\nabla \cdot J_j = Q_j$, substituting equation (5-5), we have,

$$\nabla \cdot (-(z_j F D_j)\nabla c_j - \frac{c_j(z_j F D_j)}{RT}\nabla \tau_j - \frac{z_j F c_j(z_j F D_j)}{RT}\nabla \emptyset) = Q_j \qquad (5\text{-}6)$$

Where Q_j is the source term of species j.

The equation (5-6) is applied for the transport of both oxygen vacancy and electron or hole. Since electron or hole is much smaller than oxygen vacancy, the flux of electron or hole induced by stress gradient is generally neglected. Accordingly the second term in the left side of equation (5-6) is neglected for electron or hole transport process. One essential requirement is that the charge neutrality should be maintained for bulk solid solution, i.e.,

$$\sum_j z_j c_j = 0 \qquad (5\text{-}7)$$

The equations of (5-6) and (5-7) are used to describe the transport process of charged species in a solid solution.

5.2.2 Surface electrochemical reactions

The electrochemical reactions in the electrodes are strongly dependent on the electrode materials. Without loss of generality, we assume that the cathode material is a mixed ionic and electronic conducting (MIEC) ceramics while the anode material is the composite of nickel and electrolyte material.

5.2.2.1 Electrochemical reactions in MIEC cathode

With MIEC ceramic as the cathode material, the active sites for oxygen reduction reaction are extended to the entire MIEC/gas interface. The oxygen molecule first is adsorbed onto the material surface. The adsorbed oxygen then is incorporated into an

oxygen vacancy in MIEC material matrix. Using the Kroger-Vink notation, these two steps can be represented as,

$$\frac{1}{2}O_2 + s \rightarrow O'_{ads} + h^{\cdot} \tag{5-8}$$

$$O'_{ads} + V_{\ddot{O}} \rightarrow O_O^x + h^{\cdot} + s \tag{5-9}$$

where $V_{\ddot{O}}$ is an oxygen vacancy, O'_{ads} is an adsorbed oxygen, $h^{\cdot}$ is an electron hole, and s is an empty adsorption site on the surface of the MIEC. When the surface polarization is taken into account, the rate equations for these reactions can be represented as [141, 142]:

$$r_{c1} = r_{c1}^0 \left[\frac{1-\theta}{1-\theta_0} exp\left(\frac{-\alpha_1 F \Delta\chi_S}{RT}\right) - \frac{\theta c_h}{\theta_0 c_{h,0}} exp\left(\frac{(1-\alpha_1)F\Delta\chi_S}{RT}\right) \right] \tag{5-10}$$

$$r_{c2} = r_{c2}^0 \left[\frac{\theta c_v}{\theta_0 c_{v,0}} exp\left(\frac{\alpha_2 F \Delta\chi_S}{RT}\right) - \frac{1-\theta}{1-\theta_0} \frac{c_h}{c_{h,0}} exp\left(\frac{-(1-\alpha_2)F\Delta\chi_S}{RT}\right) \right] \tag{5-11}$$

where c_v and c_h are the concentrations of oxygen vacancies and holes, respectively, taken at the MIEC surface; the r^0 terms are exchange rate constants; the θ is the site fraction of absorbates; the α terms are transfer coefficients; and $\Delta\chi_S$ is the difference between the electrostatic potential drop across the surface and its equilibrium value. The subscript 0 denotes the equilibrium value. It is generally recognized that the oxygen incorporation step is a rate-limiting step [143]; therefore the surface adsorption reaction of (5-8) can be treated as in equilibrium. In this situation, there is no need to find the accurate value for r_{c1}^0; further the concentration of adsorbates on the MIEC surface should be close to equilibrium, i.e., $\Delta\chi_S \approx 0$. Accordingly the equation (5-11) can be simplified. The calculated reaction rate r_{c2} determines the magnitude of source term in Equation (5-6).

5.2.2.2 Electrochemical reaction at the cathode/electrolyte interface

At the cathode/electrolyte interface, two different materials are bonded together through sintering process. It is recognized that the vacancy transport from the electrolyte to the cathode is an electrochemical reaction [142]. The reaction rate can be represented as,

$$r_v = r_v^0 \left[exp\left(\frac{2\alpha_3 F\eta_c}{RT}\right) - \frac{c_v}{c_{v,0}} exp\left(-\frac{2(1-\alpha_3)F\eta_c}{RT}\right) \right] \tag{5-12}$$

where the c_v is the oxygen vacancy concentration at the interface; η_c is the change of electrostatic potential across the electrolyte/cathode interface. Compared to the oxygen incorporation step on the MIEC surface, the vacancy transport process across the cathode/electrolyte interface is not rate-limiting.

5.2.2.3 Electrochemical reactions in the anode

The widely used anode material is nickel-electrolyte composite. In nickel cermet composite, the electrochemical reaction takes place at the triple phase boundaries, where the gas phase (hydrogen) and electronic conducting phase (Ni) as well as ionic conducting phase (electrolyte material) meet together. The reaction rate related current density is represented using Butler-Volmer equation,

$$i_{a,ct} = i_{0,a} \left[x_{H_2} \frac{c_t}{c_{H_2,ref}} exp\left(\frac{0.5F\eta_a}{RT}\right) - x_{H_2O} \frac{c_t}{c_{H_2O,ref}} exp\left(-\frac{0.5F\eta_a}{RT}\right) \right] \tag{5-13}$$

where, $i_{0,a}$ is the exchange current density of the anode at equilibrium; x_{H_2O} and x_{H_2O} are the molar fraction of steam and hydrogen respectively; c_t the total concentration of species; and $c_{H_2O,ref}$, $c_{H_2,ref}$ are the reference concentration of steam and hydrogen respectively; and η the overvoltage. The overvoltage is defined as, $\eta_a = \phi_e - \phi_i - \Delta\phi_{eq}$, here $\Delta\phi_{eq}$ is the equilibrium potential difference.

Although the ionic transport is dominant in electrolyte materials, the electronic transport could also be involved especially for intermediate temperature electrolyte materials e.g., doped ceria. As a result, the electrochemical oxidation of hydrogen could also take place on the surface of electrolyte material in porous anode. The reaction can be represented as,

$$O_O^x + H_2 \rightarrow H_2O + 2e^- + V_{\ddot{O}} \tag{5-14}$$

Similar to the surface reaction of MIECs, the reaction rate can be calculated as,

$$r_a = r_a^0 \left[\frac{x_{H_2}}{x_{H_2,0}} exp \left(\frac{\alpha_4 F \Delta \chi_s}{RT} \right) - \frac{x_{H_2O}}{x_{H_2O,0}} \frac{c_v}{c_{v,0}} \left(\frac{c_e}{c_{e,0}} \right)^2 exp \left(-\frac{(1-\alpha_4)F\Delta\chi_s}{RT} \right) \right] \tag{5-15}$$

Here similar to MIECs, the surface overpotential $\Delta\chi_s$ is assumed to be 0.

5.2.3 Gas species transport in porous electrodes

The electrochemical reactions are closely related to fuel/gas diffusions in the anode and cathode electrodes. Since multi-species transports are involved in porous electrodes, multi-species Maxwell-Stefan's equation is employed to calculate gas species concentrations,

$$\nabla \left(-\rho\omega_i \sum_{j=1}^n D_{ij}^{eff} \left(\frac{M}{M_j} \left(\nabla\omega_j + \omega_j \frac{\nabla M}{M_j} \right) \right) \right) = R_i \tag{5-16}$$

where ρ is the density of gas; $\omega_{i/j}$ the mass fraction of gas species i/j; M_j the molecular weight of gas species j; $M = \sum_{j=1}^n x_j M_j$ the average molecular weight; x_j the molar fraction of gas species j; R_i is the reaction source term for gas species i and is related to the electrochemical current density and reaction rates in equations (5-10), (5-11), (5-13), and (5-15); D_{ij}^{eff} is the effective binary diffusion coefficients. To avoid the violation of gas species conservation, the average Bosanquet diffusion coefficient is employed [144],

$$D_{ij}^{eff} = \frac{1}{2}\frac{\varepsilon}{\tau}\left(\frac{1}{\frac{1}{D_{ij}}+\frac{1}{D_{Kn,i}}} + \frac{1}{\frac{1}{D_{ij}}+\frac{1}{D_{Kn,j}}}\right) \tag{17}$$

Here, ε and τ are porosity and tortuosity of electrode respectively; D_{ij} is the binary diffusion coefficient for a pair of gas species i and j [145]; $D_{Kn,i}$ is the Knudsen diffusion coefficient for gas species i [145].

5.2.4 Solid mechanics

The governing equations of transport processes described above are used to determine oxygen vacancy concentration distributions in the PEN structure. To further determine chemical stress induced by non-uniform distribution of oxygen vacancy concentration, the coupling between oxygen vacancy concentration and solid mechanics is needed. It is assumed that the bulk volume of ionic conducting materials changes linearly with volumetric insertion and extraction of oxygen ions. Specifically the strain due to chemical expansion effect is represented as,

$$\varepsilon_{ij}^c = \beta \Delta c \delta_{ij} \tag{5-18}$$

Where Δc is the variation of oxygen vacancy concentration, β is the chemical expansion coefficient. $\delta_{ij} = \begin{cases} 1, i = j \\ 0, i \neq j \end{cases}$.

Since this research is focused on the chemical stress in a button cell, thermal stress is neglected. Therefore, the total strain is composed of mechanical strain and chemical strain. Under the assumption that the total strain is the superposition of mechanical strain and chemical strain, we have,

$$\varepsilon_{ij} = \frac{1}{E}\left[(1+v)\sigma_{ij} - v\sigma_{kk}\delta_{ij}\right] + \beta \Delta c \delta_{ij} \tag{5-19}$$

where ε_{ij} represents the total strain components with i and j indicating the axis of the Cartesian coordinate system, σ_{ij} is the corresponding stress components; E is Young's Modulus; ν is Poisson's ratio of the material; and $\sigma_{kk} = \sigma_1 + \sigma_2 + \sigma_3$.

Rearranging equation (5-19), we may obtain the expression for stress components as,

$$\sigma_{ij} = 2\mu^* \varepsilon_{ij} + (\lambda \varepsilon_{kk} - \beta' \Delta c)\delta_{ij} \tag{5-20}$$

where, $\mu^* = \frac{E}{2(1+\nu)}$, $\lambda = \frac{2\nu\mu^*}{1-2\nu}$, $\beta' = \beta(3\lambda + 2\mu^*)$, and $\varepsilon_{kk} = \varepsilon_1 + \varepsilon_2 + \varepsilon_3$.

In elasticity, the strain tensor is related to the displacement **u** by [119],

$$\varepsilon_{ij} = \frac{1}{2}\left(\frac{\partial u_i}{\partial x_j} + \frac{\partial u_j}{\partial x_i}\right) \tag{5-21}$$

By neglecting the body forces, the equilibrium equation can be represented as,

$$\sigma_{ij,i} = 0, (j = 1,2,3) \tag{5-22}$$

Substituting equations (5-20) and (5-21) into equation (5-22), the displacement equation can be expressed as [120],

$$\mu^* \nabla^2 u_i + (\lambda + \mu^*)u_{k,ki} - \beta' \Delta c = 0, (i, k = 1,2,3) \tag{5-23}$$

Combining equations (5-6), (5-7), (5-16), and (5-23), the chemical stress in a SOFC under multi-physicochemical processes can be determined.

5.3 MODEL SETUP, BOUNDARY CONDITIONS, AND MECHANICAL PROPERTIES

The basic structure of SOFCs is a tri-layer assembly of PEN structure composed of anode electrode, electrolyte, and cathode electrode. The PEN structure should be strong enough to support mechanical loadings. This is usually achieved by using the thickest layer as the supporting layer. In the early stage of SOFC development, both

cathode electrode layer and electrolyte layer have been employed as the supporting layer respectively [146]. To reduce ohmic loss and polarization loss, the anode-supported SOFCs have been widely used since then [147]. Without loss of generality, we consider an anode-supported button cell (Figure 5.1a) with $La_{0.6}Sr_{0.4}Co_{0.2}Fe_{0.8}O_{3-\delta}$ (LSCF) cathode, $Ce_{0.9}Gd_{0.1}O_{1.95-\delta}$ (GDC) electrolyte, and nickel/GDC composite anode. Due to the symmetrical feature, a 2-D axial-symmetrical domain is employed as the computational domain for 3-D button cell. The detailed dimensions are shown in Figure 5.1b. Since the considered button cell is relatively small, the isothermal condition is considered. Also because the chemical stress is the major concern in this research, the thermal stress is neglected.
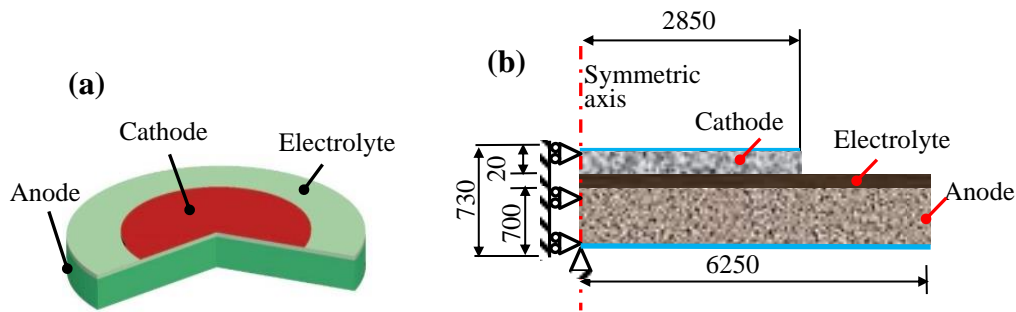
Figure 5.1 (a) Illustration of SOFC button cell; (b) FEM model of SOFC button cell (Dimension unit: μm).

5.3.1 Concentration boundary conditions

The defect concentration of conducting ceramic materials is determined at the stage when the materials are synthesized. The factors influencing defect concentration may include crystal structure and compositions. Once the material is applied for the device component, the defect concentration is also affected by operating conditions. In particular, the anode electrode is exposed to the atmosphere with extremely low oxygen partial pressure, which in turn significantly affects oxygen vacancy concentration on the

anode surface. According to the Nernst equation [148], the reversible voltage E_r of an SOFC can be represented as,

$$E_r = \frac{RT}{4F} ln \frac{P_{O_{2,c}}}{P_{O_{2,a}}} = -\frac{\Delta G^0}{2F} + \frac{RT}{4F} ln P_{O_{2,c}} + \frac{RT}{2F} ln \frac{P_{H_{2,a}}}{P_{H_2O,a}} \qquad (5\text{-}24)$$

Solving for $P_{O_{2,a}}$ from equation (5-24), one may obtain,

$$P_{O_{2,a}} = \left(\frac{1}{K_i} \frac{P_{H_2O,a}}{P_{H_{2,a}}} \right)^2 \qquad (5\text{-}25)$$

where $K_i = \exp(\frac{-\Delta G^0}{RT})$ is the equilibrium constant. Given the hydrogen and steam partial pressures in the anode, the corresponding oxygen partial pressure can be determined using equation (5-25). Then the oxygen deficit at the anode surface can be determined using such an oxygen partial pressure. Accordingly the boundary condition of oxygen vacancy/electron concentration on the anode surface can be obtained.

The oxygen partial pressure in the cathode is in the order of 0.21 atm. In this condition, the nonstoichiometric defect reaction is less likely to happen. Therefor the electrolyte material GDC is treated as a perfect electrolyte material at electrolyte/cathode interface. The corresponding boundary condition of oxygen vacancy/electron concentration is determined by doping level only.

5.3.2 Other boundary conditions

The ionic flux at the cathode/electrolyte interface is determined by equation (5-12). The electronic current leakage at the cathode/electrolyte interface is calculated by integrating surface reaction rate (equation (5-15)) over the surface of GDC phase in the anode. The humidified hydrogen is used as the fuel with the composition of H_2:H_2O:$N_2 =$ 0.96:0.03:0.01. The cathode is exposed to ambient air with composition of O_2:H_2O:$N_2 =$ 0.21:0.03:0.76. The equilibrium potential difference of the cathode and anode are

determined from experiments, i.e., $\Delta\phi_{eq,c} = 0.82V$ and $\Delta\phi_{eq,a} = 0V$. The boundary conditions for the solid mechanics are illustrated in Figure 5.1b. The surface center of the anode is point-fixed so that the chemical stress distribution in the cell will not be affected by mechanical constraints. The boundary conditions are concisely summarized in Table 5.1.

Table 5.1 Boundary conditions

Boundary	Cc/Cathode interface	Cathode/Electrolyte interface	Anode/Electrolyte interface	Cc/Anode interface	Symmetric axis/Other boundaries
Ionic flux in LSCF	Insulation	Equation (5-12)	--	--	Symmetry /Insulation
Electronic flux in LSCF	0.82V	Leakage current from GDC	--	--	Symmetry /Insulation
Electronic flux in GDC	--	Specified by GDC doping level	Continuum	Specified by P_{O_2} of feeding fuel	Symmetry /Insulation
Ionic flux in GDC	--	Equation (5-12)	Continuum	Insulation	Symmetry /Insulation
Electronic flux in Ni	--	--	Insulation	0V	Symmetry /Insulation
Mass fraction	Air composition	Insulation	Insulation	Fuel composition	Symmetry /Insulation
Mechanics	Free	Continuum	Continuum	Point fixed as shown in Figure 5.1b	Symmetry /Free

*Cc represents Current Collector.

5.3.3 Mechanical property of materials

The anode electrode is a composite porous structure composed of nickel and GDC as well as void phase. The mechanical property of the composite of nickel and GDC is first determined; then the void phase effect is taken into account. Using the composite sphere method [149] and treating the inclusion material as the phase 1, the bulk moduli of a composite material can be represented as,

82

$$\overline{K_{comp,2,1}} = K_{(2)} + \cfrac{V_{(1)}}{\cfrac{1}{\left(K_{(1)}-K_{(2)}\right)}+\cfrac{3V_{(2)}}{\left(3K_{(2)}+4G_{(2)}\right)}} \qquad (5\text{-}26)$$

where the K is the bulk modulus of the material; V is the volume fraction of a material phase in the composite; the subscripts "1" and "2" refer to the two material phases. By switching the role of phase 1 and phase 2 in equation (5-26) and treating the phase 2 as the inclusion material, we may obtain another bulk moduli $\overline{K_{comp,1,2}}$. The practical bulk moduli of the composite will be between $\overline{K_{comp,2,1}}$ and $\overline{K_{comp,1,2}}$. In this research, the average bulk modulus is utilized.

The corresponding Young's Modulus of the composite can be represented as,

$$E = 3K_{comp}(1 - 2v) \qquad (5\text{-}27)$$

When the void phase is taken into account, the effective elastic moduli of porous anode can be expressed as [51, 149],

$$E^{eff} = E_0 \frac{(1-\varepsilon)^2}{1+(2-3v_0)\varepsilon} \qquad (5\text{-}28)$$

here ε is the porosity of the composite; subscript 0 stands for the properties of the dense composite.

The oxygen partial pressure affects oxygen deficits of electrolyte GDC. The oxygen non-stoichiometry in turn strongly influences the mechanical property of GDC. To take this effect into account, the elastic modulus of GDC is expressed as the function of oxygen partial pressure [51],

$$E_{GDC} = 255.9 \times 10^9 + 3.31 \times 10^{-5}\left(-log_{10}p_{O_2}\right)^{11.11} \qquad (5\text{-}29)$$

here the unit of oxygen partial pressure p_{O_2} is Pa. Other mechanical properties of involved materials are listed in Table 5.2.

Table 5.2 Solid mechanical parameters used in the model

Parameters	Values
Young's modulus E, Ni/GDC/LSCF, [51]	219/217/161 (GPa)
Poisson's ratio ν, Cathode/Electrolyte/Anode, [51]	0.32/0.334/0.326
Density ρ, Ni/GDC/LSCF, [51]	8900/7150/6820 (kg/m^3)
Chemical expansion coefficient β, GDC/LSCF, [150]	$1.92\times10^{-6}/4.95\times10^{-6}$ (m^3/mol)
Uniaxial tensile strength σ_f, GDC/LSCF,[127-129]	250/180(MPa)

5.4 NUMERICAL SOLUTION AND MODEL VALIDATION

Table 5.3 Physical parameters used in the model

Parameters	Values
Atmospheric pressure, P_0	1[atm]
Temperature, T_0	700[^{o}C]
Inlet molar fraction of H_2 $x_{ref,H2}$	0.97
Inlet molar fraction of O_2 $x_{ref,O2}$	0.21
Tortuosity, Anode/Cathode τ*	8.5
Porosity, Anode/Cathode ε	0.35
Electronic conductivity, Anode σ_a	2×10^6 [S/m]
Exchange current, Anode/Cathode i_0*	2×10^3 /1.5×10^4 [A/m^2]
Specific surface area, Anode/Cathode A_V*	$1\times10^5/1.5\times10^7$ [1/m]
Reaction rate, LSCF/GDC r [142, 151, 152]	6×10^{-4} /**1.0×10^{-7}** [mol/m^2·s]
Diameter of spherical particle, Anode/Cathode, d_p	0.35(μm)
Ionic Mobility in GDC m_v [130]	1.2×10^{-13}(mol·m^2/J·s)
Electronic Mobility in GDC, m_e [130]	7.26×10^{-13}(mol·m^2/J·s)
Ionic Mobility in LSCF m_v [142]	2.6×10^{-14}(mol·m^2/J·s)
Electronic Mobility in LSCF, m_e [142]	1.4×10^{-12}(mol·m^2/J·s)

Note: The parameters with * are adjustable to validate the model with the experimental results.

Combining equations (5-6), (5-7), (5-16), and (5-23), we may solve for defect concentration c_j, electrical potential $\emptyset$, mass fraction of gas species ω_j, and displacement **u**, as well as their derivatives. Then the chemical stress distribution in the PEN structure can be calculated. The mathematical model is solved using commercial software package

of COMSOL Multiphysics 4.1a. The model parameters are listed in Tables 5.3. The boundary conditions are summarized in Table 5.1. The computational domain was discretized and refined until the mesh-independent solution was obtained. This mesh then was used to obtain the numerical solution. The COMSOL solver (UMFPACK) was utilized to solve the discretized equations. The general coefficient form PDEs were used to implement the charge transport in the electrodes and electrolyte, and the mass transport in porous electrodes. The solid mechanics module was employed to calculate the displacements and their derivatives.

Model validation is an important step towards further high fidelity numerical analysis. In principle, the model predictions should be able to match experimental results under identical operating conditions, including a variety of parameter distributions, polarization performance. However, it is very difficult for present techniques to measure reactants/products distribution, oxygen vacancy distribution, and stress distribution within an SOFC. Therefore, the measurable polarization performance was used to validate the model. The purpose of this validation is to examine the numerical code and determine the unknown model parameters as indicated in Table 5.3. For a specified cell voltage at the cathode electrode boundary, the corresponding species distributions and average cell current density were calculated. The cell polarization curve then was obtained by specifying a series of cell voltages and calculating the corresponding average cell current densities. The parameters denoted with "*" in Table 5.3 were adjusted so that the polarization curves predicted by the model can match with experimental results under identical operating conditions. As shown in Figure 5.2, the model predictions match the

85

experimental data reasonably well. The validated model is utilized for further numerical simulations.
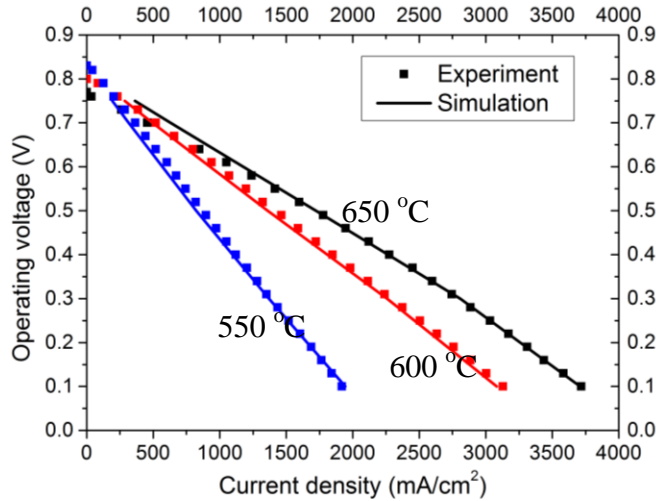
Figure 5.2 Validation of V-I curves

5.5 RESULTS AND DISCUSSION

In the following sections, the chemical stress induced by chemical-mechanical coupling in the considered button cell is systematically studied. Upon the chemical stress calculation, the failure probability is analyzed using Weibull theory and elastic energy.

5.5.1 Distributions of oxygen vacancy site fraction and chemical stress in the cell

In this section, the distribution of oxygen vacancy site fraction in the PEN structure is studied. The operating voltage of the cell is set at 0.4V as an example, the rest of the operating conditions are listed in Table 5.3. As shown in Figure 5.3a, the oxygen vacancy site fraction decreases from the anode surface towards the anode/electrolyte interface. The regime with high oxygen vacancy site fraction shows relatively large area towards the circumference of the button cell. Since humidified hydrogen is supplied to the anode, the anode is surrounded by the atmosphere with low oxygen partial pressure. Therefore the lattice oxygen would release from GDC to maintain an equilibrium and

oxygen vacancy site fraction increases. On the other hand, the oxygen ions transported from the cathode side would fill in some vacancy sites in the anode. Simulation results indicate that the ionic current density in the central area of the button cell is stronger than that in the circumference area. The combinational effects of low oxygen partial pressure and ionic current density lead to non-uniform distribution of oxygen vacancy site fraction.
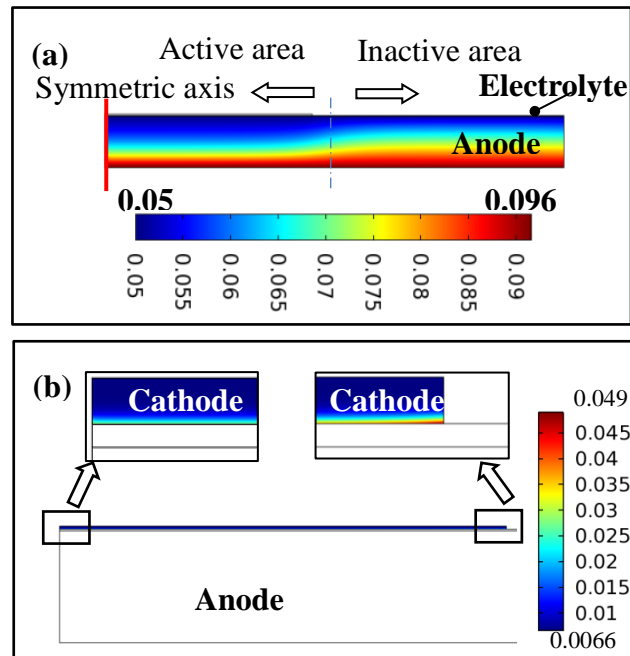
Figure 5.3 (a) Oxygen vacancy site fraction in LSCF; (b) Oxygen vacancy site fraction in GDC.

The profile of oxygen vacancy site fraction in LSCF phase is shown in Figure 5.3b. The two regions are obtained by enlarging the locations at the center and edge of the cathode respectively because the cathode is very thin. Obviously, the oxygen vacancy site fraction shows relatively uniform distribution from the cathode surface towards the cathode/electrolyte interface and maintains at a low fraction of about 0.01. Approaching the cathode/electrolyte interface, the oxygen vacancy site fraction shows a significant

increase, and reaches the maximum value of 0.049 or equivalently 1485.5 mol/m^3 at the cathode/electrolyte interface adjacent to the circumference of the cathode electrode. It is approximately six times higher than the vacancy site fraction (0.0066) on the surface of the cathode. The abrupt change might be attributed to the combinational effect of two factors. One is that the continuum condition of ionic hopping process has to be maintained at the cathode/electrolyte interface, i.e., the oxygen released from the LSCF should be equal to the oxygen gained by the GDC at the interface. However, the conductivity and the initial oxygen vacancy concentration of LSCF cathode are different from those of GDC. In order to maintain the continuum, the oxygen vacancy site fraction near the cathode/electrolyte interface has to be different from the rest regime within the cathode.

Under the mechanical constraint of point-fixed at the anode surface center (Figure 5.1b), the corresponding chemical stress distribution is shown in Figure 5.4. Here the magnitude of chemical stress is represented with different colours while the direction is indicated by arrows. The first principal stress is shown in Figure 5.4a and the third principal stress is shown in Figure 5.4b. Since the thickness of the cathode and electrolyte is very thin compared to the anode substrate, the stress distributions at the center and the circumference of the cathode as well as the circumference of the electrolyte are enlarged in order to clearly observe the details of the stress distributions. As can be seen from Figure 5.4a, the first principal stress is relatively uniform. There is a stress concentration area near the intersection point between the cathode circumference and the electrolyte. The maximum first principal stress in the cathode is about 106 MPa while that in the electrolyte is around 142 MPa, which is less than the uniaxial tensile strength of the

LSCF (180MPa) and GDC (250 MPa) respectively. The maximum first principal stress in the anode domain is about 15 MPa. The distribution of third principal stress is shown in Figure 5.4b. Relatively uniform distribution can be observed except for the cathode/electrolyte interface, where high compressive stress takes place. The maximum third principal stress is -671 MPa in the cathode domain, -530 MPa in the electrolyte domain, and -16MPa in the anode domain.
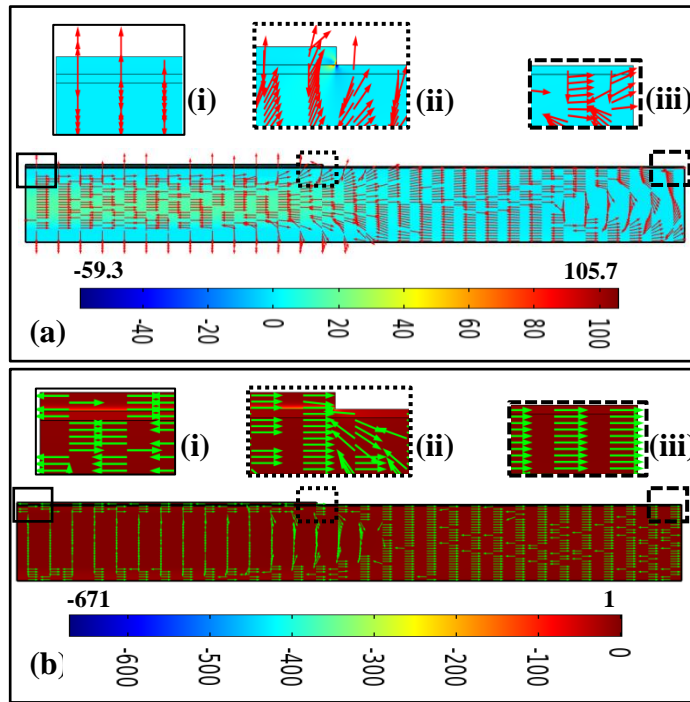
Figure 5.4 Principal stress distribution in the cell, (MPa):
(a) first Principal stress; (b) third Principal stress.

The profile of oxygen vacancy site fraction in Figure 5.3 clearly shows that oxygen vacancy concentration of LSCF phase at the cathode/electrolyte interface is relatively high, the GDC phase in the bottom part of the anode also shows relatively high oxygen vacancy concentration. The high oxygen vacancy concentration would lead to large volume expansion of bulk materials. However, the large volume expansions in these

two locations are constrained by PEN structure assembly, resulting in complicated chemical stress distribution in Figure 5.4.

5.5.2 Deformation and chemical stress of the cell under different mechanical constraints

The non-uniform distribution of oxygen vacancy fraction leads to different chemical expansions in different locations. Depending on specific mechanical constraints, the cell may have different deformations. In this section, the cell deformations are studied under the cell voltage of 0.4V and three different mechanical constraints (Figure 5.5).
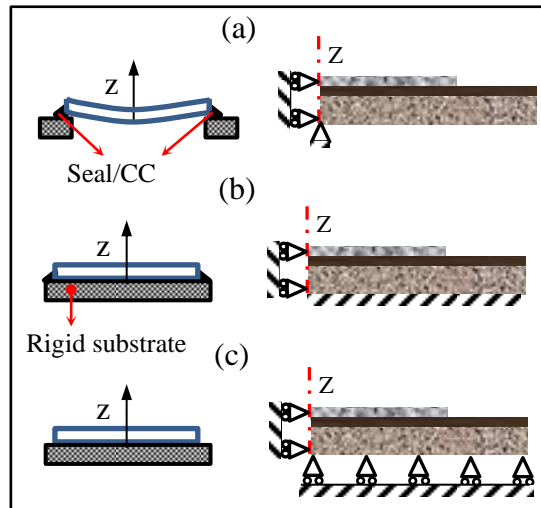
Figure 5.5 Schematic diagram showing different mechanical constraints: (a) point fixed; (b) fixed; (c) roller. (CC represent current collector)

The three typical mechanical constraints are schematically illustrated in Figure 5.5, which is originated from Atkinson [74]. The mechanical constraint in Figure 5.5a could occur in a single test, in which the sealing material around the edge of supporting anode or current collector has little effect on the deformation of the cell. This mechanical constraint is denoted as point-fixed at the anode surface center. The mechanical constraint in Figure 5.5b could take place when a single cell is assembled into a stack. In

this situation, the deformation of the cell is almost fully restricted. We denote this mechanical constraint as fixed. The mechanical constraint in Figure 5.5c could be the case, where a single cell is embedded into a stack but the friction force at the anode surface is not strong enough to restrict the deformation of the cell in radial direction. The mechanical constraint is called as roller-supported.
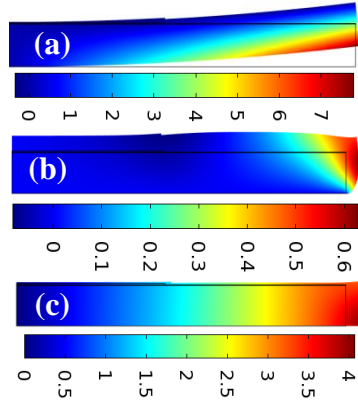
Figure 5.6 Deformation under different mechanical constraints (μm): (a) point fixed; (b) fixed; (c) roller.

Figure 5.6 shows the chemical strain distribution and deformation of the cell. For the mechanical constraint of (a), the regime near the anode circumference and surface has relatively large chemical strain, which cause the cell to bend upwards (Figure 5.6a). When the anode surface is mechanically fixed (b), the deformation is shown in Figure 5.6b. Obviously the volume of the cell is expanded towards the z-direction and circumference. The regime of circumference shows very high chemical strains. With the mechanical constraint of (c), the volume of the cell expands in r-direction. One may see the fact that the stronger mechanical constraint leads to smaller chemical strains.
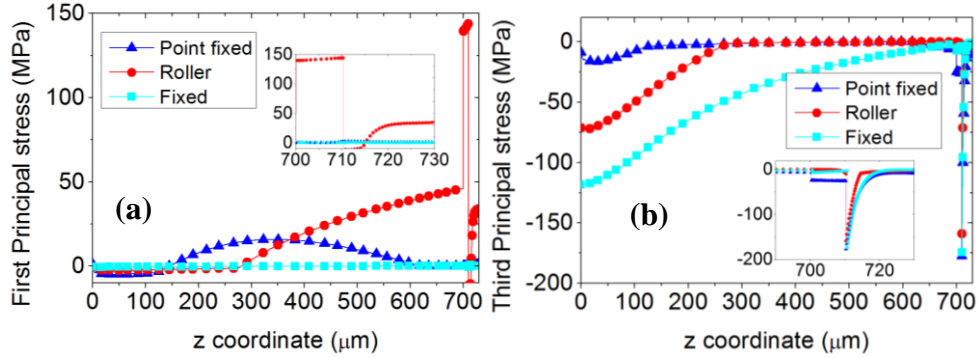
Figure 5.7 Parameter profiles along the symmetrical axis under different mechanical constrains: (a) first principal stress, (MPa); (b) third principal stress, (MPa).

The corresponding chemical stress distributions are shown in Figure 5.7. Here the horizontal-axis is defined from the center of the anode surface towards the center of the cathode surface along z-direction, in which 0 μm ~700 μm is the anode domain, 700 μm ~710 μm is the electrolyte domain, and the cathode domain is beyond 710 μm. The vertical-axis is the first principal stress (Figure 5.7a) and the third principal stress (Figure 5.7b) respectively. With the mechanical constraint of (a), the maximum first principal stress reaches 15MPa in the anode domain, the maximum third principal stress reaches -177MPa at the electrolyte/cathode interface. When the anode surface is fully fixed (constraint (b)), the first principal stress is relatively low and reaches the maximum value of 10 MPa in the anode domain. The third principal stress shows significant variations along the axial-symmetrical line. Near the anode surface, the third principal stress reaches -118 MPa and decreases towards the electrolyte. At the electrolyte/cathode interface, it shows an abruptly increases and reaches -174 MPa and then rapidly decreases to a relatively low value in the cathode domain. Under the mechanical constraint of (c), the first principal stress gradually increases from the middle point of the anode towards the electrolyte, and has an abrupt increase from 46 MPa to 139 MPa at the anode/electrolyte interface. At the electrolyte/cathode interface, the first principal stress shows an abrupt

decrease from 139 MPa to -11 MPa. Beyond the electrolyte/cathode interface, the first principal stress increases and reaches to 35 MPa in the cathode. The corresponding third principal stress shows a large compressive value of -71 MPa near the anode surface and gradually decreases to 0 MPa in the rest of the anode domain and the electrolyte. The third principal stress suddenly increases to -160 MPa at the electrolyte/cathode interface and then gradually reduces to 0 MPa in the cathode. Obviously the mechanical constraints have significant effects on chemical stress distribution. In above three cases, the electrolyte/cathode interface shows an abrupt change of the third principal stress with relatively high magnitude.

Table 5.4 Stress extremes for mechanical constraints

Stress extreme, (MPa)	Point fixed	Roller	Fixed
Max_cathode	106.5	153.4	111.33
Max_electrolyte	142	310.7	154.4
Max_anode	16.5	73.8	61.1
Min_cathode	-671	-364.2	-639.5
Min_electrolyte	-530.5	-145.7	-491.65
Min_anode	-16.6	-72.8	-1372.5

The stress extremes in each domain under three mechanical constraints are summarized in Table 5.4. For the point-fixed case (a), the maximum tensile stress (106.5 MPa) occurs in the cathode and the maximum compressive stress (-671 MPa) also occurs in the cathode. For the roller constraint case, the maximum tensile stress (310.7 MPa) takes place in the electrolyte while the maximum compressive stress (-364.2 MPa) takes place in the cathode. When the anode surface is fixed, the maximum tensile stress (154.4 MPa) is generated in the electrolyte while the maximum compressive stress (-1372.5 MPa) is generated in the anode. Obviously the fully relaxed mechanical boundary condition may facilitate to reduce the maximum chemical stress generated in the cell.

According to above numerical results, one can see that the chemical stress in a single cell is attributed to two factors. One is the volumetric expansions of bulk materials induced by non-uniform oxygen vacancy concentration distribution; another one is mechanical constraint applied on the cell. To highlight the chemical stress induced by non-uniform oxygen vacancy concentration distribution while minimizing the effect of mechanical constraints, the point-fixed constraint (Figure 5.5a) is employed throughout the research unless otherwise indicated.

5.5.3 Chemical stress under different operating conditions

The oxygen vacancy concentration distribution in SOFCs is determined by operating conditions and involved multi-physicochemical processes. Accordingly the chemical stress occurred in the PEN structure is also significantly affected by these conditions. In this section, the chemical stress under different operating conditions is systematically studied.

5.5.3.1 Cell potential effect on chemical stress

Shown in Figure 5.8a and Figure 5.8b are the oxygen vacancy site fraction distributions along the axial-symmetrical line of the cell. Obviously the oxygen vacancy site fraction decreases from the anode surface towards the electrolyte. Similar trend can be observed from the electrolyte/cathode interface towards the cathode surface. It is known that oxygen is incorporated into the LSCF matrix at the cathode electrode and transported towards the anode electrode through the electrolyte. At the anode electrode, the mobile oxygen ions in the vacancies at the GDC surface are released through electrochemical reactions; the lattice oxygen in the GDC anode could also get lost due to low oxygen partial pressure in the anode. Combining these factors together, it is not

difficult to understand that the oxygen vacancy site fraction increases from the cathode towards the anode. It is interesting to note that the overall oxygen vacancy site fraction distribution in the anode-electrolyte regime increases with increasing the applied cell voltage, however, that in the cathode domain shows an opposite trend. When the applied cell voltage is high, the corresponding cell current is low. Accordingly the oxygen ionic current from the cathode to the anode is reduced. In other words, the number of mobile oxygen vacancies transported from the anode to the cathode is decreased. Therefore the oxygen vacancy site fraction increases in the anode but decreases in the cathode when the applied cell potential is increased.
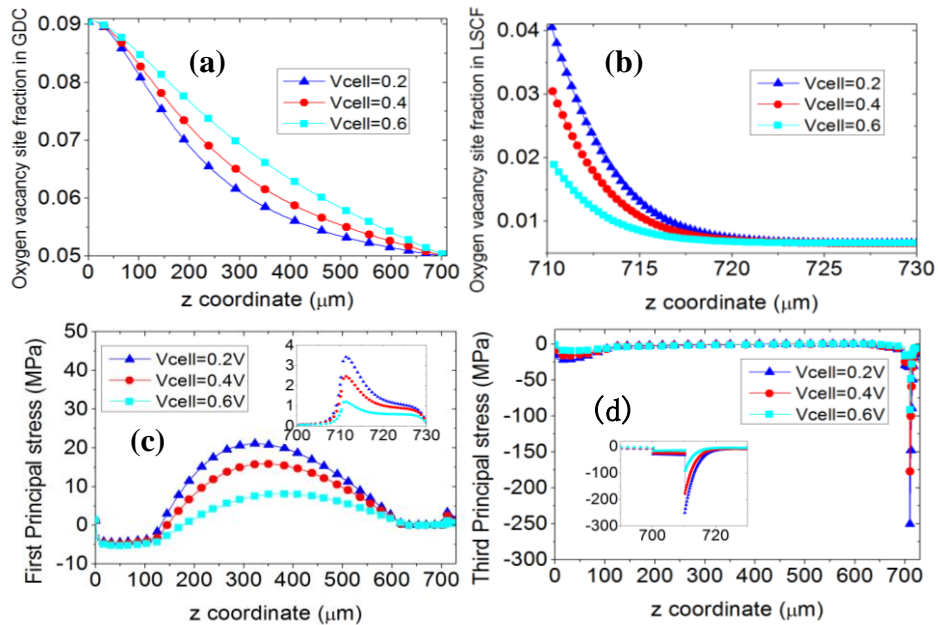
Figure 5.8 Parameter profiles along the symmetrical axis under different operating potentials: (a) oxygen vacancy site fraction in GDC, (b) oxygen vacancy site fraction in LSCF; (c) first principal stress, (MPa); (d) third principal stress, (MPa).

The non-uniform oxygen vacancy site fraction distribution leads to the fact that different locations in PEN assembly have different volumetric chemical expansions. The strains induced by chemical expansion are also confined with one another within PEN structure assembly, resulting in complicated chemical stress distribution. As shown in

Figure 5.8c, the first principal chemical stress shows two peak values, which are located within the anode electrode and at the anode/electrolyte interface respectively. The third principal chemical stress shows a peak value at the electrolyte/cathode interface (Figure 5.8d). Both the first and third principal stress increases with decreasing the applied cell voltage from 0.6V to 0.2V.
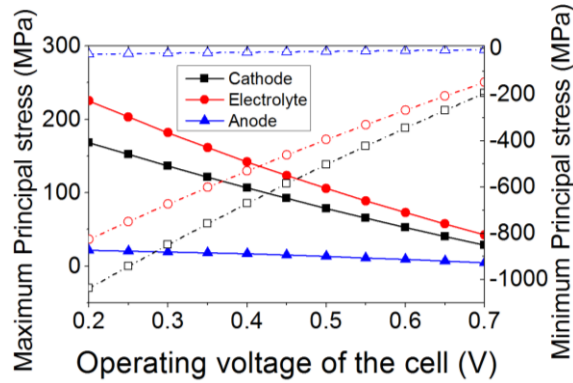
Figure 5.9 Stress extremes in each domain, (MPa)

To systematically study the applied cell voltage effects, the maximum first and third principal stress in each layer of PEN assembly are plotted in Figure 5.9. The solid line represents the maximum first principal stress while the dashed line denotes the maximum third principal stress. With increasing the applied cell voltage, the maximum first and third principal stresses in the electrolyte and cathode domains decrease, however, those in the anode domain shows negligible variations. It is interesting to note that the maximum first principal stress (tensile) in the electrolyte domain is greater than that in the cathode domain, while the maximum third principal stress (compressive stress) in the cathode domain is higher than that in the electrolyte domain. These observations indicate that the electrolyte tends to fail under tensile stress while the cathode tends to fail under compressive stress.

96

5.5.3.2 Effect of fuel composition
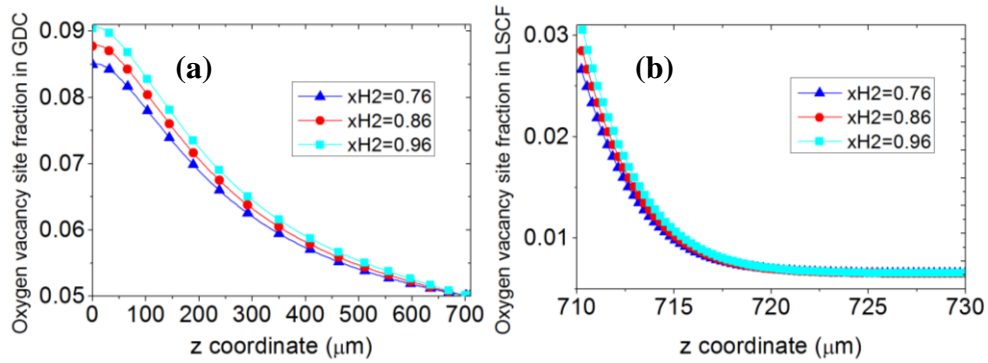
Figure 5.10 Parameter profiles along the symmetrical axis with different fuel compositions: (a) oxygen vacancy site fraction in GDC, (b) oxygen vacancy site fraction in LSCF.

The fuel composition in the anode affects oxygen partial pressure, which in turn affects the oxygen vacancy boundary condition in the anode and oxygen vacancy site fraction distribution in the PEN assembly. Therefore the fuel composition would influence chemical stress occurred in SOFC. In this section, the fuel composition effect is studied. The applied cell voltage is set at 0.4V as an example. The hydrogen is used as the fuel with nitrogen as the balance gas in the anode. As shown in Figure 5.10, with increasing the molar fraction of hydrogen from 0.76 to 0.96, the oxygen vacancy site fraction shows a slight increase in both the anode and cathode domains. Because of these slight variations, it is anticipated that the chemical stress variation will not be obvious. As shown in Figure 5.11, with increasing molar fraction of hydrogen, the maximum first principal stress demonstrates a slight increase (solid lines), e.g., from 15MPa to 16MPa in the anode domain, from 133MPa to 142MPa in the electrolyte domain, and from 99MPa to 106MPa in the cathode domain. The maximum third principal stress also shows a slight increase (dashed lines), e.g., from -15MPa to -16MPa in the anode, from -499MPa

to -530MPa in the electrolyte, and from -631MPa to -671MPa in the cathode respectively.
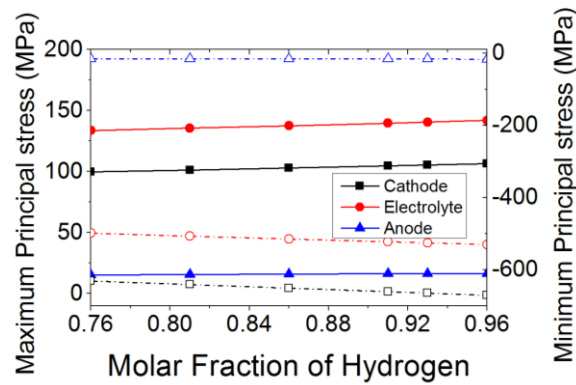
Figure 5.11 Stress extremes in each domain, (MPa)

5.5.4 Porous electrode effects on chemical stress

Porous electrodes are composed of solid phase and void phase. The void phase in the electrodes affects not only reactant/product gas diffusion but also mechanical property, e.g., Young's modulus, effective chemical expansion coefficient. In this section, the effects of porosity and tortuosity of electrodes on chemical stress will be studied. The applied cell voltage is still set at 0.4V as an example.

5.5.4.1 Porosity effects

To simplify numerical analysis, the porosity of anode electrode is assumed to be the same as that of cathode electrode. With increasing the porosity from 0.2 to 0.5, the oxygen vacancy site fraction shows a slight increase within the anode (150 μm – 650 μm, Figure 5.12a) and an obvious increase within the regime of 710 μm – 715 μm in the cathode (Figure 5.12b). This observation indicates that more mobile oxygen ions are transported from the cathode side to the anode side, generating more oxygen vacancy site fraction. The high porosity renders the fuel/gas diffusion easy and improves electrochemical reactions. The enhanced electrochemical reactions consume more

98

oxygen ions in the anode electrode. Therefore more oxygen ions are transported from the cathode side to the anode, which is consistent with above observation.

Figure 5.12 Parameter profiles along the symmetrical axis with different porosities of the electrodes: (a) oxygen vacancy site fraction in GDC, (b) oxygen vacancy site fraction in LSCF; (c) first principal stress, (MPa); (d) third principal stress, (MPa).

The corresponding chemical (first and third principal) stress distributions are shown in Figure 5.12c and d. With relative high porosity of 0.5, the first principal stress is pretty low. When the porosity is decreased from 0.5 to 0.2, the first principal stress in the anode domain shows the maximum value of -30MPa in the range of 0 – 150 μm and then becomes a tensile state with the maximum value of 30MPa in the range of 160 μm – 600 μm. Near the electrolyte/cathode interface, the first principal stress rapidly increases and reaches a peak value at the interface, and then gradually decreases to zero towards the cathode surface. The third principal stress (Figure 5.12d) shows relatively low values in the PEN assembly except for those at the electrolyte/cathode interface, where

99

extremely high compressive stress occurs. With decreasing the porosity from 0.5 to 0.2, the peak value of the third principal stress increases from -100MPa to -225MPa at the interface. The high porosity could reduce the effective expansion coefficient and Young's modulus of electrodes. Therefore the stress in the PEN assembly can be mitigated by the high porosity. It is worth mentioning that the anode electrode is much thicker than the electrolyte and cathode in the anode-supported button cell. The anode plays a dominant role on affecting chemical stress distribution in the PEN assembly.
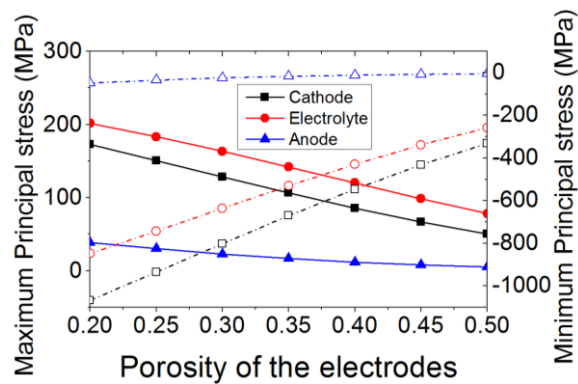
Figure 5.13 Stress extremes in each domain, (MPa)

The more systematic results are shown in Figure 5.13, where the left and right vertical axis represent the first and third principal stress extremes respectively in the anode, electrolyte, and cathode domains. With increasing the porosity from 0.2 to 0.5, the first principal stress extreme (solid line) decreases from 201MPa to 78MPa in the electrolyte, from 173MPa to 50MPa in the cathode, and from 38MPa to 5MPa in the anode. The third principal stress extreme reduces from -848MPa to -258MPa in the electrolyte, from -1068MPa to -331MPa in the cathode, and from -48MPa to -5MPa in the anode respectively. It is easy to observe that the maximum first principal stress extreme takes place in the electrolyte while the maximum third principal stress extreme occurs in the cathode.
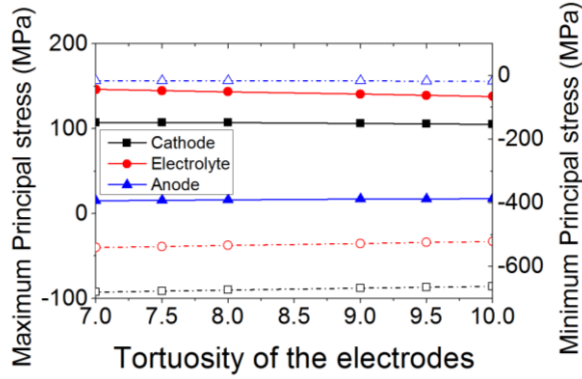
Figure 5.14 Stress extremes in each domain, (MPa)

5.5.4.2 Tortuosity effects

The tortuosity is an important parameter characterizing the porous electrode property for gas diffusion. Figure 5.14 shows the tortuosity effects on principal stress extremes in the PEN assembly. With increasing the tortuosity from 7 to 10, the first principal stress extreme decreases from 146MPa to 137MPa in the electrolyte, from 107MPa to 105MPa in the cathode, and the stress in the anode exhibits a slight increase from 15MPa to 17MPa. Similarly the maximum third principal stress reduces from -540MPa to -521MPa in the electrolyte, from -680MPa to -662MPa in the cathode, and the stress in the anode slightly increases from -16.7MPa to -17.9MPa. Compared to the porosity effect, the tortuosity effect is negligible.

5.5.5 Anode thickness effect on chemical stress

In anode-supported SOFC designs, the anode electrode is relatively thick. Therefore the anode plays an important role on determining the deformation and chemical stress in the concerned button cells. In this section, the anode thickness is varied while the corresponding chemical stress is examined.
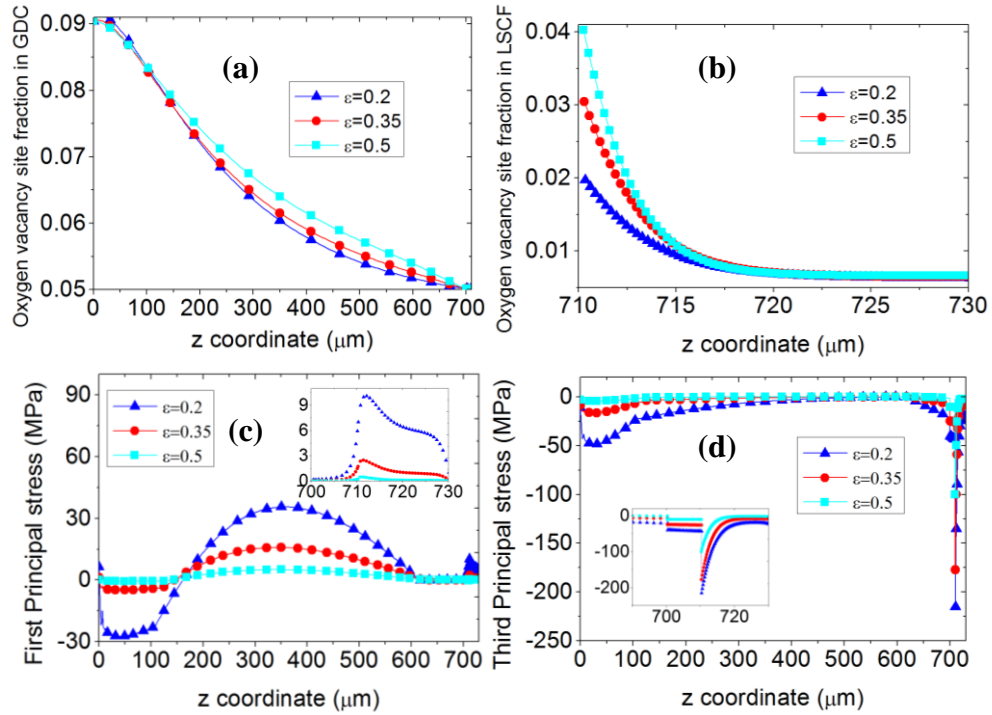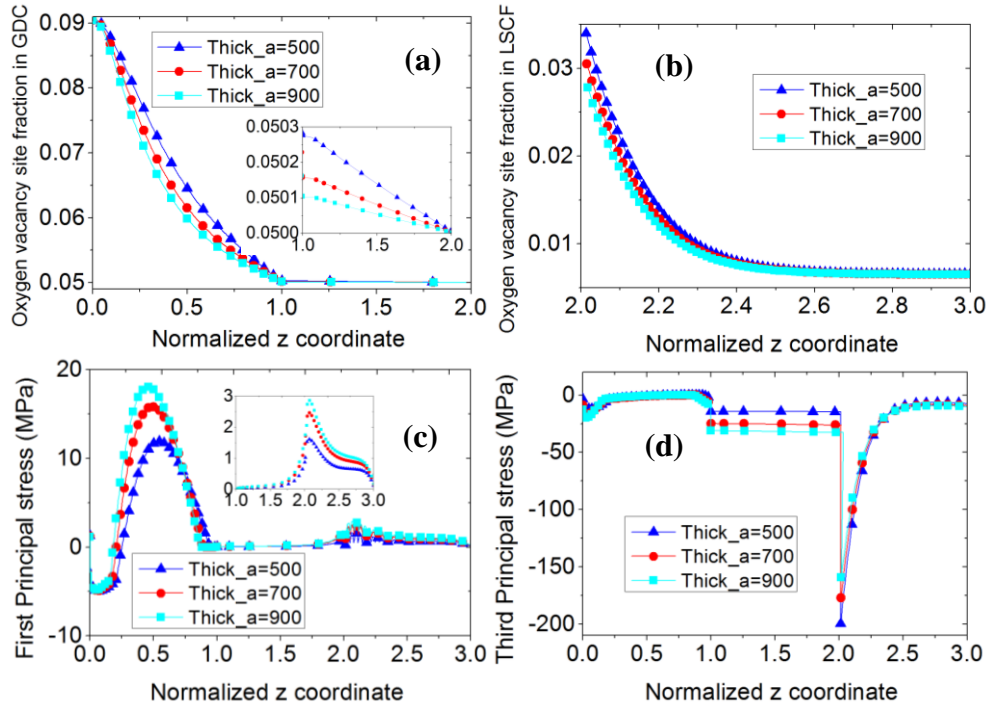
Figure 5.15 Parameter profiles along the normalized symmetrical axis with different anode thicknesses: (a) oxygen vacancy site fraction in GDC, (b) oxygen vacancy site fraction in LSCF; (c) first principal stress, (MPa); (d) third principal stress, (MPa).

The results are shown in Figure 5.15. Since the thickness of anode is different in each case, the horizontal-axis is normalized in order to obtain convenient comparisons, e.g., anode domain: $0 - 1$, electrolyte domain: $1 - 2$, and cathode domain: $2 - 3$. With increasing the thickness of anode, the oxygen vacancy site fraction shows a slight decrease in the PEN assembly along the axial-symmetrical line (Figure 5.15a and b). The corresponding first principal stress demonstrates two peak values, which are located at the middle of anode and anode/electrolyte interface respectively. The peak value increases with increasing the thickness of the anode (Figure 5.15c). The third principal stress in the electrolyte domain increases with increasing the anode thickness (Figure 5.15d). Interestingly, the third principal stress decreases at the electrolyte/cathode interface (Figure 5.15d) when the anode thickness is increased (Figure 5.15d).
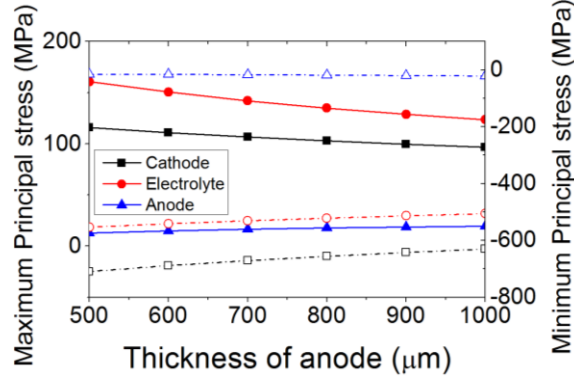
Figure 5.16 Stress extremes in each domain, (MPa)

The more systematic results are shown in Figure 5.16. With increasing the anode thickness from 500 μm to 1000 μm, the first principal stress extreme (solid line) decreases from 160MPa to 123MPa in the electrolyte domain and from 116MPa to 96MPa in the cathode domain, but increases from 12MPa to 19MPa in the anode domain. The third principal stress extreme (dashed line) decreases from 160MPa to 123MPa in the electrolyte domain and from 116MPa to 96MPa in the cathode domain, but increases from -15MPa to -21MPa in the anode domain. Therefore high anode thickness in the anode-supported SOFCs favors decreasing the chemical stress in electrolyte and cathode domain.

5.5.6 Failure probability analysis with tensile chemical stress

Ceramics especially porous ceramics are brittle materials in nature and exhibit a statistical strength scatter due to preexisting cracks in bulk materials. To obtain high fidelity analysis under complicated chemical stress conditions, we need to consider both average material strength and the degree of strength scatter. This can be achieved by using Weibull failure analysis approach [153]. For a bulk material subject to a uniaxial tensile stress σ, the survival probability can be calculated as,

$$P_s(\sigma, V) = \exp\left(- \iiint \left(\frac{\sigma}{\sigma_0}\right)^m \frac{dV}{V_0}\right) \qquad (5\text{-}30)$$

where *V* represents the volume of concerned bulk ceramics; the characteristic strength σ_0 denotes the stress level at which the survival probability is 36.8%; the *m* is the Weibull modulus controlling the degree of strength scatter, a large value of *m* indicates a small scatter while a low value of *m* corresponds to a large degree of scatter; the term V_0 is a reference volume linked to the characteristic strength σ_0.

As demonstrated above, each of component layers in the button cell is subjected to multi-axial chemical stresses. If we assume that the three principal stresses play independent role on fractural failure of the cell, the total survival probability for each layer of PEN structure assembly can be calculated as the product of the survival probability determined from each of the three principal stresses,

$$P_S^j(\bar{\bar{\sigma}}, V_j) = \prod_{i=1}^{i=3} P_S^j(\sigma_i, V_j), \text{ with}$$

$$P_S^j(\sigma_i, V_j) = \begin{cases} exp\left(-\int_{V_j}\left(\frac{\sigma_i}{\sigma_0}\right)^m \frac{dV_j}{V_0}\right) & \sigma_i \geq 0 \\ 1 & \sigma_i < 0 \end{cases} \qquad (5\text{-}31)$$

where *j* denotes the anode, electrolyte, or cathode layer; $i = 1, 2, 3$ represents three principal stresses. The failure probability then can be determined by subtracting the survival probability from 1.

Table 5.5 Weibull parameters of SOFC materials considered

Domain	Weibull modulus, m	Characteristic strength, σ_0, (MPa)	Reference volume, V_0, (mm³)
GDC	5.7[127]	183.0[127]	0.575[127]
LSCF	4.1[127]	120[127]	1.00[50]

With the Weibull approach, the failure probability of the button cell will be studied under different operating conditions based on chemical stress calculations in previous sections. The properties of SOFC materials associated with Weibull analysis are

listed in Table 5.5. Figure 5.17 shows the logarithm of failure probability of anode, electrolyte, and cathode layers under different cell voltages and hydrogen molar fractions in the fuel. With increasing the cell voltage from 0.2V to 0.7V, the failure probability decreases from $10^{-4.2}$ to $10^{-8.3}$ for the electrolyte layer, from 10^{-4} to 10^{-8} for the anode layer, and $10^{-4.4}$ to $10^{-7.7}$ for the cathode layer (Figure 5.17a). While increasing the hydrogen molar fraction in the fuel from 0.76 to 0.96, the failure probability increases from $10^{-5.6}$ to $10^{-5.3}$ for the electrolyte layer, from 10^{-5} to $10^{-4.7}$ for the anode layer, and from $10^{-5.4}$ to $10^{-5.3}$ for the cathode layer (Figure 5.17b). Therefore high cell operating voltage and low hydrogen content in the fuel may improve the reliability of button cell. However these may in turn decrease energy conversion efficiency of the cell.
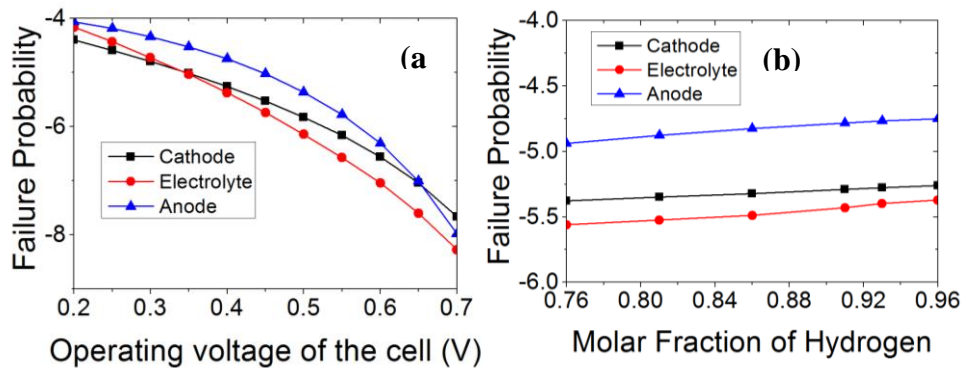
Figure 5.17 Logarithm of Failure probability in each domain as a function of: (a) Operating voltage of the cell (V); (b) Molar fraction of hydrogen.

Figure 5.18 shows the effect of porous electrode property on failure probability. With increasing the porosity of electrodes from 0.2 to 0.5, the failure probability decreases approximately from $10^{-4.5}$ to $10^{-6.8}$ for the electrolyte and cathode, and from $10^{-2.6}$ to $10^{-7.7}$ for the anode (Figure 5.18a). Below the porosity of 0.4, the anode is a vulnerable component; while above the porosity of 0.4, the electrolyte and cathode become vulnerable components. When the tortuosity of electrode is increased from 7 to

10, the failure probability decreases from $10^{-5.3}$ to $10^{-5.5}$ for the electrolyte and from $10^{-5.2}$ to $10^{-5.3}$ for the cathode, however, that of the anode increases from 10^{-5} to $10^{-4.6}$.
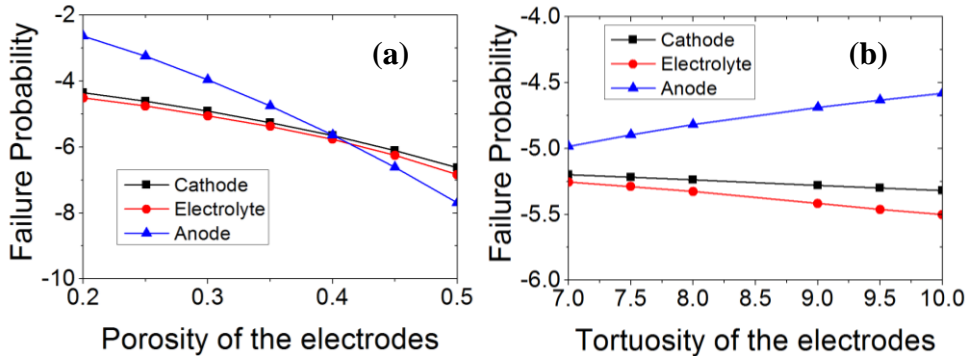
Figure 5.18 Logarithm of Failure probability in each domain as a function of: (a) Porosity; (b) Tortuosity.
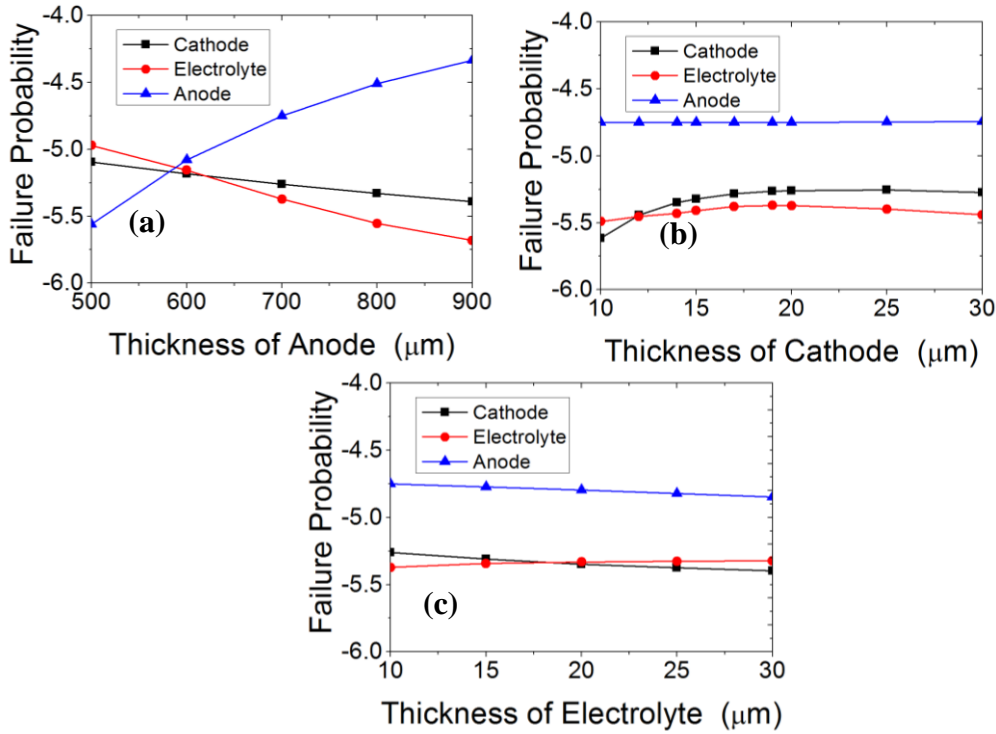
Figure 5.19 Logarithm of Failure probability in each domain as a function of: (a) anode thickness (μm); (b) cathode thickness, (μm); (c) electrolyte thickness, (μm).

The thickness effect of each layer in PEN structure assembly on failure probability is shown in Figure 5.19. Here the failure probability is calculated by varying the thickness of one layer while keeping the thickness of other two layers unchanged.

With increasing the anode thickness from 500 μm to 900 μm (Figure 5.19a), the failure probability decreases from 10^{-5} to $10^{-5.8}$ for the electrolyte and from 10^{-5} to $10^{-5.4}$ for the cathode; however this causes the increase of the anode failure probability from $10^{-5.6}$ to $10^{-4.2}$. When the cathode increases from 10 μm to 30 μm, the failure probability of the anode, electrolyte, cathode layers shows negligible variation (Figure 5.19b). Similarly the failure probability of each layer in the PEN structure assembly is not sensitive to the variation of the electrolyte thickness (Figure 5.19c). Therefore, the anode thickness plays an important role on determining the failure probability in the anode-supported button cell.

5.5.7 Delamination failure analysis with elastic energy

The Weibull approach can only take the tensile stress into account and is not able to handle the compressive stress. In the anode-supported SOFCs, the electrolyte layer and cathode layer are very thin. The delamination failure at the cathode/electrolyte interface is one of the typical failure modes for SOFCs [74]. According to previous analysis, the cathode layer is subjected to compressive stress (the third principal stress) with significant magnitude. The compressive stress could contribute significantly to the elastic energy stored in the cathode layer, which in turn may have significant effect on delamination failure of the cathode/electrolyte interface. In this section, elastic energy stored in the thin cathode layer due to stress/strain is determined to analyze the delamination failure. Given the stress/strain generated in the cathode layer, the overall stored elastic energy can be calculated by,

$$G = \iiint \frac{1}{2} \sum_{i=x,y,z} \sum_{j=x,y,z} \sigma_{ij} \cdot \varepsilon_{ij} \cdot dV \tag{5-32}$$

here the σ and ε represent stress and strain respectively.

Since the cathode/electrolyte interface is the only boundary confining the deformation of the cathode, the total stored elastic energy in the cathode layer will play an important role on the delamination failure of the cathode/electrolyte interface. If the elastic energy is greater than the critical energy, the delamination would occur.
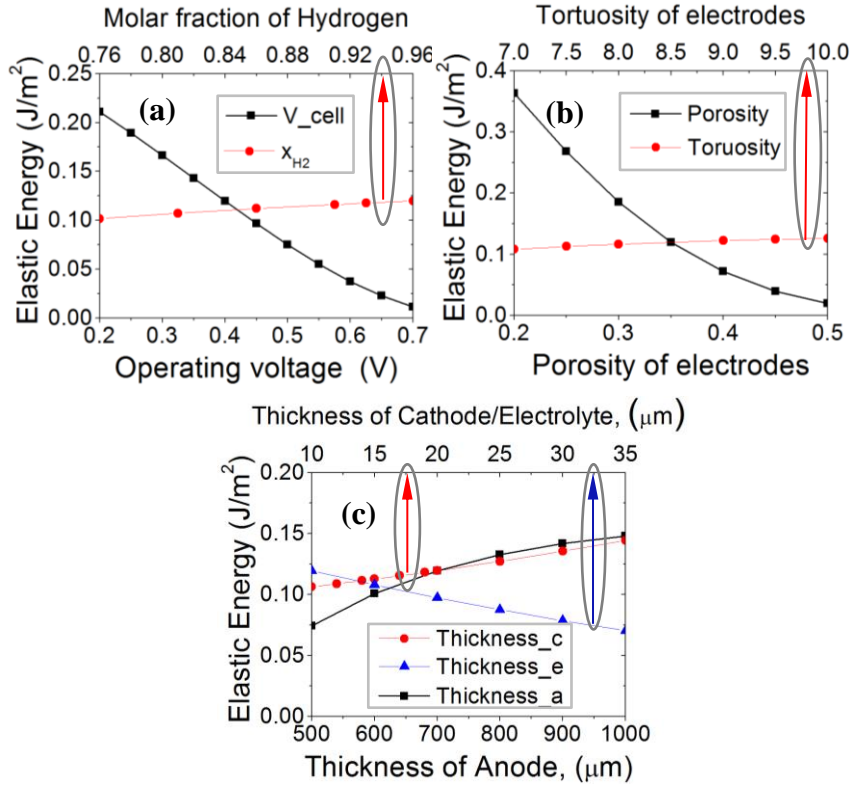
Figure 5.20 Elastic energy in cathode, (J/m^2), as a function of: (a) Operating conditions; (b) Property of the porous electrodes; (c) Thickness of each domain.

Figure 5.20 shows the variations of elastic energy stored in the cathode layer under different operating conditions. As shown in Figure 5.20a, the operating voltage demonstrates significant effect on elastic energy of cathode layer: decreasing from 0.21 J/m^2 to 0.01 J/m^2 with increasing the voltage from 0.2V to 0.7V; the effect of hydrogen molar fraction is negligible. Figure 5.20b clearly indicates that the elastic energy is reduced from 0.36 J/m^2 to 0.02 J/m^2 when the porosity of electrodes increases from 0.2 to

0.5; the variation of electrode tortuosity doesn't lead to obvious change of elastic energy. Figure 5.20c shows the thickness effect of each layer. With increasing the anode thickness from 500 μm to 1000 μm, the elastic energy increases from 0.07 J/m^2 to 0.15 J/m^2. When the cathode thickness increases from 10 μm to 35 μm, the elastic energy is increased from 0.1 J/m^2 to 0.14 J/m^2. However, increasing the electrolyte thickness leads to the decrease of elastic energy from 0.12 J/m^2 to 0.07 J/m^2. Therefore, relatively thinner anode and cathode, and thicker electrolyte can mitigate probability of delamination failure at the cathode/electrolyte interface in anode-supported SOFCs. Given the critical bonding energy of 4 J/m^2 at the cathode/electrolyte interface [74], none of above cases can lead to the delamination failure at the cathode/electrolyte interface.

5.6 CONCLUSIONS

A comprehensive model is developed to study chemical-mechanical coupling phenomenon in an anode-supported SOFC. The model for the first time links oxygen ionic transport process with chemical stress generated in the PEN structure assembly of a button cell under multi-physicochemical operating conditions. This is an important module complementary to the state-of-the-art electrochemical-thermal-mechanical modeling of SOFCs. The model is partially validated using the measured polarization performance, upon which systematic simulations are carried out. Results show that multi-physicochemical operating conditions lead to non-uniform distribution of oxygen vacancy site fraction in the PEN assembly. Different oxygen vacancy concentration causes different volumetric expansion of bulk material. Therefore chemical stress occurs in PEN assembly. The chemical stress distribution is also strongly dependent on mechanical constraints applied on the cell. Without mechanical constraint, the peak value

of the first principal stress occurs within the anode electrode and at the anode/electrolyte interface; the third principal stress shows a peak value at the cathode/electrolyte interface. The chemical stress particularly the peak values of the first and third principal stress can be mitigated by increasing the cell operating voltage (i.e. decreasing cell current). The hydrogen molar fraction in the fuel shows slight effect on chemical stress. The porosity of electrodes shows significant effects on chemical stress. Bigger porosity can significantly decrease the extremes of first and second principal stresses in PEN assembly. The effect of electrode tortuosity is negligible on chemical stress. Larger anode thickness in the anode-supported SOFCs increases the chemical stress in the anode electrode but favors decreasing the chemical stress in electrolyte and cathode domain. The Weibull analysis shows that high cell operating voltage and low hydrogen content in the fuel may mitigate failure probability of PEN assembly. With relatively low electrode porosity, the anode electrode is a vulnerable component in the anode-supported button cell; with relatively high electrode porosity, the electrolyte and cathode layer become vulnerable components. Large anode thickness can mitigate failure probability of electrolyte and cathode layer but increase anode failure probability. The failure probability is not sensitive to the thickness variations of electrolyte and cathode layers. Relatively thinner anode and cathode, and thicker electrolyte as well as high operating cell voltage can reduce the elastic energy stored in the cathode layer and therefore mitigate the probability of delamination failure at the cathode/electrolyte interface in anode-supported SOFCs.

CHAPTER 6

IMPEDANCE SPECTRA STUDY OF POLYCRYSTALLINE MIXED CONDUCTORS

UNDER MECHANICAL STRESS: A CASE STUDY OF CERIA

6.1 INTRODUCTION

Doped ceria have been widely used as electrolyte materials for intermediate temperature solid oxide fuel cells, such as $Sm_{0.2}Ce_{0.8}O_{1.9-\delta}$ (SDC), $Gd_{0.1}Ce_{0.9}O_{1.95-\delta}$ (GDC) [154, 155]. To study the doped ceria electrolyte property, symmetrical cell is generally fabricated, where the dense electrolyte is sandwiched by metal (e.g., platinum) electrode on either side. The electrochemical impedance spectroscopy (EIS) obtained from the symmetrical cell typically demonstrates a half tear-drop-shaped feature in the Nyquist plot. To interpret such EIS curves while extracting material properties such as bulk transport property and surface exchange rate for electrochemical reactions, EIS modeling approaches have been widely employed. At the early stage of EIS modeling development, equivalent circuit model (ECM) has been extensively employed [156-158]. ECM is usually obtained by wiring up a set of resistors and capacitors to form an electrical network, representing physical processes in conducting ceramics. However, the electrical elements could be re-arranged in different ways in electrical network while still generating the same IS curve, rendering the interpretation of IS data ambiguous. To overcome this issue, the flux equations of charged species are used to map the physical processes in ceramic conductors with electrical elements in the network of ECM. This method is built upon the

original work of Warburg's analysis [159], and since then is extensively advanced by Macdonald [160-164], Brumleve and Buck [165, 166], Jamnik and Maier [167, 168], and Horno *et al.* [169]. Lai and Haile significantly advanced this modeling method for the interpretation of doped ceria impedance data [170]. Ciucci et al. recently extended this EIS modeling method to the 2D ceria study [171]. To interpret the half tear-drop-shaped EIS curve of symmetrical cells, another class of modeling method has also been explored, where the sinks/sources in materials are introduced into the model and the surface reaction steps of electrodes are also considered. Classic work includes Boukamp [172, 173], Adler [174, 175], Sluyters-Rehbach and Sluyters [176], Robertson and Michaels [177], and the pioneering work of of Gerischer [178].

When doped ceria electrolyte is embedded into the structure of solid oxide fuel cells (SOFCs), it would be subject to various loadings, such as thermal stress loading [51] and chemical stress loading [62, 68, 139] as well as mechanical loading. The stresses have been identified as a major degradation mechanism limiting the industrial development of SOFCs. The conductivity of doped ceria could also be affected by the applied stresses. Araki has shown that the ionic conductivity of single crystal bulk YSZ material can be improved by applying external uniaxial tensile load [179, 180]. The electrolyte materials in practical SOFCs are polycrystalline, composed of a large number of crystallites which are bonded together through highly defective boundaries. We recently studied the conductivity of polycrystalline doped ceria under uniaxial tensile mechanical loads using four-probe and EIS techniques (the experimental will be reported in a separate research work). The EIS data from four-probe technique is not well interpreted, particularly for polycrystalline doped ceria under uniaxial tensile mechanical loads.

Built upon the approach developed by Lai and Haile [181], the advancement of EIS modeling is present and employed to interpret the EIS data of doped ceria (SDC) at elevated temperatures under uniaxial mechanical tensile loads. By fitting the model predictions with experimental data, the physical properties of polycrystalline SDC are extracted. The effects of mechanical stress on the conductivities of grains and grain boundaries are elucidated.

6.2 DESCRIPTION OF DEFECT TRANSPORT PROCESSES IN MIECS AND EIS MODELING

A mixed ionic and electronic conductor (MIEC) solid solution is capable of conducting multiple charged species. There are two fundamental equations governing such transport processes. One is the continuity of charged species, driven by the electrochemical potential. Another one is the Poisson's equation relating the electrical potential field with the charges in the system. It is worth noting that the MIECs are usually polycrystalline in practical devices. Accordingly the Poisson's equation within grain boundaries is modified using the grain boundary core-space-charge layer model. In the following sections, the governing equations are described in details.

6.2.1 Charge Transport in MIEC solid solution

The electrochemical potential of a defect species in an ideal solid solution is represented by [77]:

$$\mu_j = \mu_{0,j} + RT \ln x_j + z_j F \phi \qquad (6\text{-}1)$$

Where μ_j is the electrochemical potential of species j; R the gas constant; T the temperature; x_j the molar fraction of species j; z_j the effective charge of species j; F the Faraday's constant; ϕ the potential.

The driving force for charge transport in a solid solution is the gradient of electrochemical potential. According to non-equilibrium thermodynamics, the current density of a charged species in a solid solution driven by an electrochemical potential can be expressed as,

$$J_j = -\frac{z_j F c_j D_j}{RT} \nabla \mu_j \tag{6-2}$$

Where $D_j = RTm_j$ is the diffusion coefficient of the species j; m_j is the mobility of the species j; c_j is the concentration of diffusion component, e.g., oxygen vacancy, electron or hole.

Substitution of Equation (6-1) into (6-2) gives,

$$J_j = -\left(z_j FD_j\right)\nabla c_j - \frac{z_j F c_j (z_j FD_j)}{RT} \nabla \phi \tag{6-3}$$

Clearly, the diffusion of mobile defects in a solid solution is driven by the gradients of mobile species concentration and the electrical potential field.

Substituting the Equation (6-3) into the equation of species conservation, $\frac{\partial c_j}{\partial t} \cdot z_j F + \nabla \cdot J_j = 0$, we have,

$$\frac{\partial c_j}{\partial t} \cdot z_j F + \nabla \cdot \left(-\left(z_j FD_j\right)\nabla c_j - \frac{z_j F c_j (z_j FD_j)}{RT} \nabla \phi\right) = 0 \tag{6-4}$$

Equation (6-4) is used to describe the transport process of charged species in a solid solution, e.g., oxygen vacancy and electron or hole. When the steady-state condition is considered, the first term at the left side of Equation (6-4) disappears.

6.2.2 Poisson's equation

The overall charge density distribution is closely related to the electrical potential distribution within a grain domain and is described by the Poisson's equation [181],

$$-\varepsilon_r \varepsilon_0 \frac{\partial^2 \phi(x,t)}{\partial x^2} = \sum_j z_j F c_j(x,t) \tag{6-5}$$

where ε_0 is the vacuum permittivity and ε_r is the dielectric constant or relative permittivity of the material.

As mentioned above, the doped ceria electrolyte is generally polycrystalline in practical SOFCs, consisted of grains and grain boundaries. The Poisson's equation can mathematically describe the relations between the electrical potential distribution and charge density distribution in a grain. However, it cannot be directly used for grain boundaries due to the presence of space charge layer.
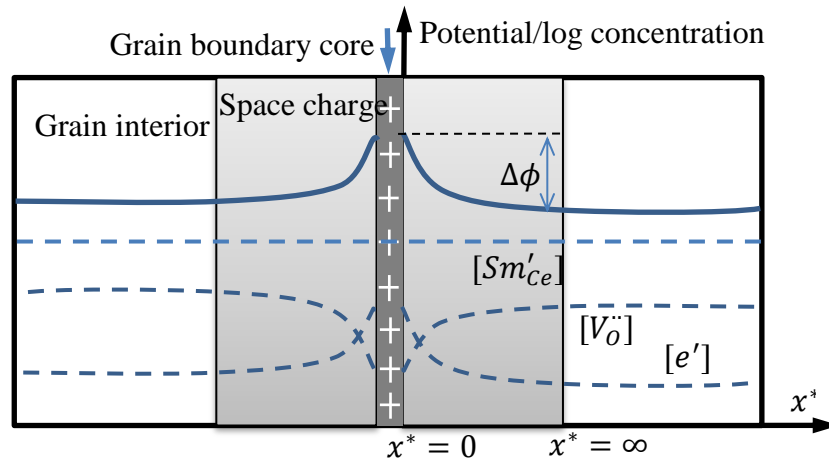
Figure 6.1 Schematic potential and concentration profiles in grain boundary

A grain boundary is the crystallographic mismatch zone between two grains. The defect structure of grain boundaries is different from that of grains. Taking the $Sm_{0.15}Ce_{0.85}O_{1.925-\delta}$ (SDC) material as an example, to achieve the thermodynamic equilibrium, Sm segregation takes place at the SDC grain boundaries. The segregation of Sm at the grain boundary leads to the depletion of oxygen vacancies and the accumulation of electrons, forming a space-charge layer. The space-charge theory is then suggested based on the experimental observations[182]. As shown in Figure 6.1, the grain boundary consists of a grain boundary core and two adjacent space charge layers. It is generally realized that compared to the concentrations of dopants, the concentrations of

ions and electrons are negligible in the space charge region, i.e., $c_v, c_e \ll c_a$ [183].

Therefore the Poisson's equation for grain boundary becomes,

$$-\varepsilon_r \varepsilon_0 \frac{\partial^2 \phi(x,t)}{\partial x^2} = -F c_a \tag{6-6}$$

6.2.3 Perturbation analysis for impedance calculation

In experiment, impedance is obtained by linear perturbation method. A periodic current perturbation with a small magnitude is applied to a steady state system. The corresponding voltage perturbation is measured. By varying the frequency of current perturbations from very low to extremely high, a series of voltage perturbations are obtained. The impedance then can be calculated using the ratio between voltage perturbations and corresponding current perturbations.

When a current perturbation is applied to an equilibrium system, all parameter variables involved in the system will have perturbations, such as electrical potential, species concentration, and charged species flux. Mathematically, we have

$$\begin{cases} \phi(x,t) = \phi(x) + \Delta\phi(x,t) \\ c_j(x,t) = c_j(x) + \Delta c_j(x,t) \\ J_j(x,t) = J_j(x) + \Delta J_j(x,t) \end{cases} \tag{6-7}$$

where $\phi(x)$, $c_j(x)$, and $J_j(x)$ represent electrical potential, species concentration, and charge flux in steady state respectively while $\Delta\phi(x)$, $\Delta c_j(x)$, and $\Delta J_j(x)$ represent the corresponding perturbations.

Substituting (6-7) into Equations (6-4) and (6-5), subtracting the corresponding steady state equations while neglecting the second-order terms, yield,

$$\frac{\partial \Delta c_j(x,t)}{\partial t} \cdot z_j F + \frac{\partial}{\partial x}\left(\Delta J_j(x,t)\right) = 0 \tag{6-8}$$

$$-\varepsilon_r \varepsilon_0 \frac{\partial^2 \Delta\phi(x,t)}{\partial x^2} = \sum_j z_j F \Delta c_j(x,t) \tag{6-9}$$

Here $\quad \Delta J_j(x,t) = -\left(z_j F D_j\right)\frac{\partial}{\partial x}\left(\Delta c_j(x,t)\right) - \frac{z_j F(z_j F D_j)}{RT}\Delta c_j(x,t) \cdot \frac{d\phi(x)}{dx} - \frac{z_j F(z_j F D_j)}{RT}c_j(x) \cdot$

$\frac{\partial}{\partial x}(\Delta\phi(x,t))$.

Since Equation (6-8) holds for each kind of charge species, summing up all kinds of species, we have,

$$-\frac{\partial}{\partial t}\left(\sum_j z_j F \Delta c_j(x,t)\right) = \frac{\partial}{\partial x}\left(\sum_j \Delta J_j(x,t)\right) \qquad (6\text{-}10)$$

Combining Equations (6-10) and (6-9), we obtain,

$$\frac{\partial}{\partial x}\left(\sum_j \Delta J_j(x,t)\right) + \frac{\partial}{\partial x}\left(-\frac{\partial}{\partial t}\left(\varepsilon_r \varepsilon_0 \frac{\partial \Delta\phi(x,t)}{\partial x}\right)\right) = 0 \qquad (6\text{-}11)$$

Equation (6-11) indicates that the total charge flux $\Delta J_T(t)$ is composed of every charge flux and a displacement flux $\Delta J_{dis}(x,t)$ induced by time-varying electrical field, i.e.,

$$\Delta J_T(t) = \sum_j \Delta J_j(x,t) + \Delta J_{dis}(x,t), \text{ with } \Delta J_{dis} = -\frac{\partial}{\partial t}\left(\varepsilon_r \varepsilon_0 \frac{\partial \Delta\phi(x,t)}{\partial x}\right). \qquad (6\text{-}12)$$

To simplify the problem into a manageable form, we consider the case where the majority of mobile defects are vacancies and electronic species only. The Laplace transform of Equations (6-8) and (6-9) yields,

$$-i\omega \Delta c_v(x,\omega) \cdot z_v F = \frac{\partial}{\partial x}\left(-\left(z_v F D_v\right)\frac{\partial}{\partial x}\left(\Delta c_v(x,\omega)\right) - \frac{z_v F(z_v F D_v)}{RT}\Delta c_v(x,\omega) \cdot \frac{d\phi(x)}{dx} - \right.$$

$$\left. \frac{z_v F(z_v F D_v)}{RT}c_v(x) \cdot \frac{\partial}{\partial x}(\Delta\phi(x,\omega))\right) \quad (6\text{-}13)$$

$$-i\omega \Delta c_e(x,\omega) \cdot z_e F = \frac{\partial}{\partial x}\left(-\left(z_e F D_v\right)\frac{\partial}{\partial x}\left(\Delta c_e(x,\omega)\right) - \frac{z_e F(z_e F D_e)}{RT}\Delta c_e(x,\omega) \cdot \frac{d\phi(x)}{dx} - \right.$$

$$\left. \frac{z_e F(z_e F D_e)}{RT}c_e(x) \cdot \frac{\partial}{\partial x}(\Delta\phi(x,\omega))\right) \quad (6\text{-}14)$$

$$-\varepsilon_r \varepsilon_0 \frac{\partial^2 \Delta\phi(x,\omega)}{\partial x^2} = z_v F \Delta c_v(x,\omega) + z_e F \Delta c_e(x,\omega) + z_a F \Delta c_a(x,\omega) \qquad (6\text{-}15)$$

In the grain boundary, $z_v F \Delta c_v(x,\omega), z_e F \Delta c_e(x,\omega)$ terms on the right of Equation (6-15) disappear according to grain boundary core-space-charge layer model. It is worth

to notify that there are 6 unknowns: the profiles of $\phi(x)$, $c_v(x)$ and $c_e(x)$ under steady state, as well as their perturbations, $\Delta\phi(x,\omega)$, $\Delta c_v(x,\omega)$ and $\Delta c_e(x,\omega)$.

The impedance spectroscopy then can be obtained using the perturbations of electrical potential and the total charge flux [184]:

$$Z^*(\omega) = \frac{\Delta\phi(L,\omega)-\Delta\phi(0,\omega)}{\Delta J_T(\omega)} \tag{6-16}$$

$$\begin{cases} \Delta J_v = -(z_v F D_v)\frac{\partial}{\partial x}\left(\Delta c_v(x,\omega)\right) - \frac{z_v F(z_v F D_v)}{RT}\Delta c_v(x,\omega)\cdot\frac{d\phi(x)}{dx} - \frac{z_v F(z_v F D_v)}{RT}c_v(x)\cdot\frac{\partial}{\partial x}\left(\Delta\phi(x,\omega)\right) \\ \Delta J_e = -(z_e F D_v)\frac{\partial}{\partial x}\left(\Delta c_e(x,\omega)\right) - \frac{z_e F(z_e F D_e)}{RT}\Delta c_e(x,\omega)\cdot\frac{d\phi(x)}{dx} - \frac{z_e F(z_e F D_e)}{RT}c_e(x)\cdot\frac{\partial}{\partial x}\left(\Delta\phi(x,\omega)\right) \\ \Delta J_{dis} = -\varepsilon_r\varepsilon_0\frac{\partial\Delta\phi(x,\omega)}{\partial x} \\ \Delta J_T = \Delta J_v + \Delta J_e + \Delta J_{dis} \end{cases}$$

6.3 MODEL SETUP, AND BOUNDARY CONDITIONS
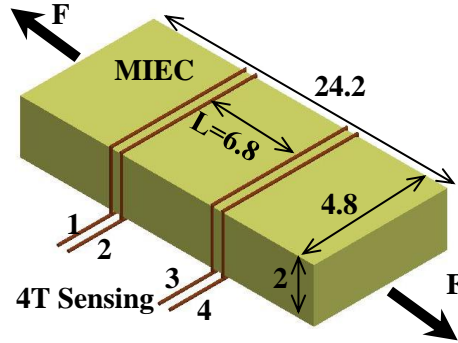
Figure 6.2 Schematic representation of experimental setup,(Dimension unit: mm)

We consider a polycrystalline MIEC $Sm_{0.2}Ce_{0.8}O_{1.9-\delta}$ (SDC) bar. The commercial $Sm_{0.2}Ce_{0.8}O_{1.9-\delta}$ (SDC20) powders are uni-axially pressed at 200MPa and then sintered at 1450^oC for 10 hours. The dimensions of the sintered sample bar are 2 mm $\times$ 4.8 mm $\times$ 24.2 mm as shown in Figure 6.2. The impedance response of the specimen under mechanical stress is measured using four-terminal technique. Four-terminal silver wires are bound on the surface of the specimen using silver paste. A uniaxial tensile load is

applied to the sample. The temperature of the specimen assembly is controlled by a test furnace in air.

This experimental system is used as a physical base for mathematical model development. For simplification, one-dimensional (1-D) model is considered. As shown in Figure 6.3, the length of 1-D computational domain is 3.4mm and consists of grains and grain boundaries. It is assumed that the grains and grain boundaries are uniformly distributed. The grain size is 4 μm, therefore there are nearly 750 grains in the computational domain. The symmetric axis is located at x=0; and the silver electrode boundary is set at x=L/2. Here, GB represents grain boundary; GI is grain interior; SC is space charge; Ag is the silver wire.
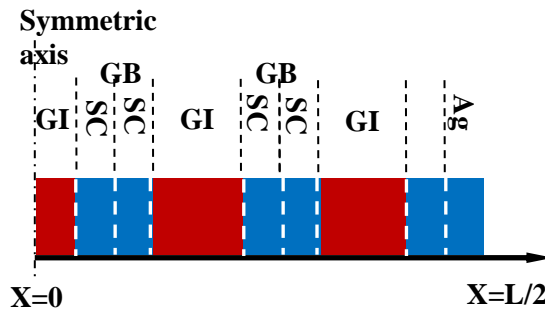
Figure 6.3 Schematic representation of model setup

6.3.1 Charge transport boundary condition under steady state

For charge transport in the solid solution, the elementary electrode kinetics is assumed and is taken into account by Change-Jaffe boundary conditions at the electrodes [167]:

$$J_j\left(x = \tfrac{L}{2}\right) = -z_j F k_j \left(c_j\left(x = \tfrac{L}{2}\right) - c_j^{eq}\left(x = \tfrac{L}{2}\right)\right) \tag{6-17}$$

The superscript "eq" refers to the equilibrium value. The reaction rate constants k_j for species j are vanishing in the limit of completely blocking electrodes and are very

high in the limit of completely reversible electrodes. Therefore, they have different values for different carriers. Since the silver is used as the current collector, which is a reversible electrode for electrons and a blocking electrode for ions respectively. Accordingly, the reaction rate constant for electrons is much larger than that for ions, which are shown in Table 6.1.

Defining a charge transfer resistance, R_j, which relates the chemical potential drop at the interface to the flux across the interface, $R_j = \frac{R_g T}{(z_j F)^2 k_j c_j}$. For silver electrode, approximately that $R_e = 0$ and R_v has a finite magnitude.

At x=0, all the charged species concentrations of the material system should be mirror symmetric with respect to the symmetric axis, accordingly,

$$c_j(x = 0) = 0 \qquad (6\text{-}18)$$

6.3. 2 Electric potential boundary condition under steady state

Under steady state conditions, there is no electric potential drop across the mixed conducting ceramic specimen. So the potential is 0 at both the symmetric axis and computational domain boundary:

$$\phi\left(x = \frac{L}{2}\right) = 0; \phi(x = 0) = 0 \qquad (6\text{-}19)$$

However, when the space charge layers are considered in the model, there will be an electric potential introduced in each grain boundary by the positively charged grain boundary core, as displayed in Figure 6.1. Accordingly, the electric boundary in the space charge layer needs to follow the grain boundary core-space-charge layer model.

In the grain interior region ($x^* = \infty$), the potential is assumed to be zero; at the grain boundary core ($x^* = 0$), the potential reaches the maximum ϕ_0 .So the boundary conditions are chosen as:

$$\varphi(x^* = 0) = \varphi_0, \; \varphi(x^* = \lambda_S) = \frac{d\varphi}{dx}\big|_{x^*=\lambda_S} = 0 \tag{6-20}$$

Here λ_S is the width of arbitrary space charge layer. It is worth mentioning that there are 750 grain boundaries, the condition on each grain boundary needs to be applied appropriately.

6.3.3 Boundary Conditions in frequency domain

Under transit condition, charge transport boundaries are in the same formats as those under steady state in Equation (6-17) and (6-18), except that J_j and c_j is dependent on both x and t. Plugging Equation (6-7) into transit form of Equation (6-17) and (6-18) and employing the steady-state solution, we have,

$$\begin{cases} \Delta J_j\left(\frac{L}{2}, t\right) = -z_j F k_j \Delta c_j\left(\frac{L}{2}, t\right) \\ \Delta c_j(0, t) = 0 \end{cases} \tag{6-21}$$

The Laplace transform of boundary conditions (6-21) from time domain to frequency domain, gives,

$$\begin{cases} \Delta J_j\left(\frac{L}{2}, \omega\right) = -z_j F k_j \Delta c_j\left(\frac{L}{2}, \omega\right) \\ \Delta c_j(0, \omega) = 0 \end{cases} \tag{6-22}$$

However, under the assumptions of Chang-Jaffe boundary conditions, there is no capacitance explicitly due to the interface. If the ionic capacitance of the current collector/mixed conductor interface is not negligible, the boundary conditions can be written as:

$$\begin{cases} \Delta J_j\left(\frac{L}{2}, \omega\right) = \frac{1}{Z_j^*\left(\frac{L}{2}, \omega\right)}\left(\frac{\Delta c_j\left(\frac{L}{2}, \omega\right)}{c_j\left(\frac{L}{2}\right)} \frac{R_g T}{z_j F}\right) \\ \Delta c_j(0, \omega) = 0 \end{cases} \tag{6-23}$$

Where, $Z_j^*\left(\frac{L}{2}, \omega\right)$ is the parallel resistance-capacitance (RC) circuit due to the interface reaction. Since silver current collector is perfectly reversible to electrons, then

121

$R_e\left(\frac{L}{2}\right) = 0, \frac{1}{Z_e^*\left(\frac{L}{2},\omega\right)} = \infty$. For oxygen vacancy, $R_v\left(\frac{L}{2}\right)$, $C_v\left(\frac{L}{2},\omega\right)$ have finite values, so

$Z_v^*\left(\frac{L}{2}\right) = \frac{1}{\frac{1}{R_v\left(\frac{L}{2}\right)} + C_i(i\omega)^\alpha}$, with $R_v\left(\frac{L}{2}\right) = \frac{R_gT}{(z_vF)^2 k_v c_v\left(\frac{L}{2}\right)}$, $C_v\left(\frac{L}{2},\omega\right) = C_i(i\omega)^\alpha$. Here, a

Constant Phase Element (CPE) is employed to take into account an imperfect capacitor at the current collector/mixed conductor interface.

After employing the steady-state boundary (6-19), the electrical potential perturbation applied across the specimen is: $\Delta\phi(0,t) = 0$; $\Delta\phi\left(\frac{L}{2},t\right) = V(\frac{L}{2})(e^{i\omega t})$. Laplace transform of these boundaries, we have,

$$\Delta\phi(0,\omega) = 0; \Delta\phi\left(\frac{L}{2},\omega\right) = V\left(\frac{L}{2}\right) \tag{6-24}$$

The impedance spectroscopy of the material system can be determined as,

$$Z^*(\omega) = \frac{2\left(\Delta\phi\left(\frac{L}{2},\omega\right) - \Delta\phi(0,\omega)\right)}{\Delta J_T(\omega)} \tag{6-25}$$

Here, the impedance is doubled as we only compute the impedance in half of the material system, indicated by the symmetric axis simplification.

6.4 NUMERICAL SOLUTION AND MODEL VALIDATION

There are 6 unknown variables in Equation (6-13), (6-14) and (6-15), the profiles of $\phi(x)$, $c_v(x)$ and $c_e(x)$ under steady state, as well as their perturbations, $\Delta\phi(x,\omega)$, $\Delta c_v(x,\omega)$ and $\Delta c_e(x,\omega)$. The profiles of $\phi(x)$, $c_v(x)$ and $c_e(x)$ are first obtained using steady state equations. The steady state solutions then are used to Equations (6-13), (6-14) and (6-15) to solve for the unknowns of three perturbations. Under a specified frequency, the profile of each perturbation is obtained by solving these three equations simultaneously. The impedance of the physical system is obtained according to Equation (6-25). The mathematical model is solved using commercial software package of

COMSOL Multiphysics 4.1a. The model parameters are listed in Table 6.1. The Partial Differential Equations (PDEs) with coefficient form are utilized for charge transport in MIEC and Poisson's equation. The computational domain is discretized and refined until the mesh-independent solution is obtained. The final computational domain mesh consists of 51020 elements. The solution of the discretized equation is implemented by COMSOL solver (MUMPS).

Model validation is an important step towards further high fidelity numerical analysis. Theoretically, the model predictions should be consistent with the experimental data over a wide range of operating conditions, including impedance responses and various parameter distributions. However, the distributions of the charged species and electric field cannot be easily obtained by present measurement techniques. In this study, the measurable impedance spectra are used to validate the model. The experimental data from open literature is first used to validate the model and determine the model parameters such as charge mobility and reaction rate constants for charged species. The model then is used to interpret the experimental data for the specimen under uniaxial loading.
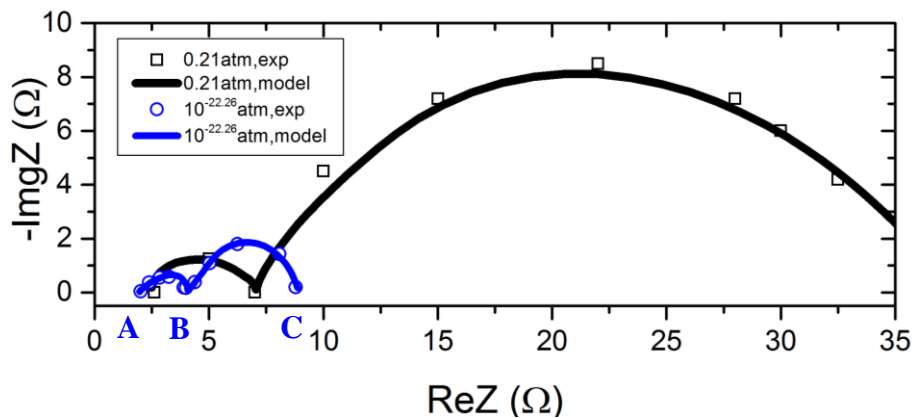
Figure 6.4 Validation of Impedance for polycrystalline mixed conductor under $600^{o}C$

Table 6.1 Physical parameters used in the model

Parameters	Lai's experimental data	In-house experimental data
Dimension of the specimen	Φ13.05mm$\times$L0.65mm	24.2mm$\times$4.8mm$\times$2mm
Dimensions of the computational domain, L	0.65mm	6.4 mm
Grain Size, D*	6 μm	4-6 μm
Width of space charge layer, λ_S*	0.38nm	0.3nm
Space charge potential Φ_0*, $\frac{\lambda_S{}^2 F c_a}{2\varepsilon_r \varepsilon_0}$	0.48V	0.38V
Dopant concentration, c_a [171]	6078mol/m^3	8104mol/m^3
Electron concentration, c_e	8(0.21atm)/84(10$^{-22.26}$atm)	Detailed in Table 6.2
Rate constant for vacancy, electron k_j*[171]	2.7$\times$10^{-15}/10^{10}(m/s)	2.7$\times$10^{-8}/10^8(m/s)
Ionic Mobility in SDC m$_v$ [170]	$\frac{1}{T} \cdot 10^{(2.31875 - 3.36932\times1000/T)}$ (cm^2/V·s)	
Electronic Mobility in SDC, m$_e$ [170]	$\frac{1}{T} \cdot 10^{(1.30343 - 1.34027\times1000/T)}$ (cm^2/V·s)	

The experimental data of $Sm_{0.15}Ce_{0.85}O_{1.925-\delta}$ (SDC15) from open literature Lai [184] was employed. In this experiment, the author measured the impedance spectra of a polycrystalline SDC pellet, with a diameter of 13mm and a thickness of 0.65mm, sandwiched by two identical patterned silver mesh current collectors. According to this experimental setup, we simulate the charge transport process and impedance response with consideration of 1-D situation in the thickness direction of the button cell. The grain size is assumed with 6nm and the space charge layer is assumed with 3.8 Å. Other parameters are shown in Table 6.1. The parameters denoted with "*" in Table 6.1 were adjustable so that the impedance curves predicted by the model can match with experimental results under identical operating conditions. The impedance spectra under 600°C with high oxygen partial pressure 0.21atm and low oxygen partial pressure 10$^{-22.26}$atm were validated respectively. As shown in Figure 6.4, the simulation results are

consistent with the experimental data. This model is then used for further investigation of material system under different operating conditions.

6.5 RESULTS AND DISCUSSIONS

In the following sections, the impedance spectra are studied by the equivalent circuit of the system, which can guide the parameter selection and improve the efficiency of the fitting process. Then, the impedance spectra were interpreted for the SDC20 specimen under stress-free and stressed conditions. The transport mechanisms of the SDC20 under mechanical stress were discussed.

6.5.1 Impedance Study

The impedance of the system was calculated according to Equation (6-25). The impedance curve then was obtained by specifying a series of frequencies and calculating the corresponding impedance. There are two subcircuits shown in the impedance curves of Figure 6.4. The "high-frequency subcircuit" only includes the contributions of the electrolyte components and thus can be characterized as "electrolyte subcircuit". Theoretically there should be two subcircuts if the space charge regions exist at the grain boundaries. However, due to the fact that the capacitance of the grain interior is much smaller than that of the space charge layer, the one closer to the origin contributed from the grain interior is out of the frequency range we tested. So, the high-frequency subcircuit shown in the figure is contributed from the space charge layer and called the grain boundary arc. The "low-frequency subcircuit" in the figure includes contributions from both the electrolyte and electrode components. Under high oxygen partial pressures, it is typically a semicircular arc displaced from the origin and can be described as the electrode arc since the electrolyte components only contribute a displacement from the

origin, as indicated by the black line in Figure 6.4. Under low oxygen partial pressures, it will give a half-tear-drop (Warburg) arc displaced from the origin, as shown by the blue line in Figure 6.4.
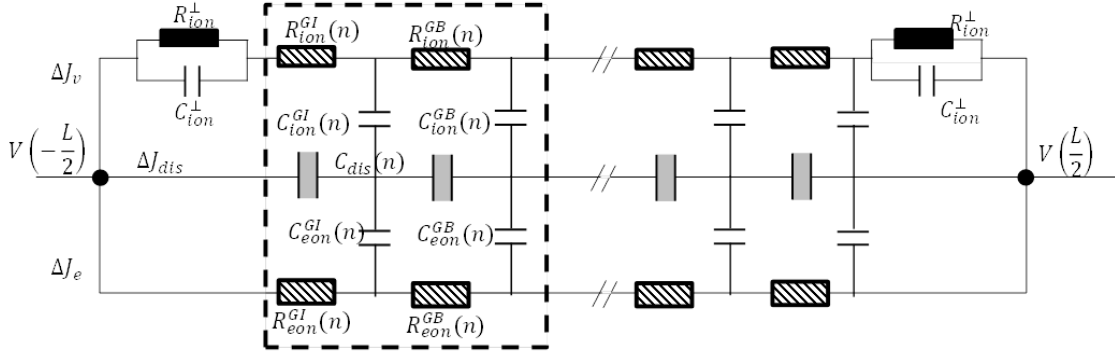
Figure 6.5 A.C. equivalent circuit for polycrystalline mixed conductor

The equivalent circuit of the material system is shown in Figure 6.5. Here, GI represents grain interior; GB is grain boundary. This circuit has been discussed in the literature for a mixed conductor [168, 170]. It is worth to further discuss the impedance at certain ranges of frequency limits and their corresponding physical characteristics. We separate the whole circuit into two subcircuits, a "low-frequency subcircuit" and a "high-frequency subcircuit". Then, there will be three intercepts, shown in Figure 6.4, including: D.C. limit (C), low-frequency limit (B) and high frequency limit (A).

At the D.C. limit ($\omega \to 0$), all the capacitors are effectively open, the impedance of this circuit is :

$$Z_0 = \left(\frac{1}{R_{ion}+2R_{ion}^\perp} + \frac{1}{R_{eon}}\right)^{-1} \text{ with } R_i = \sum_n R_i^{GI}(n) + R_i^{GB}(n) \qquad (6\text{-}26)$$

At high frequencies, both the capacitors $C_{ion}^\perp$ and $C_i^{GB}(n)$ are effectively shorted. The resistors $R_{ion}^{GI}(n)$ and $R_{eon}^{GI}(n)$ of grain interior are in parallel and can be combined into a single resistor,

126

$$Z_{high} = \left(\frac{1}{R_{ion}^{GI}} + \frac{1}{R_{eon}^{GI}}\right)^{-1} \text{ with } R_i^{GI} = \sum_n R_i^{GI}(n) \tag{6-27}$$

From the above analysis, we can obtain that the intercept A close to the origin of the blue line in Figure 6.4 is determined by the ionic and electronic resistance in the grain interior from Equation (6-27). The intercept C is determined by the ionic resistance, electronic resistance in both grains and grain boundaries, and interface resistance for oxygen vacancy at the electrodes, indicated by Equation (6-26). These two equations can provide more guidelines in the fitting process.

6.5.2 Parameter selection in the fitting process

There are 11 independent unknown variables in the model, which include grain size D, the width of space charge layer, λ_S, dopant concentration, c_a, electron concentration, c_e, rate constant for vacancy and electron k_j, ionic and electronic mobility in SDC m_j, parameters C_i and α in CPE, equivalent cross area A. By fitting the predictions of our mode to Lai's experimental data in section 6.4, we obtain the ionic and electronic mobility in SDC15 material, which is consistent with the numerical expression listed in Table 6.1 from Lai. Due to the fact that SDC15 and SDC20 are produced from ceria oxide doped by different amount of samarium element, the ionic and electronic motilities under the same temperature should be the same for the two materials. The dopant concentration in SDC20 can be specified according to the dopant magnitude in SDC15 by linear interpolation. The grain size is estimated about 4-6μm based on the TEM images of the specimen. The reaction rate constant for electron is generally large, and can hardly affect the impedance compared to other unknown variables. Then, the unknown variables are reduced to 6.

In Table 6.1, we can find that there is a big difference of the reaction rate for oxygen vacancy between Lai's data and our data. This is closely related to the different experimental setup. In Lai's experiment, the oxygen reduction reaction occurs at the surface of the pellet, where the silver meshes are painted; whereas for our in-house prepared SDC specimen, the electrochemical reaction takes place in the adjacent area where the silver wires are bound, as shown in Figure 6.2. In addition, from the experimental setup in Figure 6.2, it is difficult to determine the equivalent cross area, as the current is collected by the silver wires bound on the surface of the plate. Then, it is treated as an unknown variable in the fitting process.

At the high frequency limit, from Equation (6-27), the impedance is determined by the ionic and electronic resistance in the grain interiors. The ionic and electronic mobility are already specified through the validation process. Assuming electron concentration, c_e, the equivalent cross area A is adjusted to match Z_{high} of the experimental data. As the high-frequency (electrolyte) subcircuit represents the impedance of the space charge layer, the width of space charge layer, λ_S, is a critical unknown variable to determine the shape of the subcircuit. So, in the fitting process, we fitted the high-frequency subcircuit first by varying c_e and λ_S, with A satisfying Equation (6-27). After the first subcircuit is perfectly matched with the experimental data, the low-frequency subcircuit is fitted by changing the rate constant for vacancy k_v, and parameters of C_i, α in CPE, which are the three important parameters to determine the shape and location of the low-frequency subcircuit, as indicated in Equation (6-26).

6.5.3 Interpretation of impedance spectra under mechanical stress

It is generally recognized that the migration of the oxygen ions in the grain interior can be accelerated by mechanical strain excitation. However, under practical condition, the mixed conductor usually has a polycrystalline structure with not only grain interiors but also grain boundaries. In practical applications, the bulk ceramic materials are subjected to mechanical stress induced by either thermal, chemical or sintering effects. The impedance responses of the specimen under stress-free and stressed conditions were measured respectively in atmosphere under different temperatures. Then, the mathematical model predictions are fitted to the experimental impedance curves. Accordingly the experimental data is interpreted.
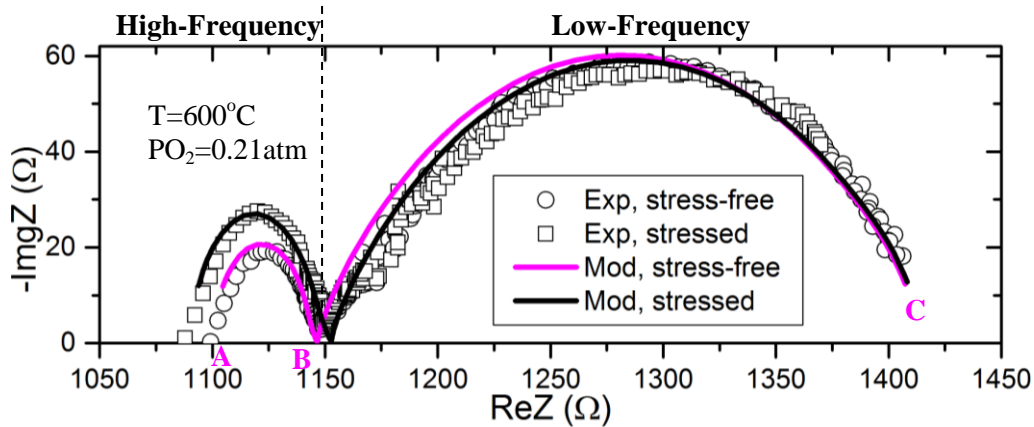
Figure 6.6 Interpretation of Impedance spectra for SDC plate under $600^{\circ}C$

The temperature of specimen is controlled at $600^{\circ}C$, $550^{\circ}C$ and $500^{\circ}C$ respectively. A 0.7MPa uniaxial tensile stress is applied to the specimen. And three set of impedance curves are obtained and shown in Figure 6.6, Figure 6.7 and 6.8.

In Figure 6.6, by comparing the stress-free case to the stressed case, one can find that the major difference occurs at the high-frequency subcircuit: the intercept close to the origin of the high-frequency subcircuit (A) moves to the left side and the other one (B) is hardly changed; the equivalent radius of the subcircuit increases when the external

load is applied on the specimen. After fitting the experimental curves, the physical parameters are obtained from the model, which are listed in Table 6.2.

Table 6.2 List of the physical parameters in the fitting process

Parameter/Case	600°C stress-free (stressed)	550°C stress-free (stressed)	500°C stress-free (stressed)
Ionic Mobility in SDC, m_v, $(m^2 \cdot mol/(J \cdot s))$	*1.71×10^{-14} (×1.01)*	*1.026×10^{-14} (×1.03)*	*6.12×10^{-15} (×1.05)*
Electronic Mobility in SDC, m_e, $(m^2 \cdot mol/(J \cdot s))$	6.965×10^{-13}	5.96×10^{-13}	4.98×10^{-13}
Reaction rate constant for vacancy, k_v, (m/s)	*1.5×10^{-7} (/1.08)*	*7.143×10^{-9} (/1.2)*	*3.597×10^{-9} (/14)*
Width of space charge layer, λ_S, (m)	*2.69×10^{-10} (×1.02)*	*3.045×10^{-10} (×1.002)*	*3.14×10^{-10} (×1.01)*
Electron concentration, c_e, (mol/m^3)	28	400	220
Cross Area, A,(m^2)	2.227×10^{-6}	1.587×10^{-6}	1.975×10^{-6}
Parameter in CPE, C_i, (F$^\alpha$)	6.5×10^{-8}	5×10^{-8}	5×10^{-7}
Coefficient in CPE, α	0.52	0.35	0.5

Italic texts represent the physical parameter variations from stress-free to stressed condition.

We can see that from stress-free condition to stressed condition, ionic mobility, width of space charge layer and reaction rate constant for oxygen vacancy have been changed. The ionic conductivity increases by 1%, which contributes to the movement of the intercept close to the origin (A); the width of the space charge layer has been stretched by 2%, which leads to the increase of the equivalent radius of the high-frequency subcircuit, and push the intercept towards to the right side due to the enhancement of ionic conductivity. In addition, the low-frequency subcircuit is affected by the variation of ionic conductivity as well, and its effect is canceled out by the change of the oxygen vacancy reaction rate constant. Therefore, the impedance variations introduced by mechanical stress indicate that under stressed state, mechanical stress can increase the ionic conductivity and stretch the space charge layer. As a result, the

impedance resistance of the grain interior is reduced due to the increase of ionic conductivity.
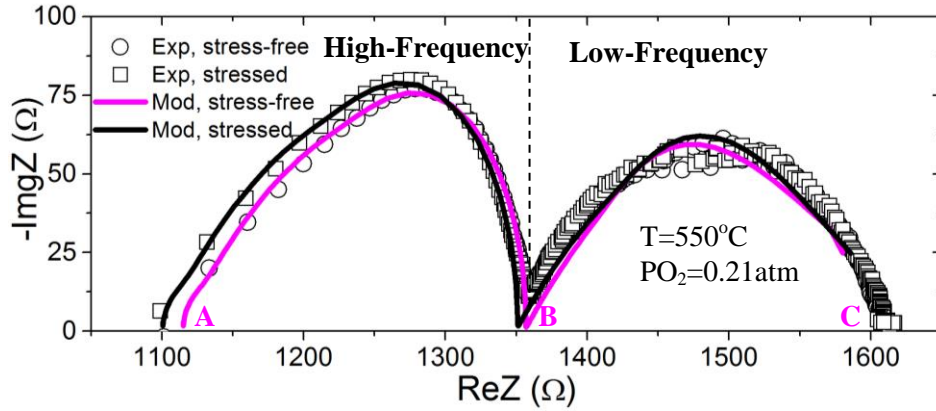
Figure 6.7 Interpretation of Impedance spectra for SDC plate under 550°C
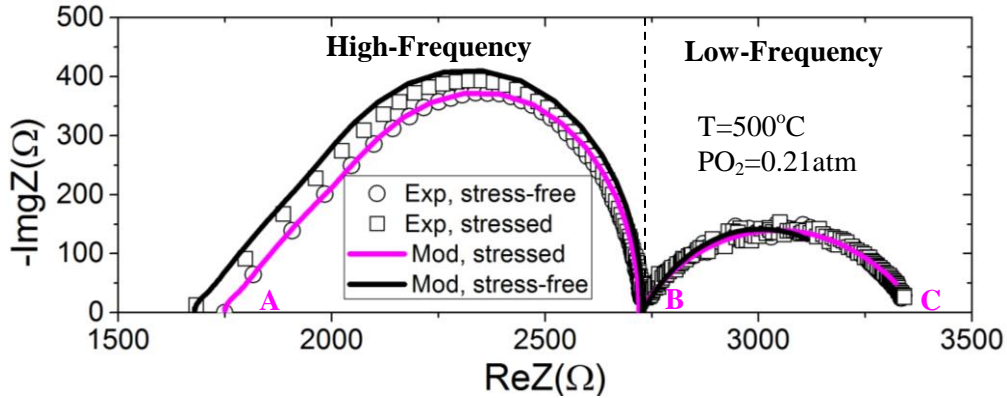
Figure 6.8 Interpretation of Impedance spectra for SDC plate under 500°C

Similarly, under 550°C and 500°C, as shown in Figure 6.7 and 6.8 respectively, the intercept close to the origin (A) shifts towards the left side and the equivalent radius of the high-frequency subcircuit increases as well. However, the intercept left-shift is much significant compared to the radius increase. Correspondingly from Table 6.2, we find that, under 550°C the ionic mobility is increased by 3%, however the width of space charge layer is only increased by 0.2%; under 500°C, the ionic mobility is enlarged by 5%, and the width of space charge layer is increased by 1%. At the same time, the oxygen vacancy reaction rates in both cases decrease.

Comparing to the impedance spectra under 600$^\text{o}$C, 550$^\text{o}$C and 500$^\text{o}$C in Figure 6.6, 6.7 and 6.8, as well as the corresponding parameters in Table 6.2, there are three distinct features of the impedance evolution with respect to temperatures. Firstly, as the temperature decreases from 600$^\text{o}$C to 500$^\text{o}$C, the high-frequency subcircuits expand while the low-frequency subcircuits shrink. This is because the resistance of the high-frequency (grain boundary) subcircuit is closely related to the ionic mobility of the material, which varies exponentially as a function of temperature. When temperature decreases, the ionic mobility decreases dramatically. Secondly, under higher temperature 600$^\text{o}$C and stressed condition, the deformation of the space charge layer is larger than that under lower temperature 500$^\text{o}$C.

In conclusion, by applying external tensile load on the mixed ionic and electronic conductor, the ionic conductivity of the material is increased, and the space charge layer is stretched. According to solid mechanics investigation, the mechanical strength of the bulk material is generally much higher than that of the grain boundary. Therefore, when the bulk ceramic is subjected to stress, the grain is hardly deformed. However, the mechanical stress can improve the migration of oxygen ions, leading to the resistance decrease of the grain interior. Meanwhile the major deformation occurs in the grain boundary, and the resistance of the grain boundary is increased.

6.5.4 Limitations of the analysis

Even though the experimental and fitted impedance spectra in Figure 6.6 , 6.7 and 6.8 are generally consistent, there are still some differences. First, under 600$^\text{o}$C, the fitted curve does not intercept with x axis at high-frequency side. Second, there appears to be some mismatch at the low-frequency region of the semicircular arc in all cases.

There are several possible reasons causing the deviations. Firstly, we proposed a one-dimension model. Secondly, the current is only collected by the silver wire bound on the surface of the SDC specimen, so the cross section area is difficult to determine. In our model, it is deduced by $R = \rho \frac{L}{A}$. Thirdly, for simplicity, both the grains and grain boundaries are assumed to be uniformly distributed throughout the entire computational domain. However in practical SDC, some distribution might exist. Finally, the inductive effect is not considered in our model.

6.6 CONCLUSIONS

In this research, we applied the continuum model with the space charge layer to simulate the impedance response of the mixed conductor SDC specimen under mechanical stress. The model was fitted to the experimental data, and the physical property variations under applied loads are interpreted. It indicates that by applying tensile load on the mixed ionic and electronic conductor, the ionic conductivity of the material is increased, and the space charge layer is stretched. The overall resistance of the ceramic maintains constant by the combined effects. In addition, as temperature increases, the increase of the width of the space charge layer is more significant; the increase of ionic mobility becomes less apparent.

CHAPTER 7

SUMMARY AND FUTURE PLAN

7.1 SUMMARY

In this research, innovative models of SOFCs were developed to study the chemical-mechanical coupling phenomena subjected to the effects of complicated multi-physicochemical processes. The structural reliability due to chemical stress was evaluated and correlated to different operating conditions of SOFCs. In addition, the effect of mechanical stress on electrical properties of MIEC was investigated by impedance spectra.

The defect transport process in conducting ceramics and non-stoichiometric conditions are closely related to the multi-physicochemical processes in SOFC devices. In chapter 2, a 2D transient mathematical model is developed for regenerative solid oxide cells. The model is employed to investigate complicated multi-physics processes during the transient process of mode switching. Simulation results indicate that the trends of internal parameter distributions, including $H_2/O_2/H_2O$ and ionic potentials, flip when the operating cell is switched from SOFC mode to SOEC mode. However, the electronic potential shows different behaviors. At H_2 electrode, electronic potential keeps at zero voltage level, while at O_2 electrode, electronic potential increases from a relatively low level in SOFC mode to a relatively high level in SOEC mode. Transient results also show that an overshoot occurs for mass fraction distribution of water vapor at H_2 side when the operating cell switches from SOFC mode to SOEC mode. The mass fractions of O_2 and

H_2 as well as charge potentials (electronic and ionic) may quickly follow the operating mode changes. The simulation results presented facilitate the internal mechanism understanding for regenerative SOFCs.

Due to degradations, the electrode layer of SOECs might be detached from the electrolyte layer, leading to delamination phenomenon. While this phenomenon is observed in post-test stacks, quantitative understanding of delamination effects may facilitate to evaluate SOEC performance tolerance on such failures. In chapter 3, the 2D CFD model in chapter 2 is applied in SOEC mode to investigate the sensitivity of electrolysis performance to deliminations occurred at oxygen electrode/electrolyte interface. Results indicate that delaminations significantly influence local charge current density distributions since the charge transport path is cutoff. In both parallel flow and counter flow settings, electrolysis performance is more sensitive to the delamination occurred at the center of the cell than those occurred at the edges of the cell.

To better understand the mechanical failure of delamination at cathode/electrolyte interface, in chapter 4, a micro model is developed to study the cathode/electrolyte interfacial stresses. The model considers the complicated interactions between structural mechanics and ionic transport process through conductive defects. While both the chemical and thermal stresses are complicated at the interface, the chemical stresses show different distribution patterns from the thermal stresses. The results of combined thermal and chemical stresses show that these two kinds of stresses can be partially canceled out with each other, leading to the reduced overall stresses at the cathode/electrolyte interface. The distributions of oxygen partial pressure and thus the oxygen vacancy

concentration on the cathode particle surface have significant effects on chemical stress distribution and consequently on the principal stresses at the cathode/electrolyte interface.

In chapter 5, a comprehensive model is developed to study chemical-mechanical coupling phenomenon in an anode-supported SOFC button cell. The model for the first time links oxygen ionic transport process with chemical stress generated in the PEN structure assembly of a button cell under multi-physicochemical operating conditions. This is an important module complementary to the state-of-the-art electrochemical-thermal-mechanical modeling of SOFCs. The model is partially validated using the measured polarization performance, upon which systematic simulations are carried out. Results show that multi-physicochemical operating conditions lead to non-uniform distribution of oxygen vacancy site fraction in the PEN assembly. Different oxygen vacancy concentration causes different volumetric expansion of bulk material. Therefore chemical stress occurs in PEN assembly. The chemical stress distribution is also strongly dependent on mechanical constraints applied on the cell. Without mechanical constraint, the peak value of the first principal stress occurs within the anode electrode and at the anode/electrolyte interface; the third principal stress shows a peak value at the cathode/electrolyte interface. The chemical stress particularly the peak values of the first and third principal stress can be mitigated by increasing the cell operating voltage (i.e. decreasing cell current). The hydrogen molar fraction in the fuel shows slight effect on chemical stress. The porosity of electrodes shows significant effects on chemical stress. Bigger porosity can significantly decrease the extremes of first and second principal stresses in PEN assembly. The effect of electrode tortuosity is negligible on chemical stress. Larger anode thickness in the anode-supported SOFCs increases the chemical

stress in the anode electrode but favors decreasing the chemical stress in electrolyte and cathode domain. The Weibull analysis shows that high cell operating voltage and low hydrogen content in the fuel may mitigate failure probability of PEN assembly. With relatively low electrode porosity, the anode electrode is a vulnerable component in the anode-supported button cell; with relatively high electrode porosity, the electrolyte and cathode layer become vulnerable components. Large anode thickness can mitigate failure probability of electrolyte and cathode layer but increase anode failure probability. The failure probability is not sensitive to the thickness variations of electrolyte and cathode layers. Relatively thinner anode and cathode, and thicker electrolyte as well as high operating cell voltage can reduce the elastic energy stored in the cathode layer and therefore mitigate the probability of delamination failure at the cathode/electrolyte interface in anode-supported SOFCs.

In chapter 6, we applied the continuum model with the space charge layer to simulate the impedance response of the mixed conductor SDC plate under mechanical stress. The model was fitted to the experimental data, and the physical property variations because of applied loads are interpreted. It indicates that by applying tensile load on the mixed ionic and electronic conductor, the ionic conductivity of the material will be increased, and the space charge layer will be stretched. The overall resistance of the ceramic maintains constant by the combined effects. In other words, to be benefited from the mechanical stress one has to avoid or minimize the grain boundary deformation.

7.2 OUTLOOK

In this dissertation, the multi-physicochemical models of SOFCs was built to study multi-physics transport processes and related chemical and thermal stresses as well

as reliability analysis. The model validation is critical step for further high fidelity numerical analysis. It is still a challenge issue on how to comprehensively validate the multi-physicochemical model coupled with mechanical stress. In this respect, more experiments are needed to identify the oxygen vacancy distribution and the deformations of solid oxide fuel cell under operating condition. Furthermore, chemical stress generated in the transient processes, such as system startup, shutdown and load fluctuation, need to be investigated further.

REFERENCES

1. Birgersson, K.E., et al., *Energy Solutions for a Sustainable World.* Applied Energy, 2012. **90**(1): p. 1-2.
2. Turner, J.A., *A realizable renewable energy future.* Science, 1999. **285**(5428): p. 687-689.
3. Shafiee, S. and E. Topal, *When will fossil fuel reserves be diminished?* Energy Policy, 2009. **37**(1): p. 181-189.
4. Cox, P.M., et al., *Acceleration of global warming due to carbon-cycle feedbacks in a coupled climate model (vol 408, pg 184, 2000).* Nature, 2000. **408**(6813): p. 750-750.
5. Solomon, S., et al., *Irreversible climate change due to carbon dioxide emissions.* Proceedings of the National Academy of Sciences of the United States of America, 2009. **106**(6): p. 1704-1709.
6. Lashof, D.A. and D.R. Ahuja, *Relative Contributions of Greenhouse Gas Emissions to Global Warming.* Nature, 1990. **344**(6266): p. 529-531.
7. Steele, B.C.H., *Fuel-cell technology - Running on natural gas.* Nature, 1999. **400**(6745): p. 619-+.
8. Acres, G.J.K., *Recent advances in fuel cell technology and its applications.* Journal of Power Sources, 2001. **100**(1-2): p. 60-66.
9. Roziere, J. and D.J. Jones, *Non-fluorinated polymer materials for proton exchange membrane fuel cells.* Annual Review of Materials Research, 2003. **33**: p. 503-555.
10. Ralph, T.R., et al., *Low cost electrodes for proton exchange membrane fuel cells - Performance in single cells and Ballard stacks.* Journal of the Electrochemical Society, 1997. **144**(11): p. 3845-3857.
11. Oetjen, H.F., et al., *Performance data of a proton exchange membrane fuel cell using H-2/CO as fuel gas.* Journal of the Electrochemical Society, 1996. **143**(12): p. 3838-3842.
12. Singhal, S.C., *Advances in solid oxide fuel cell technology.* Solid State Ionics, 2000. **135**(1-4): p. 305-313.
13. Yamamoto, O., *Solid oxide fuel cells: fundamental aspects and prospects.* Electrochimica Acta, 2000. **45**(15-16): p. 2423-2435.
14. Park, S.D., J.M. Vohs, and R.J. Gorte, *Direct oxidation of hydrocarbons in a solid-oxide fuel cell.* Nature, 2000. **404**(6775): p. 265-267.
15. McLean, G.F., et al., *An assessment of alkaline fuel cell technology.* International Journal of Hydrogen Energy, 2002. **27**(5): p. 507-526.
16. Varcoe, J.R. and R.C.T. Slade, *Prospects for alkaline anion-exchange membranes in low temperature fuel cells.* Fuel Cells, 2005. **5**(2): p. 187-200.

17. Cavallaro, S., N. Mondello, and S. Freni, *Hydrogen produced from ethanol for internal reforming molten carbonate fuel cell.* Journal of Power Sources, 2001. **102**(1-2): p. 198-204.

18. Cherepy, N.J., et al., *Direct conversion of carbon fuels in a molten carbonate fuel cell.* Journal of the Electrochemical Society, 2005. **152**(1): p. A80-A87.

19. Stonehart, P., *Development of Alloy Electrocatalysts for Phosphoric-Acid Fuel-Cells (Pafc).* Journal of Applied Electrochemistry, 1992. **22**(11): p. 995-1001.

20. Li, Q.F., H.A. Hjuler, and N.J. Bjerrum, *Phosphoric acid doped polybenzimidazole membranes: Physiochemical characterization and fuel cell applications.* Journal of Applied Electrochemistry, 2001. **31**(7): p. 773-779.

21. Wasmus, S. and A. Kuver, *Methanol oxidation and direct methanol fuel cells: a selective review.* Journal of Electroanalytical Chemistry, 1999. **461**(1-2): p. 14-31.

22. Hamnett, A., *Mechanism and electrocatalysis in the direct methanol fuel cell.* Catalysis Today, 1997. **38**(4): p. 445-457.

23. Sato, K., et al., *Fracture process of nonstoichiometric oxide based solid oxide fuel cell under oxidizing/reducing gradient conditions.* Journal of Power Sources, 2010. **195**(17): p. 5481-5486.

24. Koch, S., et al., *Solid oxide fuel cell performance under severe operating conditions.* Fuel Cells, 2006. **6**(2): p. 130-136.

25. Young, J.L. and V.I. Birss, *Crack severity in relation to non-homogeneous Ni oxidation in anode-supported solid oxide fuel cells.* Journal of Power Sources, 2011. **196**(17): p. 7126-7135.

26. Chen, K.F. and S.P. Jiang, *Failure mechanism of (La,Sr)MnO3 oxygen electrodes of solid oxide electrolysis cells.* International Journal of Hydrogen Energy, 2011. **36**(17): p. 10541-10549.

27. Badwal, S.P.S., *Stability of solid oxide fuel cell components.* Solid State Ionics, 2001. **143**(1): p. 39-46.

28. Scott, H.G., *Phase Relationships in Zirconia-Yttria System.* Journal of Materials Science, 1975. **10**(9): p. 1527-1535.

29. Badwal, S.P.S., F.T. Ciacchi, and V. Zelizko, *The Effect of Alumina Addition on the Conductivity, Microstructure and Mechanical Strength of Zirconia - Yttria Electrolytes.* Ionics, 1998. **4**(1-2): p. 25-32.

30. Minh, N.Q., *Ceramic Fuel-Cells.* Journal of the American Ceramic Society, 1993. **76**(3): p. 563-588.

31. Millichamp, J., et al., *A study of carbon deposition on solid oxide fuel cell anodes using electrochemical impedance spectroscopy in combination with a high temperature crystal microbalance.* Journal of Power Sources, 2013. **235**: p. 14-19.

32. Kuhn, J.N., N. Lakshminarayanan, and U.S. Ozkan, *Effect of hydrogen sulfide on the catalytic activity of Ni-YSZ cermets.* Journal of Molecular Catalysis a-Chemical, 2008. **282**(1-2): p. 9-21.

33. Dong, J., et al., *Identification of nickel sulfides on Ni-YSZ cermet exposed to H-2 fuel containing H2S using Raman spectroscopy.* Journal of Power Sources, 2006. **156**(2): p. 461-465.

34. Yokokawa, H., *Understanding materials compatibility.* Annual Review of Materials Research, 2003. **33**: p. 581-610.

35. Mitterdorfer, A. and L.J. Gauckler, *La2Zr2O7 formation and oxygen reduction kinetics of the La0.85Sr0.15MnyO3, O-2(g)vertical bar YSZ system.* Solid State Ionics, 1998. **111**(3-4): p. 185-218.

36. N. Q. Mihn, T.T., *Science and Technology of Ceramic Fuel Cells.* 1995, Amsterdam: Elsevier.

37. Chen, M., et al., *Thermodynamic modeling of the La-Mn-Y-Zr-O system.* Calphad-Computer Coupling of Phase Diagrams and Thermochemistry, 2006. **30**(4): p. 489-500.

38. Sarantaridis, D. and A. Atkinson, *Redox cycling of Ni-based solid oxide fuel cell anodes: A review.* Fuel Cells, 2007. **7**(3): p. 246-258.

39. Klemenso, T., C.C. Appel, and M. Mogensen, *In situ observations of microstructural changes in SOFC anodes during redox cycling.* Electrochemical and Solid State Letters, 2006. **9**(9): p. A403-A407.

40. Klemenso, T., et al., *The mechanism behind redox instability of anodes in high-temperature SOFCs.* Journal of the Electrochemical Society, 2005. **152**(11): p. A2186-A2192.

41. Waldbillig, D., A. Wood, and D.G. Ivey, *Thermal analysis of the cyclic reduction and oxidation behaviour of SOFC anodes.* Solid State Ionics, 2005. **176**(9-10): p. 847-859.

42. Waldbillig, D., A. Wood, and D.G. Ivey, *Electrochemical and microstructural characterization of the redox tolerance of solid oxide fuel cell anodes.* Journal of Power Sources, 2005. **145**(2): p. 206-215.

43. Malzbender, J., E. Wessel, and R.W. Steinbrech, *Reduction and re-oxidation of anodes for solid oxide fuel cells.* Solid State Ionics, 2005. **176**(29-30): p. 2201-2203.

44. Zhang, Y., et al., *Redox cycling of Ni-YSZ anode investigated by TPR technique.* Solid State Ionics, 2005. **176**(29-30): p. 2193-2199.

45. Fouquet, D., et al., *Kinetics of oxidation and reduction of Ni/YSZ cermets.* Ionics, 2003. **9**(1-2): p. 103-108.

46. Wood, A., et al., *Initial testing of solutions to redox problems with anode-supported SOFC.* Journal of the Electrochemical Society, 2006. **153**(10): p. A1929-A1934.

47. Pihlatie, M., et al., *Dimensional Behavior of Ni-YSZ Composites during Redox Cycling.* Journal of the Electrochemical Society, 2009. **156**(3): p. B322-B329.

48. Chen, H.Y., et al., *Simulation of coarsening in three-phase solid oxide fuel cell anodes.* Journal of Power Sources, 2011. **196**(3): p. 1333-1337.

49. Yokokawa, H., et al., *Fundamental mechanisms limiting solid oxide fuel cell durability.* Journal of Power Sources, 2008. **182**(2): p. 400-412.

50. Anandakumar, G., et al., *Thermal stress and probability of failure analyses of functionally graded solid oxide fuel cells.* Journal of Power Sources, 2010. **195**(19): p. 6659-6670.

51. Serincan, M.F., U. Pasaogullari, and N.M. Sammes, *Thermal stresses in an operating micro-tubular solid oxide fuel cell.* Journal of Power Sources, 2010. **195**(15): p. 4905-4914.

52. Huang, K. and H.D. Harter, *Temperature-dependent residual stresses in plasma sprayed electrolyte thin-film on the cathode substrate of a solid oxide fuel cell.* Solid State Ionics, 2010. **181**(19-20): p. 943-946.

53. Jiang, T.L. and M.H. Chen, *Thermal-stress analyses of an operating planar solid oxide fuel cell with the bonded compliant seal design.* International Journal of Hydrogen Energy, 2009. **34**(19): p. 8223-8234.

54. Liu, L., G.Y. Kim, and A. Chandra, *Modeling of thermal stresses and lifetime prediction of planar solid oxide fuel cell under thermal cycling conditions.* Journal of Power Sources, 2010. **195**(8): p. 2310-2318.

55. Selimovic, A., et al., *Steady state and transient thermal stress analysis in planar solid oxide fuel cells.* Journal of Power Sources, 2005. **145**(2): p. 463-469.

56. Inaba, H. and H. Tagawa, *Ceria-based solid electrolytes - Review.* Solid State Ionics, 1996. **83**(1-2): p. 1-16.

57. Mogensen, M., N.M. Sammes, and G.A. Tompsett, *Physical, chemical and electrochemical properties of pure and doped ceria.* Solid State Ionics, 2000. **129**(1-4): p. 63-94.

58. Panlener, R.J., R.N. Blumenthal, and J.E. Garnier, *Thermodynamic Study of Nonstoichiometric Cerium Dioxide.* Journal of Physics and Chemistry of Solids, 1975. **36**(11): p. 1213-1222.

59. Wang, S.R., et al., *Nonstoichiometry of Ce0.9Gd0.1O1.95-x.* Solid State Ionics, 1998. **107**(1-2): p. 73-79.

60. Otake, T., et al., *Nonstoichiometry of Ce1-xYxO2-0.5x-delta (X=0.1, 0.2).* Solid State Ionics, 2003. **161**(1-2): p. 181-186.

61. Yashiro, K., et al., *Mass transport properties of Ce0.9Gd0.1O2-delta at the surface and in the bulk.* Solid State Ionics, 2002. **152**: p. 469-476.

62. Adler, S.B., *Chemical expansivity of electrochemical ceramics.* Journal of the American Ceramic Society, 2001. **84**(9): p. 2117-2119.

63. Atkinson, A. and T.M.G.M. Ramos, *Chemically-induced stresses in ceramic oxygen ion-conducting membranes.* Solid State Ionics, 2000. **129**(1-4): p. 259-269.

64. Vaidya, S. and J.H. Kim, *Finite element thermal stress analysis of solid oxide fuel cell cathode microstructures.* Journal of Power Sources, 2013. **225**: p. 269-276.

65. Clague, R., A.J. Marquis, and N.P. Brandon, *Finite element and analytical stress analysis of a solid oxide fuel cell.* Journal of Power Sources, 2012. **210**: p. 224-232.

66. Peksen, M., et al., *3D transient thermomechanical behaviour of a full scale SOFC short stack.* International Journal of Hydrogen Energy, 2013. **38**(10): p. 4099-4107.

67. Khaleel, M.A., et al., *A finite element analysis modeling tool for solid oxide fuel cell development: coupled electrochemistry, thermal and flow analysis in MARC((R)).* Journal of Power Sources, 2004. **130**(1-2): p. 136-148.

68. Bishop, S.R., K.L. Duncan, and E.D. Wachsman, *Defect equilibria and chemical expansion in non-stoichiometric undoped and gadolinium-doped cerium oxide.* Electrochimica Acta, 2009. **54**(5): p. 1436-1443.

69. Duncan, K.L., et al., *The role of point defects in the physical properties of nonstoichiometric ceria.* Journal of Applied Physics, 2007. **101**(4): p. 044906.

70. Duncan, K.L., et al., *Role of Point Defects in the Physical Properties of Fluorite Oxides.* Journal of the American Ceramic Society, 2006. **89**(10): p. 3162-3166.

71. S. R. Bishop, K.L.D., and E. D. Wachsman, *THERMO-CHEMICAL EXPANSION OF SOFC MATERIALS.* ECS Transactions, 2006. **1**(7): p. 13-21.

72. Wang, S.R., et al., *Expansion behavior of Ce1-yGdyO2.0-0.5y-delta under various oxygen partial pressures evaluated by HTXRD.* Journal of the Electrochemical Society, 2003. **150**(7): p. A952-A958.

73. Yakabe, H., M. Hishinuma, and I. Yasuda, *Static and transient model analysis on expansion behavior of LaCrO3 under an oxygen potential gradient.* Journal of the Electrochemical Society, 2000. **147**(11): p. 4071-4077.

74. Atkinson, A., *Chemically-induced stresses in gadolinium-doped ceria solid oxide fuel cell electrolytes.* Solid State Ionics, 1997. **95**(3-4): p. 249-258.

75. Krishnamurthy, R. and B.W. Sheldon, *Stresses due to oxygen potential gradients in non-stoichiometric oxides.* Acta Materialia, 2004. **52**(7): p. 1807-1822.

76. Swaminathan, N. and J. Qu, *Interactions between non-stoichiometric stresses and defect transport in a tubular electrolyte.* Fuel Cells, 2007. **7**(6): p. 453-462.

77. Swaminathan, N., J. Qu, and Y. Sun, *An electrochemomechanical theory of defects in ionic solids. I. Theory.* Philosophical Magazine, 2007. **87**(11): p. 1705-1721.

78. Swaminathan, N., J. Qu, and Y. Sun, *An electrochemomechanical theory of defects in ionic solids. Part II. Examples.* Philosophical Magazine, 2007. **87**(11): p. 1723-1742.

79. Terada, K., et al., *Multiscale simulation of electro-chemo-mechanical coupling behavior of PEN structure under SOFC operation.* ECS Transactions 2011. **35**: p. 923-933.

80. Stambouli, A.B. and E. Traversa, *Solid oxide fuel cells (SOFCs): a review of an environmentally clean and efficient source of energy.* Renewable & Sustainable Energy Reviews, 2002. **6**(5): p. 433-455.

81. Shi, Y.X., N.S. Cai, and C. Li, *Numerical modeling of an anode-supported SOFC button cell considering anodic surface diffusion.* Journal of Power Sources, 2007. **164**(2): p. 639-648.

82. Serincan, M.F., U. Pasaogullari, and N.M. Sammes, *Computational thermal-fluid analysis of a microtubular solid oxide fuel cell.* Journal of the Electrochemical Society, 2008. **155**(11): p. B1117-B1127.

83. Jeon, D.H., *A comprehensive CFD model of anode-supported solid oxide fuel cells.* Electrochimica Acta, 2009. **54**(10): p. 2727-2736.

84. Hussain, M.M., X. Li, and I. Dincer, *Mathematical modeling of planar solid oxide fuel cells.* Journal of Power Sources, 2006. **161**(2): p. 1012-1022.

85. Yixiang Shi, N.C., Chen Li, Cheng Bao, Eric Croiset, Jiqin Qian, Qiang Hu, Shaorong Wang, *A General Approach for Electrochemical Impedance Spetroscopy Simulation Using Transient Mechanistic SOFC Model.* ECS Transactions, 2007. **7**(1): p. 1889-1899.

86. Chaisantikulwat, A., C. Diaz-Goano, and E.S. Meadows, *Dynamic modelling and control of planar anode-supported solid oxide fuel cell.* Computers & Chemical Engineering, 2008. **32**(10): p. 2365-2381.

87.   Qi, Y.T., B. Huang, and K.T. Chuang, *Dynamic modeling of solid oxide fuel cell: The effect of diffusion and inherent impedance.* Journal of Power Sources, 2005. **150**: p. 32-47.

88.   Zhang, X.W., et al., *Dynamic modeling of a hybrid system of the solid oxide fuel cell and recuperative gas turbine.* Journal of Power Sources, 2006. **163**(1): p. 523-531.

89.   Jiang, W., et al., *Parameter setting and analysis of a dynamic tubular SOFC model.* Journal of Power Sources, 2006. **162**(1): p. 316-326.

90.   Kang, Y.W., et al., *A reduced 1D dynamic model of a planar direct internal reforming solid oxide fuel cell for system research.* Journal of Power Sources, 2009. **188**(1): p. 170-176.

91.   Cheddie, D.F. and N.D.H. Munroe, *A dynamic 1D model of a solid oxide fuel cell for real time simulation.* Journal of Power Sources, 2007. **171**(2): p. 634-643.

92.   Li, J., et al., *Two-dimensional dynamic simulation of a direct internal reforming solid oxide fuel cell.* Journal of Power Sources, 2007. **171**(2): p. 585-600.

93.   Bhattacharyya, D., R. Rengaswamy, and C. Finnerty, *Dynamic modeling and validation studies of a tubular solid oxide fuel cell.* Chemical Engineering Science, 2009. **64**(9): p. 2158-2172.

94.   Udagawa, J., P. Aguiar, and N.P. Brandon, *Hydrogen production through steam electrolysis: Model-based dynamic behaviour of a cathode-supported intermediate temperature solid oxide electrolysis cell.* Journal of Power Sources, 2008. **180**(1): p. 46-55.

95.   Udagawa, J., P. Aguiar, and N.P. Brandon, *Hydrogen production through steam electrolysis: Control strategies for a cathode-supported intermediate temperature solid oxide electrolysis cell.* Journal of Power Sources, 2008. **180**(1): p. 354-364.

96.   Udagawa, J., P. Aguiar, and N.P. Brandon, *Hydrogen production through steam electrolysis: Model-based steady state performance of a cathode-supported intermediate temperature solid oxide electrolysis cell.* Journal of Power Sources, 2007. **166**(1): p. 127-136.

97.   Ni, M., M.K.H. Leung, and D.Y. Leung, *Theoretical analysis of reversible solid oxide fuel cell based on proton-conducting electrolyte.* Journal of Power Sources, 2008. **177**(2): p. 369-375.

98.   Ni, M., M.K.H. Leung, and D.Y.C. Leung, *Mathematical modeling of the coupled transport and electrochemical reactions in solid oxide steam electrolyzer for hydrogen production.* Electrochimica Acta, 2007. **52**(24): p. 6707-6718.

99.   Ni, M., M.K.H. Leung, and D.Y.C. Leung, *Electrochemical modeling of hydrogen production by proton-conducting solid oxide steam electrolyzer.* International Journal of Hydrogen Energy, 2008. **33**(15): p. 4040-4047.

100.   Ni, M., *Computational fluid dynamics modeling of a solid oxide electrolyzer cell for hydrogen production.* International Journal of Hydrogen Energy, 2009. **34**(18): p. 7795-7806.

101.   Winter, C.J., *Hydrogen energy - Abundant, efficient, clean: A debate over the energy-system-of-change.* International Journal of Hydrogen Energy, 2009. **34**(14): p. S1-S52.

102.   O'Brien, J.E., et al., *High-temperature electrolysis for large-scale hydrogen and syngas production from nuclear energy - summary of system simulation and*

economic analyses. International Journal of Hydrogen Energy, 2010. **35**(10): p. 4808-4819.

103. Gorensek, M.B. and C.W. Forsberg, *Relative economic incentives for hydrogen from nuclear, renewable, and fossil energy sources.* International Journal of Hydrogen Energy, 2009. **34**(9): p. 4237-4242.

104. Naterer, G.F., et al., *Synergistic roles of off-peak electrolysis and thermochemical production of hydrogen from nuclear energy in Canada.* International Journal of Hydrogen Energy, 2008. **33**(23): p. 6849-6857.

105. Naterer, G., et al., *Recent Canadian advances in nuclear-based hydrogen production and the thermochemical Cu-Cl cycle.* International Journal of Hydrogen Energy, 2009. **34**(7): p. 2901-2917.

106. Forsberg, C., *Futures for hydrogen produced using nuclear energy.* Progress in Nuclear Energy, 2005. **47**(1-4): p. 484-495.

107. Ni, M., M.K.H. Leung, and D.Y.C. Leung, *Parametric study of solid oxide steam electrolyzer for hydrogen production.* International Journal of Hydrogen Energy, 2007. **32**(13): p. 2305-2313.

108. Herring, J.S., et al., *Progress in high-temperature electrolysis for hydrogen production using planar SOFC technology.* International Journal of Hydrogen Energy, 2007. **32**(4): p. 440-450.

109. Hawkes, G., et al., *3D CFD model of a multi-cell high-temperature electrolysis stack.* International Journal of Hydrogen Energy, 2009. **34**(9): p. 4189-4197.

110. Mawdsley, J.R., et al., *Post-test evaluation of oxygen electrodes from solid oxide electrolysis stacks.* International Journal of Hydrogen Energy, 2009. **34**(9): p. 4198-4207.

111. Weber, A.Z. and J. Newman, *Modeling gas-phase flow in porous media.* International Communications in Heat and Mass Transfer, 2005. **32**(7): p. 855-860.

112. Weber, A., *Fuel Cells-Solid Oxide Fuel Cells | Life-Limiting Considerations*, in *Encyclopedia of Electrochemical Power Sources*. 2009. p. 120-134.

113. Park, K., et al., *Fast performance degradation of SOFC caused by cathode delamination in long-term testing.* International Journal of Hydrogen Energy, 2010. **35**(16): p. 8670-8677.

114. Virkar, A.V., *Mechanism of oxygen electrode delamination in solid oxide electrolyzer cells.* International Journal of Hydrogen Energy, 2010. **35**(18): p. 9527-9543.

115. Jin, X.F. and X.J. Xue, *Computational fluid dynamics analysis of solid oxide electrolysis cells with delaminations.* International Journal of Hydrogen Energy, 2010. **35**(14): p. 7321-7328.

116. Gemmen, R.S. and C.D. Johnson, *Evaluation of fuel cell system efficiency and degradation at development and during commercialization.* Journal of Power Sources, 2006. **159**(1): p. 646-655.

117. Ettler, M., et al., *Durability of Ni anodes during reoxidation cycles.* Journal of Power Sources, 2010. **195**(17): p. 5452-5467.

118. Duncan, K.L., et al., *Role of point defects in the physical properties of fluorite oxides.* Journal of the American Ceramic Society, 2006. **89**(10): p. 3162-3166.

119. Timoshenko, S.P. and J.N. Goodier, *Theory of Elasticity*. 1970, New York: McGraw-Hill.

120. Noda, N., R.B. Hetnarski, and Y. Tanigawa, *Thermal Stresses*. 2nd ed. 2003, New York: Taylor & Francis.

121. Newman, J., *Electrochemical systems*. 1991, NJ: Prentice-Hall, Englewood Cliffs.

122. Mizusaki, J., et al., *Nonstoichiometry and Defect Structure of the Perovskite-Type Oxides $La_{1-X}Sr_xFeO_{3-\delta}$* Journal of Solid State Chemistry, 1985. **58**(2): p. 257-266.

123. Zeng, Y. and Y.S. Lin, *A transient TGA study on oxygen permeation properties of perovskite-type ceramic membrane.* Solid State Ionics, 1998. **110**(3-4): p. 209-221.

124. Hashimoto, S., et al., *Oxygen nonstoichiometry and thermo-chemical stability of $La_{0.6}Sr_{0.4}Co_{1-y}Fe_yO_{3-\delta}$ (y=0.2, 0.4, 0.6, 0.8).* Solid State Ionics, 2010. **181**(37-38): p. 1713-1719.

125. Adler, S.B., J.A. Lane, and B.C.H. Steele, *Electrode kinetics of porous mixed-conducting oxygen electrodes.* Journal of the Electrochemical Society, 1996. **143**(11): p. 3554-3564.

126. Fleig, J. and J. Maier, *The polarization of mixed conducting SOFC cathodes: Effects of surface reaction coefficient, ionic conductivity and geometry.* Journal of the European Ceramic Society, 2004. **24**(6): p. 1343-1347.

127. Nakajo, A., et al., *Compilation of mechanical properties for the structural analysis of solid oxide fuel cell stacks. Constitutive materials of anode-supported cells.* Ceramics International, 2012. **38**(5): p. 3907-3927.

128. Atkinson, A. and A. Selcuk, *Mechanical behaviour of ceramic oxygen ion-conducting membranes.* Solid State Ionics, 2000. **134**(1-2): p. 59-66.

129. Du, Y.H., et al., *Extruded tubular strontium- and magnesium-doped lanthanum gallate, gadolinium-doped ceria, and yttria-stabilized zirconia electrolytes - Mechanical and thermal properties.* Journal of the Electrochemical Society, 2003. **150**(1): p. A74-A78.

130. Duncan, K.L. and E.D. Wachsman, *Continuum-Level Analytical Model for Solid Oxide Fuel Cells with Mixed Conducting Electrolytes.* Journal of the Electrochemical Society, 2009. **156**(9): p. B1030-B1038.

131. Gostovic, D., et al., *Three-dimensional reconstruction of porous LSCF cathodes.* Electrochemical and Solid State Letters, 2007. **10**(12): p. B214-B217.

132. Ormerod, R.M., *Solid oxide fuel cells.* Chemical Society Reviews, 2003. **32**(1): p. 17-28.

133. Hung, I.M., et al., *Phase stability and conductivity of Ba1-ySryCe1-xYxO3-delta solid oxide fuel cell electrolyte.* Journal of Power Sources, 2009. **193**(1): p. 155-159.

134. Song, H.S., et al., *Phase stability of Sm0.5Sr0.5CoO3 cathodes for on-planar type, single-chamber, solid oxide fuel cells.* Journal of Power Sources, 2009. **191**(2): p. 269-274.

135. Razbani, O., I. Waernhus, and M. Assadi, *Experimental investigation of temperature distribution over a planar solid oxide fuel cell.* Applied Energy, 2013. **105**: p. 155-160.

136. Nakajo, A., et al., *Simulation of thermal stresses in anode-supported solid oxide fuel cell stacks. Part I: Probability of failure of the cells.* Journal of Power Sources, 2009. **193**(1): p. 203-215.

137. Peksen, M., *3D thermomechanical behaviour of solid oxide fuel cells operating in different environments.* International Journal of Hydrogen Energy, 2013. **38**(30): p. 13408-13418.

138. Lowrie, F.L. and R.D. Rawlings, *Room and high temperature failure mechanisms in solid oxide fuel cell electrolytes.* Journal of the European Ceramic Society, 2000. **20**(6): p. 751-760.

139. Duncan, K.L., et al., *The role of point defects in the physical properties of nonstoichiometric ceria.* Journal of Applied Physics, 2007. **101**(4).

140. Jin, X. and X. Xue, *Micro Modeling Study of Cathode/Electrolyte Interfacial Stresses for Solid Oxide Fuel Cells.* Journal of The Electrochemical Society, 2013. **160**(8): p. F815-F823.

141. Mebane, D.S. and M.L. Liu, *Classical, phenomenological analysis of the kinetics of reactions at the gas-exposed surface of mixed ionic electronic conductors.* Journal of Solid State Electrochemistry, 2006. **10**(8): p. 575-580.

142. Mebane, D.S., Y.J. Liu, and M.L. Liu, *A two-dimensional model and numerical treatment for mixed conducting thin films.* Journal of the Electrochemical Society, 2007. **154**(5): p. A421-A426.

143. Kilner, J.A., R.A. DeSouza, and I.C. Fullarton, *Surface exchange of oxygen in mixed conducting perovskite oxides.* Solid State Ionics, 1996. **86-8**: p. 703-709.

144. Bessler, W.G., S. Gewies, and M. Vogler, *A new framework for physically based modeling of solid oxide fuel cells.* Electrochimica Acta, 2007. **53**(4): p. 1782-1800.

145. He, W.D., et al., *Gas transport in porous electrodes of solid oxide fuel cells: A review on diffusion and diffusivity measurement.* Journal of Power Sources, 2013. **237**: p. 64-73.

146. Minh, N.Q., *Solid oxide fuel cell technology-features and applications.* Solid State Ionics, 2004. **174**(1-4): p. 271-277.

147. Buchkremer, H.P., et al. *Advances in the anode supported planar SOFC technology.* in *Electrochemical Proceedings.* 1997. The Electrochemical Society, Inc.

148. Prentice, G.A., *Electrochemical Engineering Principles.* 1991, Upper Saddle River, New Jersey: Prentice Hall.

149. Hashin, Z. and S. Shtrikman, *A Variational Approach to the Theory of the Elastic Behaviour of Multiphase Materials.* Journal of the Mechanics and Physics of Solids, 1963. **11**(2): p. 127-140.

150. Bishop, S.R., K. Duncan, and E.D. Wachsman, *THERMO-CHEMICAL EXPANSION OF SOFC MATERIALS.* ECS Transactions, 2006. **1**(7): p. 13-21.

151. Lane, J.A. and J.A. Kilner, *Oxygen surface exchange on gadolinia doped ceria.* Solid State Ionics, 2000. **136**: p. 927-932.

152. Lynch, M.E., et al., *Enhancement of La0.6Sr0.4Co0.2Fe0.8O3-delta durability and surface electrocatalytic activity by La0.85Sr0.15MnO3 +/-delta investigated using a new test electrode platform.* Energy & Environmental Science, 2011. **4**(6): p. 2249-2258.

153. Weibull, W., *A Statistical Distribution Function of Wide Applicability.* Journal of Applied Mechanics-Transactions of the Asme, 1951. **18**(3): p. 293-297.

154. Zha, S.W., C.R. Xia, and G.Y. Meng, *Effect of Gd (Sm) doping on properties of ceria electrolyte for solid oxide fuel cells.* Journal of Power Sources, 2003. **115**(1): p. 44-48.

155. Wachsman, E.D. and K.T. Lee, *Lowering the Temperature of Solid Oxide Fuel Cells.* Science, 2011. **334**(6058): p. 935-939.

156. Schichlein, H., et al., *Deconvolution of electrochemical impedance spectra for the identification of electrode reaction mechanisms in solid oxide fuel cells.* Journal of Applied Electrochemistry, 2002. **32**(8): p. 875-882.

157. Wagner, N., et al., *Electrochemical impedance spectra of solid-oxide fuel cells and polymer membrane fuel cells.* Electrochimica Acta, 1998. **43**(24): p. 3785-3793.

158. Macdonald, J.R., *Impedance spectroscopy: Models, data fitting, and analysis.* Solid State Ionics, 2005. **176**(25-28): p. 1961-1969.

159. Warburg, E., *Ueber die Spitzenentladung.* Annalen der Physik, 1899. **303**(1): p. 69-83.

160. Franceschetti, D.R. and J.R. Macdonald, *Numerical-Analysis of Electrical Response - Biased Small-Signal Ac Response for Systems with One or 2 Blocking Electrodes.* Journal of Electroanalytical Chemistry, 1979. **100**(1-2): p. 583-605.

161. Franceschetti, D.R. and J.R. Macdonald, *Numerical-Analysis of Electrical Response - Statics and Dynamics of Space-Charge Regions at Blocking Electrodes.* Journal of Applied Physics, 1979. **50**(1): p. 291-302.

162. Macdonal.Jr, *Electrical Response of Materials Containing Space Charge with Discharge at Electrodes.* Journal of Chemical Physics, 1971. **54**(5): p. 2026-&.

163. Macdonal.Jr, *Simplified Impedance/Frequency-Response Results for Intrinsically Conducting Solids and Liquids.* Journal of Chemical Physics, 1974. **61**(10): p. 3977-3996.

164. Macdonald, J.R. and D.R. Franceschetti, *Theory of Small-Signal Ac Response of Solids and Liquids with Recombining Mobile Charge.* Journal of Chemical Physics, 1978. **68**(4): p. 1614-1637.

165. Brumleve, T.R. and R.P. Buck, *Numerical solution of the Nernst-Planck and poisson equation system with applications to membrane electrochemistry and solid state physics.* Journal of Electroanalytical Chemistry and Interfacial Electrochemistry, 1978. **90**(1): p. 1-31.

166. Brumleve, T.R. and R.P. Buck, *Transmission-Line Equivalent-Circuit Models for Electrochemical Impedances.* Journal of Electroanalytical Chemistry, 1981. **126**(1-3): p. 73-104.

167. Jamnik, J. and J. Maier, *Treatment of the impedance of mixed conductors - Equivalent circuit model and explicit approximate solutions.* Journal of the Electrochemical Society, 1999. **146**(11): p. 4183-4188.

168. Jamnik, J. and J. Maier, *Generalised equivalent circuits for mass and charge transport: chemical capacitance and its implications.* Physical Chemistry Chemical Physics, 2001. **3**(9): p. 1668-1678.

169.   Moya, A.A., A. Hayas, and J. Horno, *Steady-state, transient and small-amplitude AC responses of an electrochemical cell with immobile background charge: A network approach.* Solid State Ionics, 2000. **130**(1-2): p. 9-17.

170.   Lai, W. and S.M. Haile, *Impedance spectroscopy as a tool for chemical and electrochemical analysis of mixed conductors: A case study of ceria.* Journal of the American Ceramic Society, 2005. **88**(11): p. 2979-2997.

171.   Ciucci, F., Y. Hao, and D.G. Goodwin, *Impedance spectra of mixed conductors: a 2D study of ceria.* Physical Chemistry Chemical Physics, 2009. **11**(47): p. 11243-11257.

172.   Boukamp, B.A., *Small signal response of the BiCuVOx/noble metal/oxygen electrode system.* Solid State Ionics, 2000. **136**: p. 75-82.

173.   Boukamp, B.A. and H.J.M. Bouwmeester, *Interpretation of the Gerischer impedance in solid state ionics.* Solid State Ionics, 2003. **157**(1-4): p. 29-33.

174.   Adler, S.B., *Mechanism and kinetics of oxygen reduction on porous La1-xSrxCoO3-delta electrodes.* Solid State Ionics, 1998. **111**(1-2): p. 125-134.

175.   Adler, S.B., *Factors governing oxygen reduction in solid oxide fuel cell cathodes.* Chemical Reviews, 2004. **104**(10): p. 4791-4843.

176.   Sluyters.M and J.H. Sluyters, *On Impedance of Galvanic Cells .29. Potential Dependence of Faradaic Parameters for Electrode Processes with Coupled Homogeneous Chemical Reactions.* Journal of Electroanalytical Chemistry, 1970. **26**(2-3): p. 237-&.

177.   Robertson, N.L. and J.N. Michaels, *Oxygen-Exchange on Platinum-Electrodes in Zirconia Cells - Location of Electrochemical Reaction Sites.* Journal of the Electrochemical Society, 1990. **137**(1): p. 129-135.

178.   Gerischer, H., **Bestimmung Der Austauschgeschwindigkeit Beim Gleichgewichtspotential Durch Polarisationsmessungen Mit Gleichstrom Und Wechselstrom.* Zeitschrift Fur Elektrochemie, 1951. **55**(2): p. 98-104.

179.   Araki, W., Y. Imai, and T. Adachi, *Mechanical stress effect on oxygen ion mobility in 8 mol% yttria-stabilized zirconia electrolyte.* Journal of the European Ceramic Society, 2009. **29**(11): p. 2275-2279.

180.   Araki, W., M. Kuribara, and Y. Arai, *Effect of uniaxial stress on ionic conductivity of 14 mol%-yttria-stabilized zirconia single crystal.* Solid State Ionics, 2011. **193**(1): p. 5-10.

181.   Lai, W., *Impedance Spectroscopy as a Tool for the Electrochemical Study of Mixed Conducting Ceria.* 2007, California Institute of Technology, Pasadena, California. p. 166.

182.   X, G. and R. Waser, *Space charge concept for acceptor-doped zirconia and ceria and experimental evidences.* Solid State Ionics, 2004. **173**(1-4): p. 63-67.

183.   Maier, J., *On the Conductivity of Polycrystalline Materials.* Berichte Der Bunsen-Gesellschaft-Physical Chemistry Chemical Physics, 1986. **90**(1): p. 26-33.

184.   Lai, W., *Impedance Spectroscopy as a Tool for the Electrochemical Study of Mixed Conducting Ceria*. 2007, California Institute of Technology.